Synthesizing High-Quality Graphene Membranes for Engineering Diffusion Barriers

By

Susmit Singha Roy

A dissertation submitted in partial fulfillment of

the requirements for the degree of

Doctor of Philosophy

(Materials Science)

at the

UNIVERSITY OF WISCONSIN – MADISON

2015

Date of final oral examination: 6/9/2015

The dissertation is approved by the following members of the Final Oral Committee:
Michael S. Arnold, Associate Professor, Materials Science and Engineering
Padma Gopalan, Professor, Materials Science and Engineering
Paul Evans, Professor, Materials Science and Engineering
Izabela Szlufarska, Professor, Materials Science and Engineering
Franz Himpsel, Professor, Physics

Abstract

We demonstrate significant advances in the fundamental understanding and engineering of scalable graphene diffusion barriers. Experimental studies have established that defect-free non-scalable graphene is an excellent barrier material, however its scalable counterparts are still well behind in terms of performance. The latter's ability to perform as a barrier membrane is compromised primarily by the presence of three major problems - high density of defects, self-degradation in ambient environment and induced electrochemical oxidation of the underlying material. First, we develop an in-depth understanding of how diffusion occurs through monolayer graphene grown via chemical vapor deposition. It is shown that the atomic membrane is impenetrable in the pristine regions, however it is easily penetrated by oxygen and water at grain boundaries and intrinsic pinholes. Second, we study in detail the self-deterioration of graphene in ambient and quantify the evolution, kinetics, and energetics of the degradation process both in the pristine and intrinsically defective regions of graphene. It is also found that the degradation process is accelerated in the presence of water vapor. Third, we find that the overall defect density of a graphene membrane is primarily determined by the density of its intrinsic pinholes and grain boundaries. We demonstrate that the density on intrinsic pinholes can be significantly reduced by reducing the surface roughness of the growth substrate which is achieved by regulating the pre-growth annealing time and temperature. The density of the grain boundaries can be altered by varying the internucleation distance during the growth of the membrane. Fourth, when graphene is used as a corrosion barrier for metals, we establish that the electrochemical corrosion of the metal can be drastically reduced by adding an ultra-thin electrically insulating layer between the graphene and the metal. In addition, the barrier performance is enhanced greatly by stacking more layers of graphene top of the first layer. Finally, we combine all the results and knowledge from

these previous studies to design the best performing scalable graphene barrier until date. We expect this study to serve as a foundation for engineering next-generation graphene barriers with performance comparable to its pristine and theoretical counterparts.

Acknowledgements

I am extremely grateful for all the support I have been given during the course of my doctoral research at University of Wisconsin – Madison. I would like to take this opportunity to thank each and every one of them.

First, I would like to thank Prof. Michael S. Arnold for his trust, supervision, motivation, ideas and also for letting me be a part of his group. He has been and will always be a constant source of inspiration for me. It goes without saying, this would not have been possible without his presence. I would also like to thank my mentors in the Arnold group - Dr. Nate Safron, Dr. Dominick Bindl and Adam Brewer for their advice, guidance and patience. I have also been privileged and immensely benefitted from working alongside a very talented group of mentors (mentioned above) and colleagues in the Arnold group, namely Meng-Yin Wu, Robert Jacobberger, Matthew Shea , Chenghao Wan, Gerald Brady, Amir Mashal, Dr. Feng Xu, Dr. Yumin Ye, Jialiang Wang, Alan Albrecht, Juan Zhao, Dr. Alireza Mohebbi, Dr. Naechul Shin and Austin Way. The research group as a whole has not only been a great source of encouragement and feedback at work, but they are also great friends outside work and have made my stay in Madison very memorable.

In addition, I was also fortunate to have an exceptional set of collaborators with whom I was able to work on cross-disciplinary projects and understand better the broader impact of my research. I would like to thank Lushuai Zhang (Andrew group, Chem, UW), Peter Mushenheim (Abbott group, CBE, UW), Ling Li (Wong group, ECE, Stanford), Jon Choi (Gopalan group, MSE, UW), Mike Kratchovil (Lynn group, CBE, UW), Zhaodong Li (Wang group, MSE, UW), Caroline English (Hamers group, Chem, UW), Dr. Rina Maeda (Weibel group, BioChem, UW) and Mark Wall (Thermofisher Scientific, Madison) for their collaborative work. Furthermore, I am very grateful to my PhD committee for providing me with expert opinion, encouragement, feedback and valuable suggestions during the course of my doctoral program. I would also like to thank the different agencies that have funded our research.

Finally, I would like to thank my family and friends, especially my parents - Sandip and Aparna, my sister- Chandrima and my best friend - Sneha for being there and supporting me throughout. It is impossible to describe in words how much of an influence they have been and what their presence and support has enabled me to do.

Table of Contents

1. Introduction

List of Figures and Tables

1. Introduction

1.1. Graphene: Structure, Properties and Applications

Graphene is a 2-dimensional allotrope of carbon where the individual carbon atoms are bonded together in a tightly packed sp^2 honeycombed structure with an extremely small C-C bond distance of 1.42Å.[1] Each carbon atom has four bonds, three single σ-bonds with each of its in-plane neighbors and one out-of-plane π-bond. This structure not only allows graphene to possess several extraordinary properties and but it also opens doors to numerous exciting applications in diverse fields.[2-4] Since its discovery in the year 2004,[5] graphene has generated an unprecedented amount of interest in both theoretical and experimental studies in almost every area of science and engineering. It has even given rise to a new era of 2D Materials which promises to revolutionize and replace the existing technology in several areas.[6, 7] Due to its sheer enormity, it is beyond the scope of this thesis to include all the exciting properties and applications of graphene and hence this sub-section is restricted to the discussion of a selected few that are relevant to this study.

Electronic Properties and Applications

Due to its structure, graphene is a zero bandgap material and the valence band and the conduction band of graphene meet at six Dirac points in the momentum space (Fig. 1.1).[4] In addition to being a good electrical conductor, experimental studies have shown that monolayer graphene has an extremely high charge carrier mobility at room temperature of 15,000 $cm^2V^{-1}s^{-1}$.[3] The mobility is weakly coupled with temperature and extremely high values excess of 200,000 $cm^2V^{-1}s^{-1}$ have been achieved on free-standing graphene by reducing the defect and charged-impurity scattering.[8, 9] Graphene by itself can't be used in transistors for high-performance integrated logic circuits as a channel material because of the absence of a bandgap. However, quantum-confinement generated from nano-patterning the graphene layer in the form of ribbons, anti-dots etc.[10-13] allow the material to have the much need bandgap for transistor applications. In addition, the superior electronic properties in combination with some of the other properties discussed later namely, transparency, flexibility and impermeability, makes graphene an excellent choice transparent electrode material for use in organic photovoltaic (OPV) and organic light emitting diodes (OLED) devices.[14-19]

Mechanical Properties and Applications

Graphene currently holds the record of the strongest material ever to be tested.[20] It has an intrinsic tensile strength of 130 GPa and a Young's modulus of 1TPa. Graphene platelets stacked together via flow-directed assembly to form a paper can have an extremely high fracture strength of 120 MPa.[20] The superior mechanical strength in combination with other properties mentioned in this section (such as thermal and chemical stability and impermeability) opens doors to use of graphene as a selective transport membrane for water desalination, gas separation and controlled drug-delivery.[21-25]

Transparency

The electronic band-structure of monolayer graphene allows the atomic membrane to possess unique optical properties. One of the most notable among them is that graphene has a high transparency of ~97.7% which is uniform over the visible range to the infra-red range of the electromagnetic spectrum.[26, 27] Also, the transmission and reflectivity of graphene are not related to its material parameters. This makes the atomic membrane an excellent potential choice to be used as a transparent conductor in organic semiconducting devices like OPVs and OLEDs.

Thermal and Chemical Stability

It has been shown that free-standing graphene has an extraordinarily high thermal conductivity of 5000 $Wm^{-1}K^{-1}$.[28] In addition, theoretical studies and experimental research on defect-free suspended graphene has shown that graphene has remarkable thermal stability. The sublimation temperature of graphites is as high as 4000 K.[29, 30] Furthermore, in ultra-high vacuum and inert conditions graphene monolayers have been shown to be stable up to 2600 K.[31] Graphene is also noted for its superior chemical stability oxidative and corrosive environments. In particular, the chemical stability of graphene allows it to be isolated from the growth substrate after chemical vapor deposition and integrated with arbitrary substrates without sustaining any chemical damage or modification from the process.[27, 32-34] The thermal and chemical stability of the material make it an excellent choice for use in corrosion preventive coatings, filtration and high temperature applications.

Impermeable Membrane

As a consequence of a tightly bound sp^2 honeycomb lattice and a small C-C bond distance of 1.42 Å, graphene is impenetrable to even species as small as atomic Helium (Fig. 1.2).[35] This remarkable property of graphene opens up its use in several important applications. It allows it to be potentially used as a corrosion preventive layer to prevent oxidation of refined metals by oxygen and water. In addition, it can also be used as a diffusion barrier for copper interconnects in integrated circuits to prevent dielectric breakdown due to copper migration into the gate-oxide layer.[36, 37] Furthermore, it can be used as size selective transport membrane for water desalination, gas separation and controlled drug-delivery. A more detailed discussion on this property of graphene is included in section 1.4 later in the text.

Flexibility and Scalability

As a result of its structure and superior mechanical properties, graphene is an extremely flexible material.[14, 16, 17, 27, 38, 39] The fracture strain of graphene is significantly better than ten than Indium Tin Oxide which is the commercially used conductor for transparent displays. Graphene monolayers, multilayers and films can be manufactured via several scalable techniques such as chemical vapor deposition, solution-processing etc. can be transferred/integrated onto substrates in large-areas. In particular graphene can be manufactured in meter scale areas using chemical vapor deposition and transferred onto flexible substrates via roll-to-roll processing techniques as depicted in figure 1.3. [27]These make graphene an ideal choice for replacing an increasing expensive to process Indium Tin Oxide as a transparent conductor in displays and photovoltaic devices. In combination with its flexibility and impenetrability, the material has great potential in the areas of flexible organic semiconductor device applications.

1.2. Synthesis methods of graphene and challenges

Mechanical Exfoliation

In this method flakes of graphite are cleaved using a scotch tape until there is a single layer sheet of graphene remaining.[5, 40] The method produces graphene sheets that are pristine and almost defect free and are important for proof of principle studies of properties of graphene. Most of the notable record breaking feats of graphene as a material that have been experimentally achieved until date are using mechanically exfoliated graphene layers. However, this manufacturing technique has severe drawbacks which are almost impossible to overcome. The yield of monolayer and few layer graphene which are the materials of interest for most research is extremely low. In addition, the monolayer regions are restricted to only a few hundred μm^2. These make it impossible for the mechanical exfoliation technique to be scalable.

Liquid phase exfoliation and graphene-oxide solution-processing

In this method graphite flakes are dispersed in a solvent where it favors an increase in total surface area. The process can be aided by sonication and with increasing sonication time the fraction of monolayer in the solvent also increases. This fraction can also be further improved via sonication. A similar approach is also used for dispersing graphene oxide in aqueous media. Graphite platelets are first oxidized to functionalized them with oxygen and then exfoliated via sonication.[41] These exfoliated layers of graphene or graphene oxide can be uniformly coated onto arbitrary substrates or can also be made into films or paper via flow-directed assembly.[41] This manufacturing technique of few layered graphene, though easily scalable, is limited in its performance by the size of the platelets and the high density of defects in them.

SiC based synthesis

It has been shown that mono or few layers of graphene can be synthesized on either on the silicon or carbon terminated surface of a SiC wafer by sublimating Si atoms, thereby leaving a graphitized surface.[42] The quality of graphene produced via this technique is pristine and almost defect-free. However, the extremely high processing temperatures and high wafer costs are big limiting factors when it comes to using this method for mass manufacture.

Chemical Vapor Deposition

Large-area mono and few-layer graphene sheets can be grown by catalyzing a carbon precursor on refined transition metals or semiconductors at elevated temperature in the presence of hydrogen.[43-52] The graphene membranes manufactured via this technique is polycrystalline and can be easily isolated from its growth substrate and transferred onto arbitrary substrate in very large areas, thus making this method easily scalable (figure 1.4).[53] The technique also offers great control over layer uniformity. The most commonly used growth catalyst for chemical vapor deposition based monolayer graphene growth is copper. Solubility of carbon in copper is extremely low even at high temperature making the graphene growth a surface based process on the substrate. The vapor deposition process on Cu is also self-limiting where the graphene growth stops after formation of a continuous single layer.[54] All the above mentioned traits along with the make chemical vapor deposition the most favored and commonly used method for synthesizing graphene for applications that require scaling. This technique is used throughout this thesis for manufacturing continuous single layers of graphene. More details about parameters used during the growth process are discussed in the respective experimental methods section of each chapter. The graphene manufactured via this technique is not defect-free and consists of grain-boundaries, vacancies, point-defects etc. Though the density of these defects can be controlled and minimized to a great extent as elaborated in following chapters in this thesis, however, until date it has been impossible to completely eliminate them. More research is required on synthesis of graphene using chemical vapor deposition to achieve this goal.

1.3. Defect characterization in graphene

As mentioned in section 1.2, graphene manufactured via chemical vapor deposition is not free from defects. The polycrystalline nature of the growth generates grain boundaries in graphene. In addition, the surface roughness and surface impurities of the growth catalysts can create nanopores or holes in the graphene layer where the graphene growth is incomplete. Furthermore, defects in graphene can be induced by extrinsic factors such as elevated temperatures, oxidizing agents, ion bombardment, plasma etc.[55-60] The ability to characterize this defect allows us to understand and relate the limitations posed by them on the properties of graphene. There are several techniques that can be used to visualize or quantify the defects in the graphene layer and the ones relevant to this study are listed below.

Raman Spectroscopy

Raman spectroscopy is extremely useful technique to characterize not only graphene but carbon nanomaterials in general.[61, 62] Raman spectroscopy can be used not only to study defects in graphene but can also be used to characterize mechanical strain, doping and quantifying number of layers.[13, 63-69] A typical Raman spectra of graphene as shown in figure 1.5 has three prominent features namely, the D-band (1345 cm^{-1}), G-band (1585 cm^{-1}) and the 2D-band (2670 cm^{-1}).[70] The mechanism behind formation of these bands is very well studied in literature.[64, 69, 71-75] In this thesis we are interested in using Raman spectroscopy to relatively quantify the density of defects in graphene. The D-band to G-band ratio is a quantity that directly relates to the number of the defects in area scanned by the laser. For CVD-graphene monolayer when excited with a 532 nm laser wavelength, a D-band to G-band ratio of <0.1 proves that the graphene is of superior quality and has low density of defects. More details on this characterization tool can be found in the subsequent chapters of this thesis.

Scanning Electron Microscopy

It is important to point out at the very beginning that scanning electron microscopy cannot be used to resolve the defects in a graphene monolayer directly. However, there are approaches that can be used to visually emphasize the location of the defects in the graphene layer and can be used visualize the defective regions indirectly. To visualize and quantify the intrinsic holes present in monolayer graphene, it is immersed in a very dilute copper etching solution.[23] The graphene layer is able to block out the copper etchant from reaching the copper everywhere expect in the regions of incomplete growth or highly defective regions, referred as intrinsic nanopores. In the nanopores, the etchant is able to diffuse through the graphene layer to the copper underneath and form etch-pits in the copper. These etch-pits grow wider and deeper with time and are easily visualized under the SEM after prescribed amount of etching and quantified using image analysis software. More details on this technique can be found in chapter 4 of this study. To visualize grain boundaries in a graphene monolayer under the SEM, the graphene on an arbitrary substrate can be annealed at an elevated in ambient air. This oxidizes the carbon atoms at the grain boundaries and edges and then gasifies them, making the grain boundaries wider with time. The rate of etching is directly related to the annealing time and temperature. Once etched the grain boundaries have different contrast compared to the grain interiors can be easily.[55] More details on this method is discussed in chapter 3 of this work.

1.4. Graphene as a diffusion barrier

Theoretical and experimental studies on pristine and defect-free graphene have shown that graphene has the ability to outperform the materials that are currently being used as diffusion barriers. The densely-packed sp^2-honeycombed structure makes the monolayer of atoms impenetrable to even atomic He.[35] This when combined with graphene's superior thermal stability, chemical inertness, transparency and flexibility make it a great candidate for barrier applications.[14, 16, 31, 34, 76-79] However, graphene's success as a barrier depends on the ability to reproduce the results obtained from theoretical or pristine graphene using scalable approaches.[23, 24, 80] Initial research by Compton *et al.* has demonstrated that nanosheets of graphene when used as a filler material in polymer films can significantly enhance its barrier properties.[81] A pioneering experimental study by Chen *et al*. has shown that large-area monolayer graphene grown via chemical vapor deposition (CVD) can be used to reduce the oxidation of refined metals even at elevated temperatures up to 200 ° C (Fig. 1.6).[82] Kang *et al*. have also shown similar results using reduced graphene oxide and Yu *et al.* have utilized 30–40 nm thick layers of self-assembled graphene oxide (GO)-polyethleneimine (PEI) composites on PET to reduce the oxygen transmission rate to 0.05 $cc.m^{-2}day^{-1}$.[83] In addition, Kirkland et al. have demonstrated that mixed-thickness CVD-graphene coatings on Ni and

Cu can serve as barriers to electrochemical corrosion in aqueous media.[84] Prasai *et al.* have shown that multilayer graphene grown on Ni can act as a better diffusion barrier than a single layer. However, while these demonstrations of scalable graphene barriers have served as an important proof-of-principal, thus far, their performance has still been substantially below their pristine and defect-free counterparts.[85] Previous work by our group has shown that the performance of CVD-graphene based barriers can greatly enhanced via increasing the internucleation distance and stacking of multiple monolayers.[70] In addition, recent studies by Zhou *et al.* and Schriver *et al*. have shown that monolayer graphene promotes extensive electrochemical corrosion of underlying copper over a period of few months and few hours at room and elevated temperatures (~473 K), respectively, thereby severely reducing its ability to perform as a corrosion-inhibiting material.[86, 87] Finally, a recent study by our group has also shown that a graphene monolayer becomes discontinuous due to etching at intrinsic defects and grain boundaries in a matter of few hours in ambient atmosphere at slightly elevated temperatures (>473 C).[55]

In summary, these studies indicate that the problem with using scalable graphene as a barrier is three-fold – (i) high density of defects compared to pristine or theoretical graphene providing spurious diffusion pathways, (ii) degradation and etching of the monolayer graphene at the defective regions at elevated temperatures in ambient atmosphere and (iii) enhanced oxidation of underlying metal in presence of graphene due to electrochemical corrosion. Problem (i) has been and still is one of the most substantial for applications not only pertaining to barriers but also to any application of graphene that requires scalability.[45, 48, 88, 89] Though there are a few ways to minimize the intrinsic defect concentration in scalable-graphene, for example increasing the internucleation distance during the CVD process.[70]

However, the graphene manufactured using these techniques is still far from its pristine or defect-free state. Studies to reduce the defect density of scalable-graphene are being constantly pursued by our group and other groups working on synthesis of graphene. In this paper, we focus on addressing the problems (ii) and (iii) which are equally limiting when it comes to ability of graphene to perform as a diffusion barrier. Problem (ii) occurs when the defective regions in monolayer graphene are exposed to air and water. This leads to oxidation of the graphene at the defects and subsequent gasification of the oxidized carbon atom in the form of CO or CO_2, leading to formation holes in the graphene layer in the form of etched pits and grain boundaries.[55] This effect is accelerated at elevated temperatures. The holes formed from the etching process can act as spurious diffusion pathways when monolayer graphene is being used as a barrier membrane. Problem (iii) arises when graphene is in electrical contact with the material that needs protection from oxidation. Due to a difference in the electrochemical potentials of graphene and the underlying material, an electrochemical cell is created that promotes the corrosion of the material, as shown for the case of graphene protecting copper in previous studies.[86, 87]

1.5. Scope of thesis

The experimental demonstration of impermeability of graphene to atomic Helium shown by Bunch *et al*. has opened door to wide range of applications for graphene to be used as a diffusion barrier.[35] The most notable among them being, corrosion protection of refined metals, encapsulation of organic semiconducting devices, water desalination, gas separation and controlled drug-delivery etc.[24, 25, 70, 90, 91] Though used of pristine, defect-free and non-scalable form of graphene has shown its superior performance in each of these application and potential to replace the existing technology, the performance using scalable techniques of manufacturing graphene have been below par. In particular, to use scalable graphene as a corrosion preventing layer one needs to overcome three drawbacks mentioned in section 1.4: (i) high density of defects compared to pristine or theoretical graphene providing spurious diffusion pathways, (ii) degradation and etching of the monolayer graphene at the defective regions at elevated temperatures in ambient atmosphere and (iii) enhanced oxidation of underlying metal in presence of graphene due to electrochemical corrosion. In the following chapters we focus on understanding and critically analyzing these problems in detail and along the way develop novel and innovative techniques to minimize or overcome these problems.

In chapter 2, we show that defects in graphene can act as spurious diffusion pathways for oxygen and water to reach the underlying metal and corrode it. In addition, we show that the performance of graphene diffusion barriers can be enhanced by stacking multiple layers of graphene and increasing grain size. We focus on understanding large-area barriers of graphene grown by chemical vapor deposition in the context of passivating an underlying Cu substrate from oxidation in air at 200 °C and use imaging Raman spectroscopy as a tool to temporally and spatially map the barrier performance and to guide barrier design.

In chapter 3, the evolution, kinetics, and energetics of this degradation is quantified. Specifically, the deterioration of graphene on SiO_2 is studied in grain interiors and at grain boundaries in ambient air, dry air and nitrogen between 473 and 673 K, using spatially and temporally resolved in situ Raman spectroscopy in addition to electron microscopy and charge transport measurements. The results from this study can be used to quantitatively predict graphene oxidation and gasification on SiO2 in different environments and temperature.

In chapter 4, origin of intrinsic nanopores in graphene manufactured via chemical vapor deposition is studied. It is found that copper foils that are most commonly used as a catalyst for graphene growth, the degree of completeness of the growth is limited by the surface roughness of the foil. The density of the nanopores decreases when the surface roughness of the growth substrate is reduced by either increasing the pre-growth annealing temperature and time. The hole density is significantly minimized when atomistically smooth epitaxial copper is used as the growth substrate, in which case the degree of completeness of the growth is just limited by the presence of surface irregularities of the catalyst.

In chapter 5, we show that the degree of electrochemical corrosion of the underlying metal can be reduced by adding an electrically insulating layer between the graphene and the metal. We combine this with our findings from chapter 2-4 and design high-performance heterostructured scalable graphene barriers for corrosion protection. We set the foundation for future studies and engineering of scalable diffusion barriers based on graphene for corrosion protection.

In chapter 6, we explore another application that utilizes graphene’s ability to be transparent, impenetrable, conductive and flexible material; use of graphene as a transparent electrode in organic photovoltaics. Charge and energy transport in organic semiconductors is highly anisotropic and dependent on crystalline ordering. Here, we demonstrate a novel approach for ordering crystalline organic semiconductors, with orientations optimized for optoelectronics applications, by using a single monolayer of graphene as a molecular template. We show as a proof-of-principle, that large-area graphene can be integrated on metals and oxides to modify their surface energies and used to template copper phthalocyanine (CuPc), a prototypical organic semiconductor. On unmodified substrates, thermally evaporated films of CuPc are small-grained, and the molecules are in the "standing-up" (100) orientation. On graphene modified substrates, CuPc is templated in favorable "lying-down" $(11\bar{2})$ and $(01\bar{2})$ orientations with drastically larger crystal sizes.

Finally, in Chapter 7, we summarize the results and provide outlook for future directions of research in this field.

Figures:

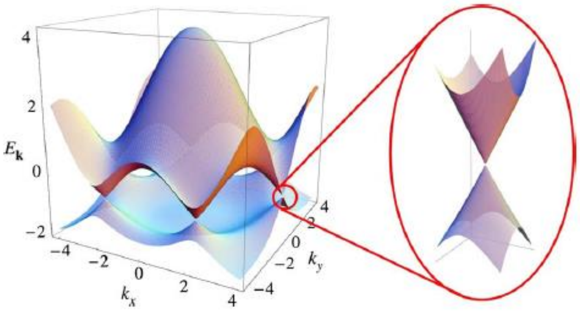

Figure 1.1. Band-structure of graphene depicting the six Dirac points in the momentum space resulting in a zero band-gap. Reproduced from Castro Neto *et al.*[4]

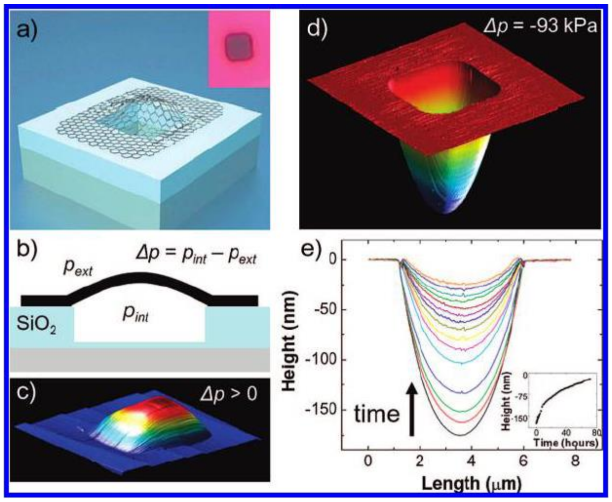

Figure 1.2. (a) Schematic of a graphene sealed microchamber with helium. (Inset) optical image of a single atomic layer graphene drumhead on 440 nm of SiO_2. The dimensions of the microchamber are 4.75 μm × 4.75 μm × 380 nm. (b) Side view schematic of the graphene sealed microchamber. (c) Tapping mode atomic force microscope (AFM) image of a ∼ 9 nm thick many layer graphene drumhead with $\Delta p > 0$. The dimensions of the square microchamber are 4.75 μm × 4.75 μm. The upward deflection at the center of the membrane is z) 90 nm. (d) AFM image of the graphene sealed microchamber of Figure 1a with Δp) -93 kPa across it. The minimum dip in the z direction is 175 nm. (e) AFM line traces taken through the center of the graphene membrane of (a). The images were taken continuously over a span of 71.3 h and in ambient conditions. (Inset) deflection at the center of the graphene membrane vs time. (Figure and caption reproduced from Bunch *et al.*). [35]

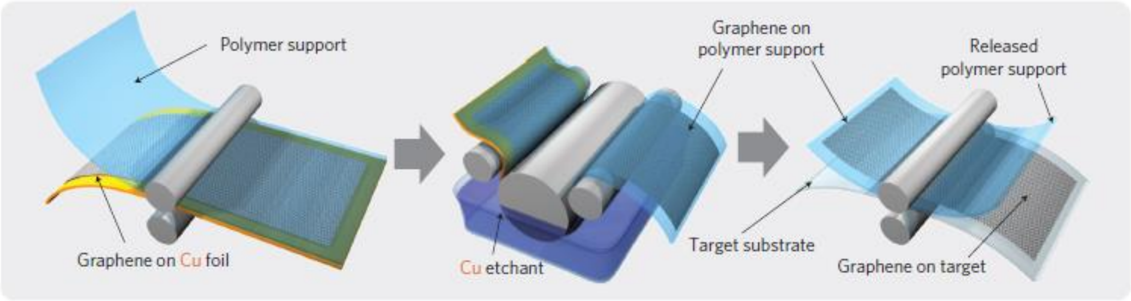

Figure 1.3. Schematic depicting the roll-based production of graphene films grown on a copper foil. Reproduced from Bae *et al.*[27]

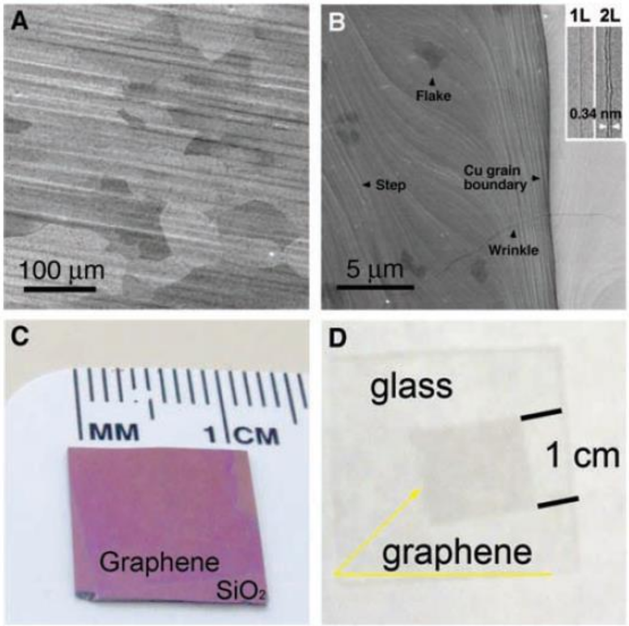

Figure 1.4. Graphene grown via chemical vapor deposition and transferred onto arbitrary substrates. (A) SEM image of graphene on a copper foil with a growth time of 30 min. (B) High-resolution SEM image showing a Cu grain boundary and steps, two- and three-layer graphene flakes, and graphene wrinkles. Inset in (B) shows TEM images of folded graphene edges. 1L, one layer; 2L, two layers. (C and D) Graphene films transferred onto a SiO2/Si substrate and a glass plate, respectively. Reproduced from Li *et al*.[53]

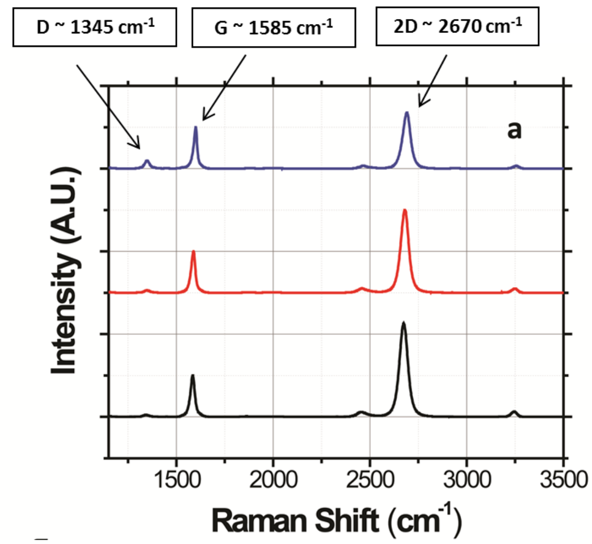

Figure 1.5. Raman spectra of monolayer graphene highlighting the three prominent features: D-band (1345 cm^{-1}), G-band (1585 cm^{-1}) and the 2D-band (2670 cm^{-1}) using a 532 nm laser excitation wavelength. Reproduced from Singha Roy *et al*.[70]

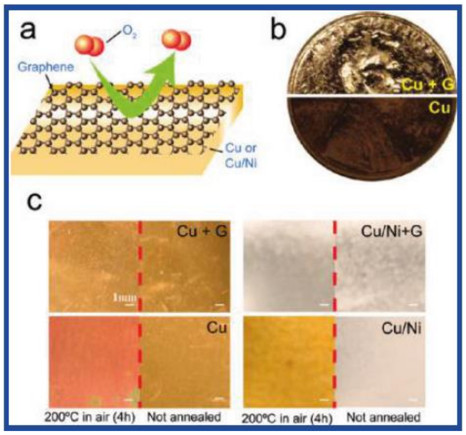

Figure 1.6. Proof-of principle experimental study using graphene synthesized via chemical vapor deposition for corrosion prevention of refined metals. (a) Illustration depicting a graphene sheet as a chemically inert diffusion barrier. (b) Photograph showing graphene coated (upper) and

uncoated (lower) penny after H_2O_2 treatment (30%, 2 min). (c) Photographs of Cu and Cu/ Ni foil with and without graphene coating taken before and after annealing in air (200 °C, 4 h). Reproduced from Chen *et al*.[82]

2. Understanding diffusion through graphene atomic membranes

This chapter was adopted from “Singha Roy, S.; Arnold, M., Improving Graphene Diffusion Barriers via Stacking Multiple Layers and Grain Size Engineering. *Advanced Functional Materials* **2013,** 23, (29), 3638-3644.” *SS performed all the experiments and analysis for the study*.

Abstract

We show that the performance of graphene diffusion barriers can be enhanced by stacking multiple layers of graphene and increasing grain size. We focus on understanding large-area barriers of graphene grown by chemical vapor deposition (CVD) in the context of passivating an underlying Cu substrate from oxidation in air at 200 °C and use imaging Raman spectroscopy as a tool to temporally and spatially map the barrier performance and to guide barrier design. At 200 °C in air, Cu oxidation proceeds in multiple regimes: first slowly *via* transport through atomic-scale grain boundary defects inherent to CVD-graphene and then more rapidly as the graphene itself degrades and new defects are formed. In the initial regime, the graphene passivates better than previously reported, for example Cu oxidation after 120 minutes is reduced by 41, 73, and >403 when passivated by 1, 2, and 4 stacked sheets of graphene, respectively, with 3 μm grains, compared with bare Cu. The Raman maps and electron microscopy show that whereas oxidation through single sheets primarily occurs through grain boundaries, oxidation through multiple sheets is spatially confined to their intersection. Performance further increases with grain-size; increasing grains from 3 to 14 μm decreases the oxidation rate by an additional factor of 5 per sheet. The degradation of the graphene itself at 200 °C is evidenced by an increase

in its D-band Raman mode, ultimately limiting high temperature but suggesting superior low temperature barrier performance. This study is expected to improve the understanding of mass transport through CVD-graphene materials and lead to improved large area graphene materials for barrier applications.

2.1. Introduction

Recent experimental and theoretical work show that the one atom thick, densely packed sp^2-honeycomb network of graphene makes it nearly impenetrable to species even as small as atomic He.[35] Graphene has been found to be thermally stable even over 2600 K in inert and ultra-high vacuum environments,[31] and other experimental studies also suggest its extraordinary durability at high temperatures.[42, 67, 79, 92] Additionally, research has shown that the atomic membrane is electrochemically inert over a wide range of potentials when used as an electrode in display devices.[17, 76] Moreover, graphene can be transferred onto arbitrary substrates, is over 97% transparent, and can be scaled to areas as large as 30 inch (diagonal) *via* chemical vapor deposition (CVD).[27, 33, 93] These attributes inherently make graphene and graphene based materials appealing candidates for diffusion barriers in applications including the corrosion inhibition of reactive/refined metals, lifetime enhancement of organic photovoltaic devices (OPV), and ultrasensitive gas detection.[14, 82, 85, 91, 94-97]

Initial research by Compton et al. has demonstrated that nanosheets of graphene when used as a filler material in polymer films can significantly enhance its barrier properties.[81] A recent pioneering experimental study by Chen *et al.* has shown that large-area CVD-grown atomic membranes of graphene can be used to reduce the oxidation of refined metals even at elevated temperatures up to 200 °C.[82] Kang *et al.* have also shown similar results using reduced graphene oxide [95] and Yu *et al.* have utilized 30 – 40 nm thick layers of self-assembled graphene oxide (GO)-polyethleneimine (PEI) composites on PET to reduce the oxygen transmission rate (OTR) to 0.05 cc/m^2-day. In addition, Kirkland *et al.* have demonstrated that mixed-thickness CVD-graphene coatings on Ni and Cu can serve as barriers to electrochemical corrosion in aqueous media.[83, 84] Furthermore, Prasai *et al.* have shown that multiple layers of CVD-graphene can have a multiplicative effect and act as a better diffusion barrier than a single layer.[85] However, while these demonstrations of large-area graphene barriers have served as an important proof-of-principal, thus far, their performance has still been substantially below their theoretical limit.

The first practical challenge in implementing graphene as a large-area diffusion barrier is that, because it is only one atomic layer, even a single defect has the possibility of providing a spurious transport pathway for leakage across its thickness. CVD-graphene, while attractive for its scalability, is known in particular to be punctuated by microscopic (tears and holes) and atomic-scale (grain boundary) defects. In principal, it should be possible to eliminate tears and holes by refining the purity and smoothness of the Cu growth substrates, processing in more particulate-free environments, and developing better graphene transfer procedures. On the other hand, grain boundaries will always be ubiquitous in polycrystalline CVD-graphene. It has been theoretically shown by Topsakal *et al.* that grain boundary defects can act as spurious diffusion pathways for oxygen transport.[94] Chen *et al.* have imaged the oxidation of Cu through single layers of graphene and shown that the Cu oxidizes in a pattern that appears to be related to the grain boundaries of the graphene, but the correlation between grain boundaries and oxidation was not explicitly confirmed.

A second practical challenge is stability. While graphene has excellent stability in inert environments,[31] it is less stable under oxidizing conditions. Preliminary studies have shown that the interior of a grain of CVD-graphene will degrade rapidly at 400 °C in air.[98, 99] Degradation in ambient at temperatures < 400 °C may be possible but has not been elucidated in detail. Grain boundaries and defects are expected to further decrease stability. Xu *et al.* have shown *via* modeling that the oxidative etching of graphene at a defect site is expected to be faster than at a non-defect site.[100] Duong *et al.* have experimentally shown that grain boundaries in CVD-graphene on Cu can be probed when it is exposed to UV radiation in ambient because UV-generated O and OH radicals will selectively react with and degrade the graphene grain boundaries thereby providing an enhanced pathway for the oxidization of the underlying Cu substrate.[101] In general, if there is instability and degradation of graphene or its grain boundaries under a particular set of conditions then this will further limit the applicability of graphene as a diffusion barrier under these conditions.

Here, in order to gain more insight into these aspects, we have used imaging Raman spectroscopy to conduct detailed measurements of the oxidation of Cu through single and multiple layers of graphene, grown *via* CVD. We have used imaging Raman spectroscopy, in particular, as a tool to map where the oxidation occurs and to also track how both the oxidation and stability of the graphene evolve with time.

2.2 Results and Discussion

The graphene barriers for our studies were grown one layer at a time on Cu foils using standard atmospheric pressure CVD commonly used to grow monolayer graphene.[45, 53] Here, we refer to single layered graphene (SLG) on Cu by the abbreviation, SLG*x*1_Cu. Two-layered (SLG*x*2_Cu) and four-layered (SLG*x*4_Cu) samples were fabricated by mechanically transferring additional layers of graphene onto the SLG*x*1_Cu with the help of a sacrificial layer of poly(methyl methacrylate), using a transfer approach derived from that of Li *et al*., Safron *et al.*, and others for transferring graphene to arbitrary substrates.[14, 34, 102] All multi-layered samples were fabricated using graphene with 3 μm grains. The motivation behind independently growing then post-synthetically stacking the layers was to ensure a misalignment of microscopic and atomic-scale defects in each layer. The graphene on Cu samples (collective term for SLG*x*1_Cu, SLG*x*2_Cu and SLG*x*4_Cu) and control Cu samples without graphene were heated on a hotplate set to 200 °C in ambient atmosphere for up to 10 hours, in order to induce oxidation. A temperature of 200 °C was used to ensure rapid Cu oxidation kinetics and to match the work of Chen *et al.*[82] After oxidation, the samples were imaged using Scanning Electron Microscopy (SEM) and the oxidation of the Cu was quantified temporally and spatially using imaging Raman spectroscopy. Cu_2O was specifically mapped *via* its well established Raman mode at ~647 cm^{-1} and grain boundaries and defects in graphene were mapped by the D-band Raman mode at ~1345 cm^{-1}.[64, 71, 103-105] To quantify oxidation for the kinetics studies, the Cu_2O Raman intensity was averaged spatially over a 20 x 20 μm^2 region for the 3 μm grain size and a 30 x 30 μm^2 region for 14 μm sized grains. In order to independently confirm the Raman data, X-ray Photoelectron Spectroscopy (XPS) and X-ray excited Auger Electron Spectroscopy (XAES) were performed on a subset of samples, although the approaches only provide macroscopic averages of the degree of Cu oxidation (see Figures A.S1-3 and Table 1 in the Supplementary Information).

Figures 2.1a-d show electron micrographs of annealed Cu foil without graphene and SLG*x*1_Cu, SLG*x*2_Cu and SLG*x*4_Cu substrates, respectively, prior to oxidation. The bare annealed Cu foil was polycrystalline and relatively smooth, and the morphology of the graphene modified Cu substrates was similar. The regions of darker contrast in the images of the graphene modified Cu show the partial growth of additional layers. For example, the regions of darker contrast in the SLGx1 image (Fig. 2.1b) correspond to partial 2nd layers.

Figures 2.1e-h show electron micrographs of annealed Cu foil without graphene and SLG*x*1_Cu, SLG*x*2_Cu and SLG*x*4_Cu substrates, respectively, after 240 minutes of annealing in air. The surface of the Cu foil without graphene nearly completely oxidizes and becomes considerably rougher. In contrast, there is significantly less oxidation or perturbation of the graphene on Cu samples. Two features are observed in the SLG*x*1_Cu samples: (i) an interconnected network or grain boundary-like web of oxidation and (ii) oxidation along horizontal striations. The former resembles the observations of Chen *et al.*, which we later confirm correspond to oxidation of the underlying Cu directly through graphene's grain boundaries, *via* Raman mapping. The latter occurs at macroscopic striations in the Cu foil that result from the foil's processing and manufacture that translate into defects/steps into the structure of the graphene. In principal, these striations could be eliminated prior to CVD.

In comparison to the SLG*x*1_Cu samples, there is considerably less oxidation of the SLG*x*2_Cu samples and SLG*x*4_Cu samples (Fig. 2.1g and 2.1h) where the oxidation furthermore occurs in a different way. The Cu oxidation is limited to single points in SLG*x*2_Cu samples whereas considerable oxidation is not observed at all in SLG*x*4_Cu samples. Qualitatively, the improved barrier performance of the multi-layers makes sense as the microscopic and atomic-scale defects in each layer will be incommensurate, which is discussed further later.

The degree of oxidation of each of these four samples is more quantitatively compared in **Figure 2.2a**, using Raman spectra to assess copper oxide yield spatially averaged over a 20 × 20 μm^2 region. The spectrum of the highly oxidized bare foil is dominated by an intense feature at 647 cm^{-1} corresponding to Cu_2O and smaller peaks at 500 cm^{-1} and 800 cm^{-1} for CuO and

$Cu(OH)_2$ respectively. In comparison, the Cu_2O Raman feature is 41, 73, and > 403 times weaker on the SLG*x*1_Cu, SLG*x*2_Cu, and SLG*x*4_Cu, respectively. In the SLG*x*4_Cu sample, the graphene G- and 2D-band Raman features are visible at ~1585 cm^{-1} and ~2670 cm^{-1}, respectively, but the Cu_2O Raman feature is immeasurable, below the noise. It should be noted that that the 2D/G ratio of the SLG*x*2_Cu and SLG*x*4_Cu spectra are decreased with respect to that of the SLGx1_Cu sample. This decrease is observed both before and after annealing at 200 °C and can be attributed inter-layer interactions between domains of graphene that are randomly oriented.[65, 106, 107]

To better understand how the oxidation yield of each of these samples evolves, we measured similar Raman spectra as a function of time at intervals up to 610 min of oxidation (Fig. 2.2). The kinetics plots show that the amplitude of the Cu_2O Raman feature increases rapidly on the bare Cu sample, saturating after only ~5 min (Fig. 2.2a). In contrast, the amplitude of the Cu_2O Raman feature increases much more slowly on the graphene on Cu samples, although the increase is not linear. For example, at first, the increase in amplitude of the Cu_2O Raman feature on the SLG*x*1_Cu substrate is 290*x* slower than the bare Cu substrate. But, after ~60 min, the oxidation accelerates. Then, after ~240 min, the oxidation tends to saturate but at only ~10% of the amplitude of the bare Cu substrates. The mechanisms responsible for these three regimes of oxidation are discussed further later.

The kinetics plots for the SLG*x*2_Cu and SLG*x*4_Cu samples show that the rate of Cu oxidation is increasingly suppressed with an increasing number of sheets. In particular, at any given time, the overall degree of oxidation of the SLG*x*2_Cu and SLG*x*4_Cu samples is less than that of SLG*x*1_Cu samples. Furthermore, the onset of the accelerated degradation is delayed. For example, the first clearly measurable signature of oxidation of the SLG*x*4_Cu samples is not observed until 610 min. In all of the graphene on Cu samples, however, while the initial rate of oxidation was slow, it accelerated with time. Figure 2.2b compares the Raman spectra after 240 min of oxidation for the bare copper and the graphene on Cu samples. It can be easily noted from these spectra that the intensity of the Cu_2O peak (647 cm^{-1}) is reduced as the number of graphene layers on Cu is increased. The broad background / interference patterns between 400 – 1000 cm^{-1}, 1200 – 1900 cm^{-1} and 2500 – 3100 cm^{-1} are from the substrate (Cu).

In order to better understand the pathways for oxidation through single and multiple sheets of graphene, we collected Raman maps and electron micrographs of the samples at fixed oxidation times. We first analyzed a SLG*x*1_Cu sample prior to oxidation (see Figures A.S4-5 in the Supplementary Information). We then analyzed a SLG*x*1_Cu after 120 min of oxidation. A map of the Cu_2O Raman feature intensity at 647 cm^{-1} and a corresponding optical micrograph of the same region confirm that the web of topographical features observed optically and in the SEM are indeed Cu_2O (**Fig. 2.3a** and inset). The Raman mapping offers the possibility for not only mapping the spatial distribution of Cu_2O but for also mapping the spatial distribution of defects in the graphene *via* its D-band, at the same time. Toward this end, we measured high resolution Raman spectra at a number of points along a line intersecting one of the oxide features (Fig. 2.3b, inset). The resulting two-dimensional Raman map (with color intensity normalized to the graphene G-band) is shown in Figure 2.3b, whereas Figure 2.3c presents the intensity of the Cu_2O (647 cm^{-1}) and the D-band spectral features (normalized to the G peak) as function of position. The data show that the Cu_2O is commensurate with a concentration of defects in the graphene. This data taken together with knowledge of the characteristic grain-size of the graphene (3 μm) conclusively confirms that oxidation through single layers of graphene occurs primarily through its grain boundaries, thereby resulting in oxide directly underneath them.

It then follows that in multi-layered samples, these "line-of-sight" pathways would be reduced primarily to a set of points where the defect/grain boundaries of all the stacked layers coincide. For example, oxidation through two layers would be reduced to a set of points only where the grain boundaries of the two stacked layers intersect. Oxidation through multiple layers also has the possibility of proceeding *via* a second mechanism, which is *via* lateral-diffusion pathways, where oxygen penetrates through the defect/grain boundary of the topmost layer and laterally diffuses between two graphene layers until it finds a defect/grain boundary in the second layer and so on until it reaches the surface of the Cu. Oxidation *via* the former can be easily observed in Figure 2.1g, whereas oxidation *via* the latter can be seen as faint white dotted lines (Fig. 2.3d) indicating Cu oxidation at the grain boundaries of the layer in contact with the Cu (as seen through the overlying layer).

If the primary mode of oxygen transport through graphene is *via* its grain-boundaries, then it should be possible to engineer improved graphene barriers by controlling grain-size, which we demonstrate in **Figure 2.4**. We varied the grain-size of graphene by adjusting the growth temperature and the carbon concentration during the CVD process. The average grain-sizes were calculated by measuring the spatially averaged inter-nucleation distance from partial growths under the same conditions. For this particular aspect of our study, we used SLG*x*1_Cu with grain sizes (or inter-nucleation distances) of 3 μm and 14 μm (Fig. 2.4a and 2.4b, respectively). After annealing for 240 minutes, one can observe the formation Cu_2O on both of the SLG*x*1_Cu's at their respective grain boundaries (Fig. 2.4c and 2.4d, respectively). The average grain-size observed by the formation of the Cu_2O compares very well with our measurements of inter-nucleation distance. Figure 2.4e depicts the oxidation kinetics as a function of grain-size. The onset of oxidation occurs at roughly 90 min in both samples, but the oxidation saturates at roughly

20% of the intensity in the SLGx1_Cu sample with 14 μm grains compared with the sample with 3 μm grains. It can be inferred from the plot that the rate and degree of oxidation through a single layer of graphene are both linearly related to its defect/grain boundary density.

The kinetics plots in Figure 2.2 and 2.3e all generally tell a similar story, in which the oxidation evolves over time in three regimes, which are labeled in Figure 2.3e. At short times (regime I), the rate of oxidation is slowest. At moderate times (regime II), the rate of oxidation rapidly increases. Finally, at long times (regime III), the Cu_2O peak intensity tends to saturate. The latter saturation can be attributed to a self-passivation of the Cu under the graphene grain boundaries by already-formed Cu_2O, after it becomes sufficiently thick. What is not immediately clear, however, is the mechanism for the acceleration of oxidation in regime II. Our hypothesis is that the graphene itself degrades at 200 °C, thereby introducing new defects that accumulate with time, providing additional transport pathways through each sheet of graphene and accelerating oxidation.

Previous experimental studies have shown that the defect density and doping of CVD grown graphene increase with temperature and annealing time rapidly over 400 °C.[98, 99, 108] To study the stability of the polycrystalline CVD-graphene at only 200 °C, by itself off of the Cu substrate, we transferred a single layer of graphene onto a SiO_2/Si substrate and annealed it for 240 min in air. The defect density was monitored using Raman Spectroscopy as a function of time. The integrated D/G Raman ratio, spatially averaged over a $30 \times 30\ \mu m^2$ region, was initially 0.05, which is typical of CVD-graphene (**Fig. 2.5a**). After annealing for 120 min, the integrated D/G Raman ratio increased marginally to 0.06. However, after 240 min, the ratio increased to 0.19, indicating the formation of new defects. The positions of the G and 2D peaks also up-shifted with time during annealing (Fig. 2.5b). Previous work[109] has shown that this up-shift can be attributed to a change in doping arising from oxygen and moisture exposure or coupling of the graphene layer to the substrate. Determining the exact mechanism for the decomposition of CVD-graphene with increasing temperature will be the focus of a future study. Nonetheless, this decomposition accounts for the accelerated Cu oxidation in regime II and indicates that the performance of polycrystalline graphene as a diffusion barrier at 200 °C is limited by its instability.

Thus, overall, we believe that in regime I, the oxidation primarily occurs *via* the defects and grain boundaries that existed in the (as-grown) graphene prior to the 200 °C annealing, or in other words, *via* the defects inherent to CVD-graphene. With time, these defects and grain boundaries themselves degrade and new defects are formed, further enhancing mass transport through the graphene layers – which result in a rapid increase in the Cu_2O peak intensity with annealing time in regime II. Eventually, in regime III, the Cu oxidation becomes limited not by transport through the graphene barrier layers but rather by slow transport through the existing Cu_2O, itself. Perhaps the most interesting aspect is regime I because it suggests that if the stability of the CVD-graphene can be maintained (for example, possibly at lower temperature) then substantially superior barrier performance may be achievable. In fact, in this case, the ultimate barrier performance may be even better than what we observe in regime I, here, because it is likely that in reality there is not a sharp transition between regime I and II but rather a continuous build-up of defects with time, starting as soon as at t=0. More detailed studies of the stability of polycrystalline CVD-graphene and the mechanisms for its degradation as a function of temperature are needed to confirm these hypotheses.

2.3. Conclusion

We have utilized imaging Raman spectroscopy in conjunction with electron microscopy to better understand how the oxidation of Cu passivated by single and multiple layers of graphene, grown by chemical vapor deposition (CVD), evolves temporally and spatially. At 200 °C in air, Cu oxidation proceeds in 3 regimes: first slowly *via* transport through atomic-scale grain boundary defects inherent to CVD-graphene; secondly more rapidly as the graphene itself degrades and new defects are formed; and finally the oxidation saturates after the Cu_2O reaches a sufficient thickness to limit transport. The degradation limits high temperature barrier applications; however, initially, the graphene passivates substantially better than previously reported, suggesting better low temperature performance. The Raman maps establish that oxidation through single sheets occurs through graphene's grain boundaries, whereas oxidation through multiple sheets occurs *via* first at their intersection and then more slowly *via* lateral-diffusion between layers. Performance further increases with grain-size; for example, increasing grains from 3 μm to 14 μm decreases the oxidation rate by an additional factor of ~5 per sheet, suggesting additional gains in performance will be possible with improved graphene crystal growth. Overall, this study is expected to improve the understanding of transport through CVD-graphene and lead to improved large area graphene materials for barrier applications.

2.4. Experimental

Preparation: The graphene barriers for our studies were grown one layer at a time on Cu foils using standard atmospheric pressure chemical vapor deposition (CVD) commonly used to grow monolayer graphene. [45, 53] Prior to CVD, the Cu foils (Alfa Aesar 99.8% Lot # 13382) were annealed in a reducing forming gas environment (17 sccm H_2, 320 sccm Ar) at their respective growth temperatures for 30 min. The growth of graphene with 3 μm grains was achieved by adding a 0.360 sccm CH_4 flow for 240 min at 972 °C. The growth of graphene with 14 μm grains was initiated by adding a 0.250 sccm CH_4 flow for 240 min at 1030 °C. Control bare Cu samples without graphene were produced by annealing in forming gas at 972 °C for 270 min but never introducing methane. Two-layered (SLG*x*2_Cu) and four-layered (SLG*x*4_Cu) samples were fabricated by mechanically transferring additional layers of graphene onto the SLG*x*1_Cu with the help of a sacrificial layer of poly(methyl methacrylate), using a transfer approach derived from that of Li *et al.*, Safron *et al.*, and others for transferring graphene to arbitrary substrates.[34, 102] Oxidation was carried out on a hot-plate set to 200 °C in air. The ambient temperature = 23.5 °C and the relative humidity was 32 – 37%.

Characterization: After oxidation, the samples were imaged using Scanning Electron Microscopy (SEM LEO 1530, 3 keV) and optical microscopy. The oxidation of the Cu was quantified temporally and spatially using imaging Raman spectroscopy (DXR Raman Thermo Fisher Scientific, excitation $\lambda = 532$ nm, 1 mW). The step size of the scans was 1 μm and the laser spot size was also ~1 μm. The laser power and exposure time were sufficiently low that the Raman laser did not induce oxidation of the Cu during measurement. The amplitude of the Cu_2O component of each Raman spectrum was determined by fitting. Each spectrum was fit from 450 – 850 cm^{-1} using the Raman spectrum of the oxidized bare Cu sample as a reference spectrum for Cu_2O and a sixth order polynomial to account for the broad background and interference effects. The full-width at half-maximum of the main Cu_2O peak at 647 cm^{-1} was only 50 cm^{-1} and could not be reproduced by the polynomial background, which was forced to fit over the entire 450 – 850 cm^{-1} range. Thus, this fitting protocol successfully was able to extract the Cu_2O component of each spectrum. X-ray Photoelectron Spectroscopy (XPS) and X-ray excited Auger Electron

Spectroscopy (XAES) studies were performed using Perkin Elmer 5400 XPS (ESCA- electron spectroscopy for chemical analysis) with a Mg X-ray source (15 kV, 300 W).

Acknowledgement

This work was supported by National Science Foundation (Grant# CBET-1033346). MSA also acknowledges partial support from a 3M Non-Tenured Faculty Grant.

Figures and Captions

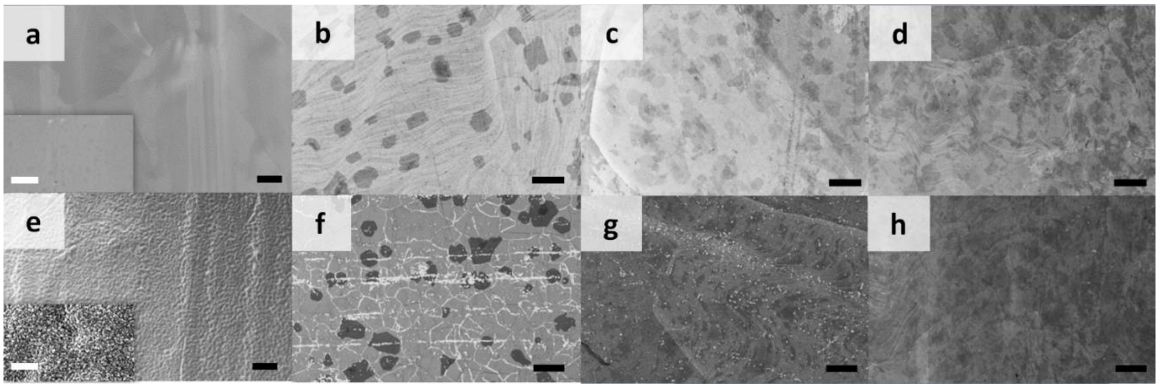

Figure 2.1. SEM images comparing bare Cu, SLG*x*1_Cu, SLG*x*2_Cu and SLG*x*4_Cu before oxidation (a-d, respectively) and after 240 min in air at 200 °C (e-h, respectively). Scalebars = 10 μm. Insets in (a) and (e) depict SEM images of wider areas. Scalebars = 1 μm.

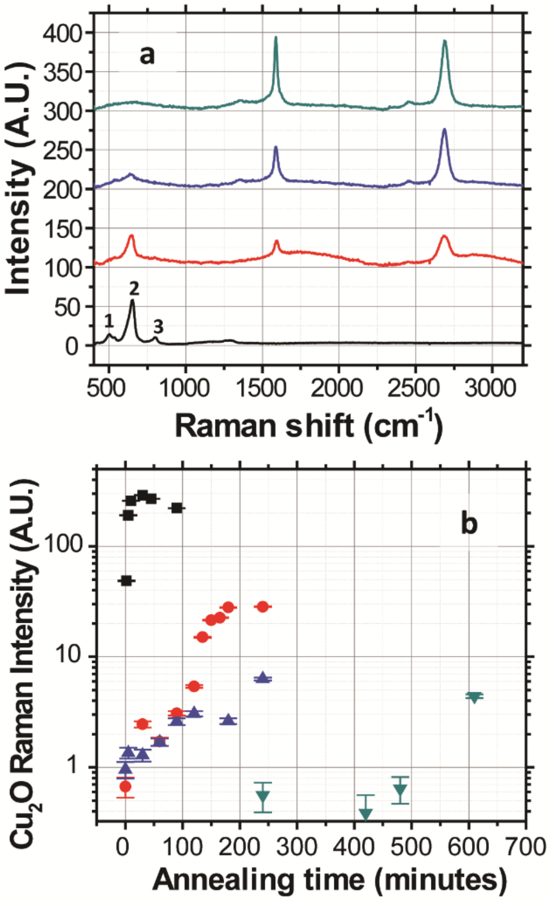

Figure 2.2. (a) Raman spectra of bare Cu, SLG*x*1_Cu, SLG*x*2_Cu, and SLG*x*4_Cu after 240 min in air at 200 °C, offset from bottom to top, respectively. (Legend for bare Cu spectra: 1 – 500 cm^{-1} (CuO), 2 – 647 cm^{-1} (Cu_2O), 3 – 800 cm^{-1}($Cu(OH)_2$) (b) Kinetic evolution of the Cu_2O Raman feature at 647 cm^{-1} for bare Cu (black squares), SLGx1_Cu (red circles), SLGx2_Cu (blue triangles) and SLGx4_Cu (inverted triangles). Error bars depict ± one standard deviation in fitting certainty of the amplitude of the Cu_2O Raman feature.

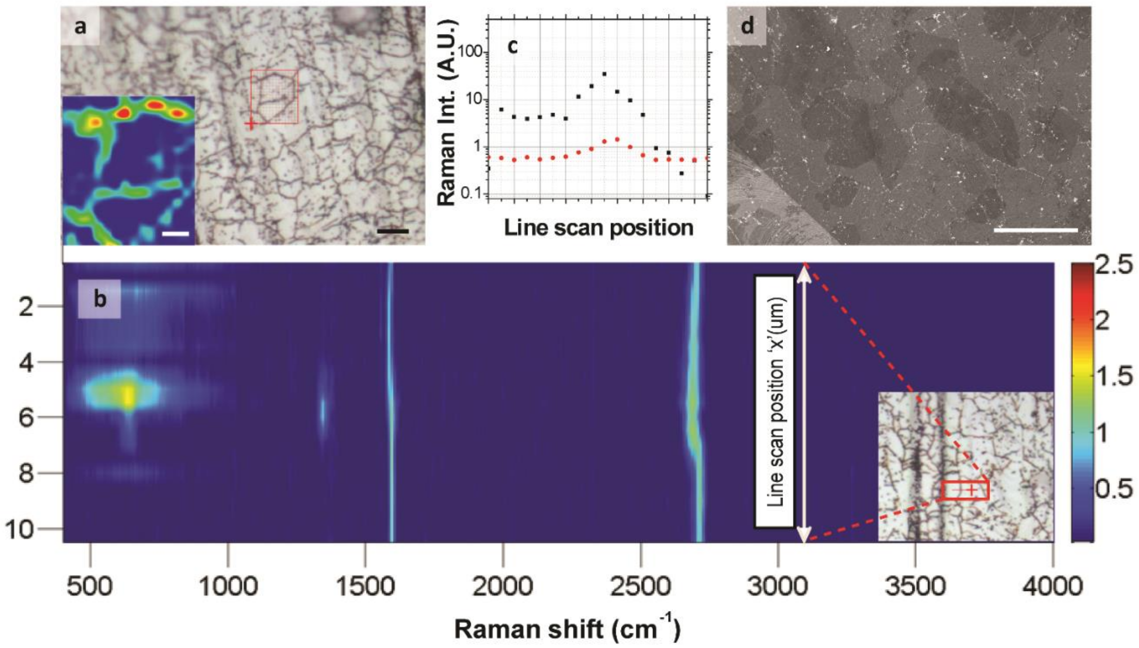

Figure 2.3. (a) Optical micrograph highlighting the Cu oxide features on SLGx1_Cu after 120 min (scalebar = 10 μm). Inset maps the Cu_2O Raman intensity in the region of part (a) highlighted red (scalebar = 3 μm). (b) Raman line-scan across a Cu oxide feature (inset – red line), normalized to the intensity of the G-band at each point along the line-scan. (c) Cu_2O peak intensity (black squares, right-axis) and integrated D/G ratio (left-axis) as a function of position, extracted from the Raman line-scan in part (b). The Cu_2O peak intensity was extracted from the Raman scattering signal at 647 cm^{-1} from the line-scan from part (b) and the integrated D/G ratio was extractetd by integrating the Raman signal due to the D-peak at 1345 cm^{-1} and dividing by the integrated Raman signal due to the G-peak at 1585 cm^{-1} from the line-scan from part (b). (d) SEM of oxidized SLGx2_Cu sample. The faint white lines are Cu oxide resulting from lateral diffusion between the two graphene layers and the subsequent oxidation of the Cu at the grain-boundaries of the graphene layer immediately in contact with the Cu (scalebar = 10 μm).

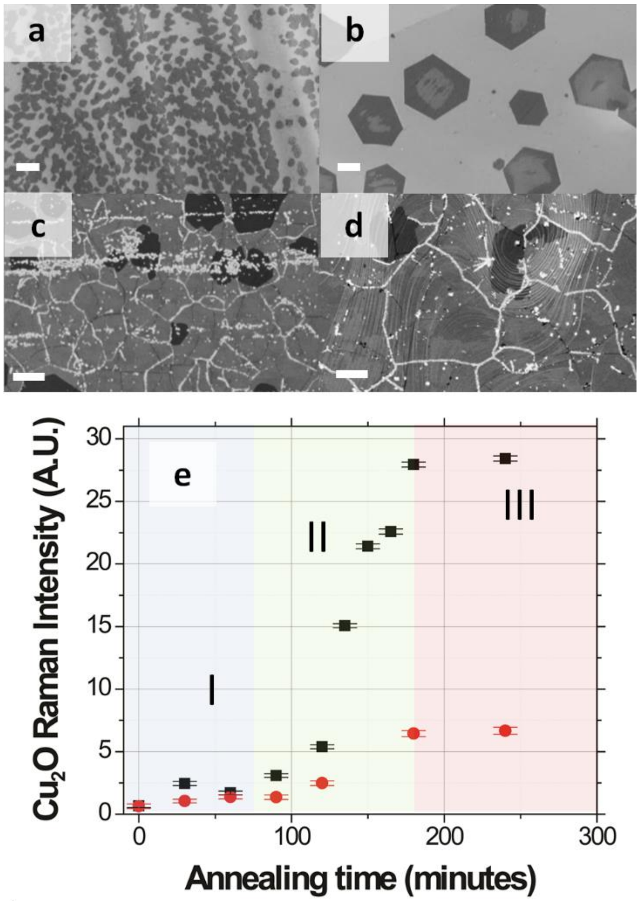

Figure 2.4. (a) and (b): SEM images showing the nucleation density for partially grown graphene monolayers at 972 °C and 1030 °C, respectively (scalebars = 5 μm). (c) and (d): SEM images of fully grown graphene layers at 972 °C and 1030 °C after 240 min of annealing on Cu at 200 °C in air. The underlying Cu locally oxidizes underneath grain boundaries in the overlying graphene indicated by the white features in the image. (e) Grain size or defect density dependence of transport through a single layer of graphene: Black-squares and red-circles represent the oxidation kinetics of SLG*x*1_Cu with 3 μm grains and SLG*x*1_Cu with 14 μm grains, respectively. Error bars depict ± one standard deviation in fitting certainty of the amplitude of the Cu_2O Raman feature.

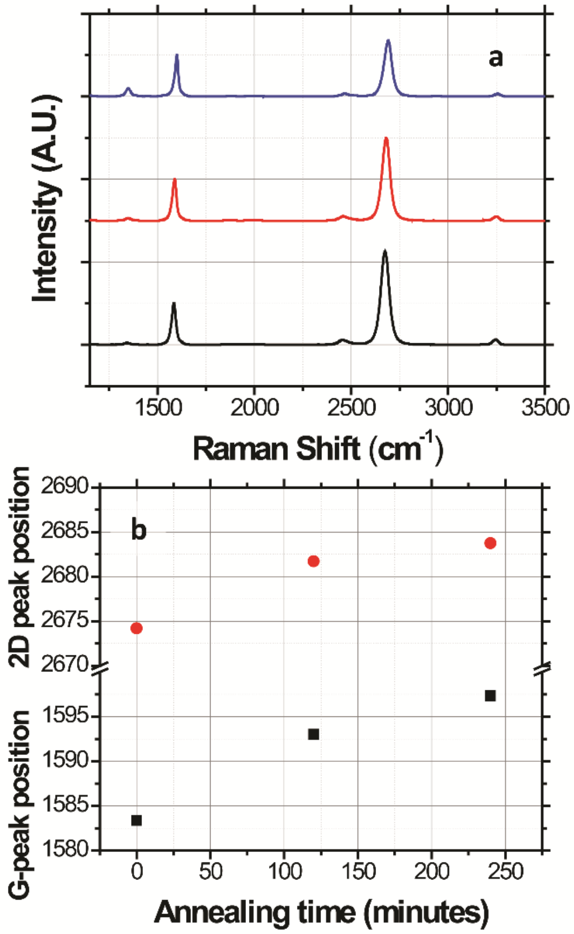

Figure 2.5. (a) Raman spectra of CVD-graphene (normalized to G-band) on SiO_2/Si after 0 (bottom), 120 (middle) and 240 min (top) of annealing in air at 200 °C. (b) Spectral shift of the G and the 2D Raman modes with annealing time, indicating an increase in doping with time.

3. Quantifying degradation of graphene in ambient

This chapter was adopted from “Singha Roy. S.; Safron, N. S.; Wu, M.-Y.; Arnold, M. S., Evolution, kinetics, energetics, and environmental factors of graphene degradation on silicon dioxide. *Nanoscale* **2015,** 7, (14), 6093-6103.” SS synthesized and transferred graphene, performed all the oxidation tests, Raman studies and SEM imaging, fabricated FETs and analyzed all the data for this study. NSS performed the FET based charge carrier concentration and mobility measurements. MYW wrote the code for analyzing the images for the grain boundary etching study.

Abstract

Recent studies have qualitatively shown that the oxidative stability of monolayer graphene integrated on oxides is relatively poor. Here, the evolution, kinetics, and energetics of this degradation is quantified. Specifically, the deterioration of graphene on SiO_2 is studied in grain interiors and at grain boundaries in ambient air, dry air and nitrogen between 473 and 673 K, using spatially and temporally resolved in situ Raman spectroscopy in addition to electron microscopy and charge transport measurements. The grain interiors of chemical vapor deposition (CVD) grown graphene monolayers oxidize with an activation energy of 0.63 ± 0.05 eV in ambient (15,000 ppm H_2O). This energy increases to 1.85 ± 0.17 eV in dry air, whereas degradation is immeasurable in nitrogen and for multilayers even in ambient. Gasification at grain boundaries in CVD monolayer proceeds at a rate of $(1.08 \pm 0.02) \times 10^{-1}$ nm s^{-1} at 673 K with an activation energy $E_A = 1.14 \pm 0.10$ eV in ambient. The more facile degradation of the monolayer grain interiors in ambient indicates the role of the substrate in decreasing stability against oxidation. Electrical transport mobility decays with an activation rate similar to that of grain

interiors. These results can be used to quantitatively predict graphene oxidation and gasification on SiO_2 in different environments and temperature.

3.1 Introduction

The integration and support of graphene on a substrate is a necessary aspect of exploiting this two-dimensional material with exceptional properties in next generation electronic and optoelectronic applications. A majority portion of the device architectures that have already been proposed and demonstrated specifically use glass, SiO_2, or other oxides as supporting substrates.[70, 91, 108, 110-114] One potential challenge with using oxides as substrates, however, is that the chemical stability of single layers of graphene integrated on them is relatively poor.[115-118] For example, it has been qualitatively observed that single layers of graphene degrade faster and at lower temperature on SiO_2/Si substrates than graphene on non-polar substrates or graphene that is suspended.[115] Sharma *et al*. have previously shown that on SiO_2/Si, a single layer graphene is chemically more reactive to aryl diazonium reactants than bi-layer graphene.[116] In a recent study, Yamamoto *et al*. qualitatively observed that charge inhomogeneity on the supporting substrate’s surface enhances the oxidation of a mechanically exfoliated graphene monolayer and reported that single layers of graphene on SiO_2 also oxidize faster than multiple layers of graphene.[117] Furthermore, they observed an increased sensitivity of graphene monolayers to oxidation on a rougher SiO_2 nanoparticle film compared to on a smoother thermally grown SiO_2/Si film, suggesting that an increased substrate surface roughness can also increase the rate of oxidation. While these qualitative studies serve as an important proof-of-principle, a better quantitative understanding of this relatively poor oxidative stability of monolayer graphene on SiO_2 and similar oxide and polar substrates is needed to guide the engineering of future graphene based devices.

Here, we quantify the degradation (i.e. oxidation and gasification) of single layers of graphene on SiO_2/Si substrates in order to learn more about this instability. SiO_2/Si substrates are used as representative oxide substrates because they have been used extensively in the past in graphene and graphene-based field-effect transistors (FETs) and other electronic/optoelectronic devices.[110-113] As shown in Figure 3.1, multiple mechanisms contribute to the degradation. In order to differentiate among them, we study the degradation using several techniques. We (i) quantify the rates and kinetics of degradation, (ii) spatially map where the degradation occurs, (iii) determine environmental factors favoring degradation, and (iv) quantify effective activation energies.

In Section 3.2.1, we employ temporally-resolved and spatially-averaged *in situ* Raman spectroscopy to compare the oxidation kinetics of single layers of graphene produced by two different methods: chemical vapor deposition (CVD) and mechanical exfoliation. This oxidation is studied under the influence of different atmospheric conditions between 473 and 673 K. It has been previously shown that (a) O_2 plays an important role in the deterioration of sp^2-bonded carbon materials and (b) H_2O vapor accelerates the degradation process,[60, 119-126] hence we investigate the role of each of these species. Specifically, we vary the *in situ* atmospheric environment from (i) humid air to (ii) desiccated-dry air to (iii) nitrogen (N_2). In Section 3.2.2, in order to map where the oxidation and gasification take place, we use *ex situ* spatially-resolved imaging Raman spectroscopy (IRS). With the help of these techniques we show that the activation energy measured in Section 3.2.1 corresponds to intra-grain oxidation (i.e. the process depicted in Fig. 3.1i). In Section 3.2.3, we quantify the temperature dependence of the etch rate at grain boundaries (i.e. the process depicted in Fig. 3.1iii-iv) using time resolved scanning electron microscopy to determine the activation energy for gasification at receding grain edges.

Finally (Section 3.2.4), to relate the deterioration to the electronic properties of single layers of graphene, we quantify charge transport mobility and carrier concentration using *in situ*, temperature-dependent, field-effect transport measurements. Overall, this study will help in (i) understanding how environmental factors affect the integrity and properties of graphene, (ii) discerning the effect of the substrate on inducing defects in graphene, (iii) learning the limitations of graphene for applications which operate under either elevated temperature or in ambient conditions such as gas-sensors, electrodes, or diffusion barriers, and (iv) overcoming these limitations.

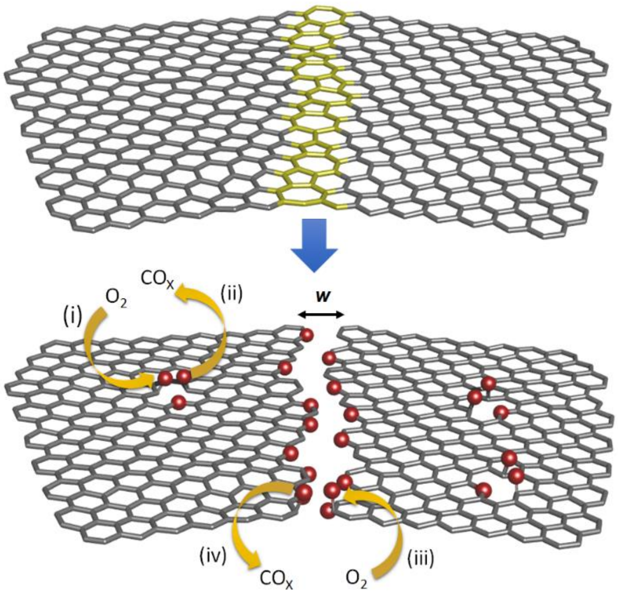

Figure 3.1: Schematic of degradation processes. Top: As-manufactured graphene with grain boundaries highlighted in yellow. Bottom: Graphene following degradation. Red represents oxygen atoms. Two modes of degradation are observed in this paper. One occurs in the grain interiors via oxidation (i) and gasification (ii). The second occurs at the grain boundaries and edges via oxidation (iii) and gasification (iv). Several different forms of oxygen functionalization are possible, with either CO or CO_2 as gasification byproducts.

3.2 Results

3.2.1. Temporally-resolved and spatially-averaged *in situ* Raman spectroscopy

Here, we use *in situ* Raman spectroscopy to quantify the accumulation of defects in graphene as it oxidizes with time (Fig. 3.1i), as a function of temperature between 473 and 673 K, in humid air, desiccated-dry air, and nitrogen. We quantify the defect density by measuring the ratio of the integrated Raman scattering intensity of the D-band (~1345 cm^{-1} at 532 nm excitation) mode of graphene to the integrated Raman scattering intensity of the G-band mode (~1590 cm^{-1} at 532 nm excitation), I_D/I_G. At low defect density with an inter-defect separation, L_d, that is >> 4 nm, I_D/I_G is linearly proportional to the defect density and thus can be used to compare defect densities as a function of time and conditions and between different samples. In contrast at high defect density, as L_d decreases and becomes comparable to 4 nm, I_D/I_G increases and then saturates at a maximum of 3 (for a Raman excitation wavelength of 514.5 nm).[63, 127] To assure that we are confined to or near the linear regime, our time-resolved degradation experiments are terminated before an I_D/I_G of 2 is reached. The spatial resolution of the technique is determined by the laser spot-size, which is ~700 nm. Substrate-induced topological features and charge inhomogeneity are expected to vary on a much finer lateral length scale of ~ 10 nm.[115, 117, 128] It is also important to point out that I_D/I_G does not depend on the nature or the geometry of the defect (within the Raman spectrometer resolution) but only depends on the overall density, as previously shown by Eckmann *et al.*,[73] thus giving us an ideal way to quantify the density without having to separately account for contributions due to each type of defect. An *in situ* Raman heated-stage enclosure (Linkam THMS 600) is used to control the temperature of the sample and the atmosphere around it. To regulate the atmosphere, two different *in situ* experimental setups are used: (i) an open-lid setup is used to characterize degradation in humid air in which the sample is exposed to ambient humid air while being heated and (ii) a closed-lid set-up is used to confine the sample's ambient to desiccated-dry air and nitrogen. The Raman spectra are spatially averaged over a 100 x 100 μm^2 area.

We first study the oxidation (Fig. 3.1i) of graphene grown by atmospheric pressure CVD. The graphene is grown on Cu from CH_4 and transferred to SiO_2/Si via a standard sacrificial polymer approach using a thin film of poly(methyl methacrylate) to support the graphene during the removal of the Cu growth substrate/catalyst in ammonium persulfate (25% Transene company, Inc. APS-100 + 75% DI water) Cu etchant.[34, 91] After transfer to SiO_2/Si, the poly(methyl methacrylate) is removed in acetone followed by rinsing in isopropyl alcohol and subsequently air-drying. The graphene on SiO_2/Si is then transferred to the Raman instrument and characterized.

Figure 3.2a shows the Raman spectra of monolayer graphene on SiO_2 spatially averaged over a 100 x 100 μm^2 area and normalized to the G-band intensity. The average I_D/I_G is measured for the area is 0.05. When the sample is annealed in ambient air at 573 K, the I_D/I_G starts increasing with time. Figure 3.2b and c show representative Raman spectra of the sample after 5k seconds and 10k seconds of annealing, respectively. The average I_D/I_G of the same area increases to 0.26 and 0.48 after 5k and 10k seconds, respectively.

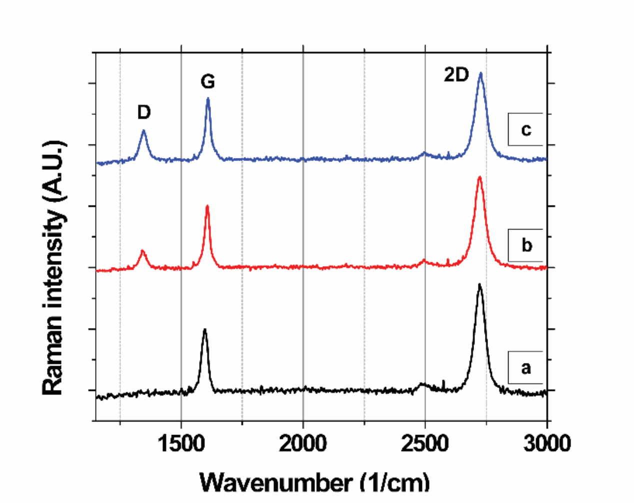

Figure 3.2: Evolution of spatially-averaged Raman spectra of the monolayer graphene normalized to the intensity of the G-band annealed at 573 K in ambient air. The I_D/I_G ratio increases from an initial value of 0.05 (a) to 0.26 (b) after being annealed for 5k seconds and then to 0.48 (c) after 10k seconds.

The evolution of I_D/I_G versus time is shown in Fig. 3.3a for CVD-grown graphene on Si/SiO_2 in humid air at a water vapor concentration of 15,000 ppm at 473, 573, and 673 K. At each temperature, I_D/I_G increases linearly with time, indicating that the defect density increases linearly with time.[129] The rate of increase becomes faster with increasing temperature. It is important to keep in mind that the contribution to I_D arises primarily from the grain interiors (Fig. 3.1i) as opposed to at grain boundaries (Fig. 3.1iii), as we show later in Section 3.2.2. An initial lag in the onset of the linear increase in I_D/I_G with time is observed (Fig. 3.3a inset) and potentially can be attributed to desorption of residual surface adsorbents and contaminants that might have originated from the transfer process. As shown in Fig. 3.3b, the rate of change, R, in the linear regime has an Arrhenius dependence with temperature, T, such that, $R = (\partial/\partial t)(I_D/I_G) = R_{673}\exp[(-E_A/k_B)(1/T - 1/673)]$ where R_{673} is a pre-exponential factor specifying the degradation rate at T = 673 K and E_A is the activation energy. The fit $R_{673} = (3.7 \pm 0.7) \times 10^{-4}$ s^{-1}

and the fit $E_A = 0.63 \pm 0.05$ eV, over the range of 473 to 673 K, where the error bars denote two standard deviations of certainty.

The above experiment is also performed for mechanically exfoliated graphene transferred onto SiO_2/Si to examine if the initial "quality" of the graphene affects the kinetics or energetics of oxidation (Fig. 3.1i). Unlike the mechanically exfoliated graphene, the CVD graphene is stitched together via defective grain boundaries. In addition, the superior transport characteristics of exfoliated graphene [130, 131] suggest that the initial concentration of defects is lower in exfoliated graphene than in CVD graphene grown on Cu foils under the conditions used here. Moreover, mechanically exfoliated graphene is also flatter and single crystalline whereas the topology of CVD-grown graphene contains wrinkles and maintains the memory of the "rough" Cu foil catalyst substrates and is polycrystalline (average grain size here is ~14 μm). The I_D/I_G for mechanically exfoliated monolayer graphene is measured over a smaller area of 2 x 2 μm^2 away from the edges of the flakes because of their limited size, in humid air at a water vapor concentration of ~12,000 ppm. The fit $R_{673} = (3.2 \pm 0.1)\ x\ 10^{-3}\ s^{-1}$ and $E_A = 0.79 \pm 0.01$ eV (Fig. 3c). While the small 20% difference in water vapor concentration between the experiments on CVD-graphene and mechanically exfoliated graphene preclude precise quantitative comparison, the relatively low E_A for both cases (compared with the much higher E_A measured in dry air, below), indicates that the "quality" of the graphene and intrinsic defects do not substantially lower the effective E_A in humid air on SiO_2/Si substrates. Rather, these data indicate the importance of extrinsic factors, for example graphene-substrate interactions, in driving the degradation.

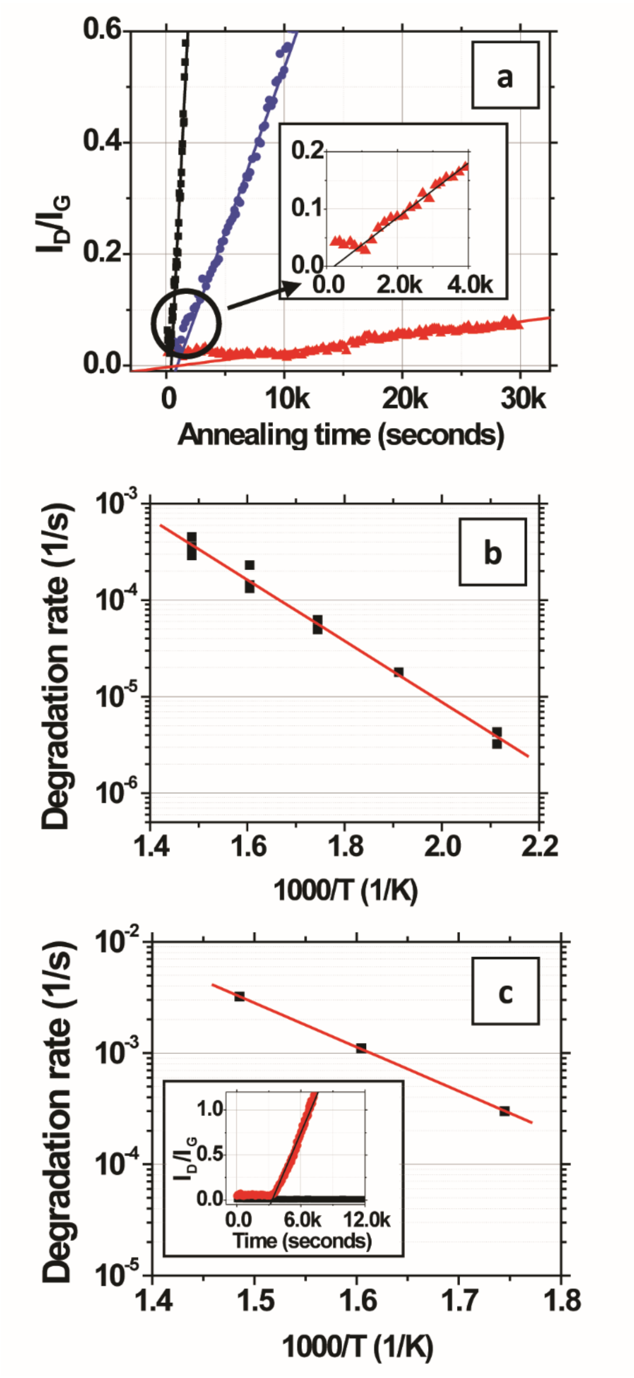

Figure 3.3: Rate and kinetics of degradation of monolayer CVD-graphene on SiO_2/Si. (a) Red-triangles, blue-circles and black-squares represent the evolution of I_D/I_G versus time in humid air (15,000 ppm H_2O) at 473 K, 573 K and 673 K, respectively. Inset: Initial lag in the onset of the linear increase in I_D/I_G with time. (b) Arrhenius dependence of degradation rate ($\delta(I_D/I_G)/\delta t$) with temperature (R_{673} = (3.7 ±

0.7) x 10^{-4} s^{-1} , E_A = 0.63 ± 0.05 eV) for CVD-graphene in humid air (15,000 ppm H_2O). (c) Arrhenius dependence of degradation rate ($\delta(I_D/I_G)/\delta t$) with temperature (R_{673} = (3.2 ± 0.1) x 10^{-3} s^{-1} , E_A = 0.79 ± 0.01 eV) for mechanically exfoliated graphene in humid air (12,000 ppm H_2O). Inset: Comparison of the evolution of I_D/I_G versus time for single (red) and multiple layers of mechanically exfoliated graphene (black) on SiO_2/Si at 623 K.

In contrast with single layer graphene, mechanically exfoliated few ($1<n<4$) layer graphene transferred to SiO_2/Si is much more stable in humid air. The inset in Fig. 3.3c compares the evolution of I_D/I_G versus time for single and multiple layers of graphene on SiO_2/Si at 623 K. Whereas I_D/I_G for the single layer increases rapidly with time, I_D/I_G for multiple layers does not measurably increase even after 3 hours. In both cases, the top layer of graphene is hot and exposed to the humid air. However, in the few layer sample, the top layer that is exposed to the humid air is isolated from the SiO_2 substrate by the underlying layers, which themselves are not directly exposed to the ambient environment. Thus, graphene isolated from the SiO_2 substrate oxidizes and gasifies very slowly even in humid air. These results suggest that substrate interactions play important roles in the degradation of single layers of graphene. While we cannot preclude the possibility that bi- or multi-layer graphene might be less reactive than single layer graphene, even in the absence of substrate-effects, it is well known that the different layers are coupled via a weak van dar Waals interaction with only minor electronic perturbation. Taking this argument into account, the most likely explanation for the decreased reactivity of the topmost layer of the multi-layer graphene is the isolation from the substrate. This explanation is further supported by the qualitative study of the chemical reactivity of graphene on various substrates by Yamamoto *et al.*[117]

It has been theoretically shown by Patra et al. that water can act as a catalytic element that initiates rapid conformational changes in single layers of graphene.[125] Also, experimental studies indicate that water has the ability to intercalate at the graphene-SiO_2 interface and deform the surface of the atomic membrane.[124, 126] These effects distort the graphene on the atomic scale creating deformation or curvature causing strain-induced pyramidalization, which is known to increase chemical reactivity.[132] Therefore cumulatively, it can be hypothesized that the critical role of water on oxides may be to strain and deform single layers of graphene thereby decreasing the activation energy for oxidation (Fig. 3.1i).

To probe the effect of water vapor further, we next study the effect of reducing its concentration on degradation rate and activation energy. In this case, we use the closed-lid setup and dry the wet ambient air using desiccants. The use of desiccants has the advantage of ensuring that the composition of the ambient air remains constant except for water vapor, which is reduced by the desiccants (as opposed to creating mixtures of dry N_2 and O_2 that are missing the other relevant components of ambient atmosphere like CO and CO_2). In the closed-lid setup, the humid ambient air is drawn through 3 cascaded drying tubes of desiccants (1*x* silica gel, Fisher Chemical product # S161-500 and 2*x* drierite, W.A. Hammond Drierite Indicating Drying Tube 8"L x ¾" O.D.) and then through the sample chamber by pulling a vacuum on the outlet port of the sample chamber. This approach reduces the water vapor concentration below the sensitivity of our hygrometer to < 2,000 ppm. We also conduct a control experiment in the closed-lid setup using humid air without desiccants to test if the flow of the gas over the substrate used in this closed-lid setup leads to differences in degradation compared to the open-lid setup used previously in which there was no forced flow. The humid air (water vapor concentration ~15,000 ppm) in the closed-lid setup yields a R_{673} = (7.8 ± 1.0) x 10^{-4} $s^{-1}$and an E_A = 0.71 ± 0.06 eV (Fig. 3.4a), which is similar to the E_A of 0.63 ± 0.05 determined previously in the open-lid setup.

The degradation rate is substantially slower in dry air. At 623 K, it is 100 times slower. The activation energy increases to E_A = 1.85 ± 0.17 eV (Fig. 3.4a) with R_{673} = (3.6 ± 0.4) x 10^{-5} s^{-1}, which is ~3 times E_A in humid air. Both the above observations with the dry air indicate that water vapor present in the air plays a vital role in the degradation process on SiO_2 which is consistent with the theoretical studies and qualitative observations made regarding conformational changes in the graphene on SiO_2 in humid but not dry air by other groups.[60, 124-126] Previous study has shown that water vapor can independently abstract C atoms from basal plane of graphite thereby creating new defects on the surface between 673 to 1573 K [133]; however, this effect seems to be secondary to substrate effects as evidenced by immeasurably slow degradation of the few layered graphene samples on SiO_2 in humid air (Inset Fig. 3.3c).

To further investigate the thermal stability of single layers of graphene on SiO_2, we measure the evolution of I_D/I_G in a nitrogen atmosphere (99.999% N_2, < 1 ppm O_2, < 1 ppm water vapor). As shown in Fig. 3.4b, no measurable degradation is observed at 623 K even after 7 hours of annealing, indicating that the quality of the graphene is unaffected even at elevated temperatures under inert conditions similar to previously reported by several groups.[31, 42, 67, 92, 134, 135]

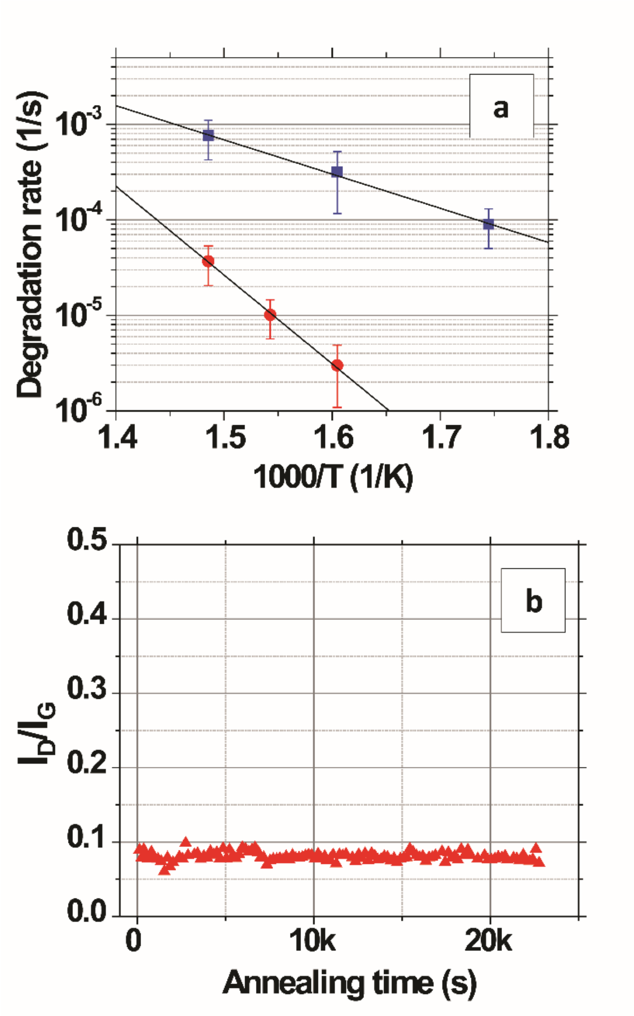

Figure 3.4: (a) Arrhenius dependence of degradation rate ($(\delta(I_D/I_G)/\delta t)$ with temperature of monolayer CVD-graphene on SiO_2/Si in humid air (blue-squares) and in desiccated-dry air (red-circles). $E_A = 0.71 \pm 0.06$ eV and $E_A = 1.85 \pm 0.17$ eV for CVD-graphene in humid air and desiccated-dry air, respectively. (b) Represents the evolution of I_D/I_G versus time in nitrogen (99.999%) for monolayer CVD-graphene on SiO_2/Si at 623 K.

3.2.2. Ex situ spatially-resolved imaging Raman spectroscopy (IRS)

Now that the rate and the activation energy for the oxidation of single layers of graphene on SiO_2 are known, we next investigate and visualize the degradation using imaging Raman spectroscopy

(IRS) microscopy. To compare the contribution to I_D/I_G from grain boundaries versus grain interiors, we imaged its spatial distribution using IRS at different times at 623 K in humid air. Figure 3.5a and b (insets) show optical images of the regions of graphene on SiO_2/Si scanned after annealing for 45 and 110 minutes, respectively. Etching and gasification along grain boundaries and smaller circular features (etch pits) are evident from the optical images. The IRS maps of these same areas are shown in Figs. 3.5a,b. After 45 minutes (Fig. 3.5a), the I_D/I_G is most intense at the grain boundaries. The graphene that has been etched and gasified at the grain boundaries (Fig. 3.1iii-iv) no longer contributes to this I_D/I_G because this carbon has been removed as CO and CO_2, but rather the carbon remaining at the edges of the graphene grains gives rise to the intense I_D/I_G signal. More importantly, substantial oxidation (Fig 3.1i) has also occurred within the grains. The average I_D/I_G at the grain boundaries (determined by averaging I_D/I_G ± 0.4 μm along each grain boundary) is 0.80 whereas the average I_D/I_G in the remaining grain interiors is 0.23. Even though I_D/I_G at the grain edges is higher, the area occupied by the grain interiors is much larger; therefore, the I_D/I_G spatially averaged over the entire image (=0.4) is actually dominated by the grain interiors. For example, spatially weighing, we find that 70% of the overall I_D/I_G comes from the interiors whereas only 30% of the I_D/I_G comes from the grain boundaries. Moreover, the I_D/I_G at the grain edges should remain invariant with time because new oxidation at the grain edges is accompanied by new gasification, as discussed in Section 3.2.3, below. Thus, the spatially averaged data and activation energies presented in Section 3.2.1 are indicative of the oxidation (Fig 3.1i) that occurs within the grains. After 110 minutes (Fig. 3.5b), the I_D/I_G at the grain interiors and the grain edges become indistinguishable and the integrated average of the ratio becomes ~1.0. The above results again highlight that the deterioration proceeds via two different processes that occur with different kinetics: (a) the oxidation of the grain interiors (Fig. 3.1i) and (b) oxidation and gasification at grain boundaries and edges (Fig. 3.1iii-iv). Whereas the kinetics of the oxidation of the grain interiors are quantified via Raman spectroscopy, above, the kinetics of the oxidation and gasification of grain edges are quantified in Section 3.2.3, below.

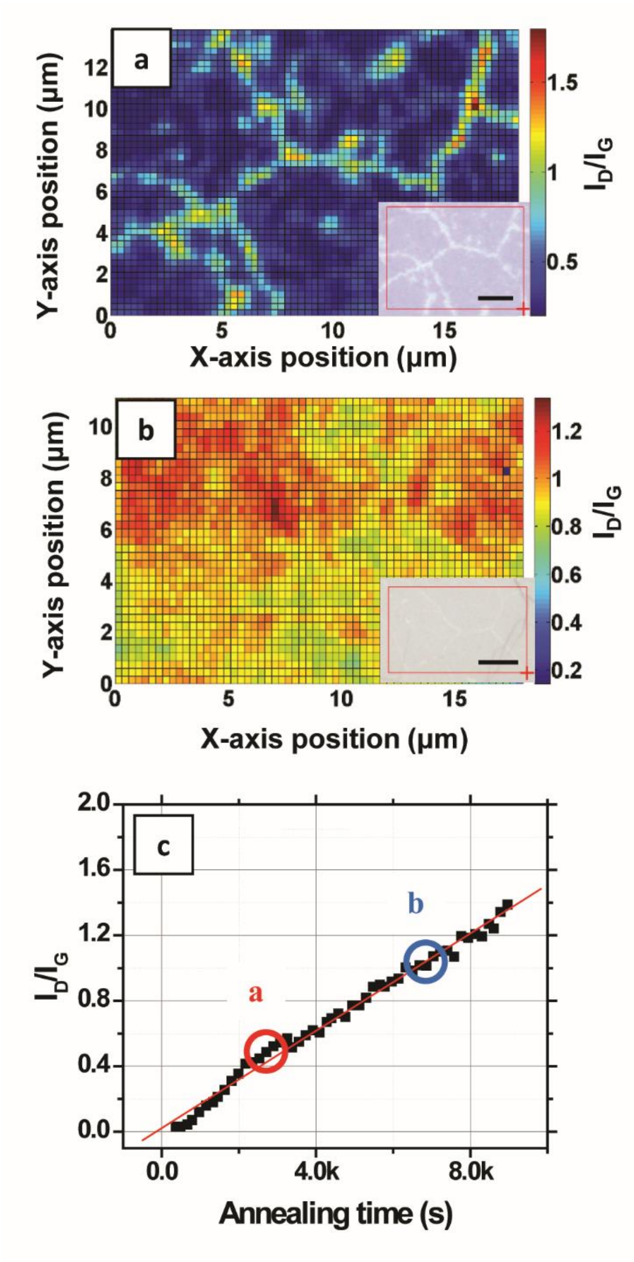

<u>Figure 3.5</u>: Temporally resolved imaging Raman spectroscopy depicting the progression of the degradation process. (a) Depicts the spatial distribution of I_D/I_G over regions of visibly etched grain boundaries (as seen in the inset) after a 45 min anneal in humid air (15,000 ppm H_2O) at 623 K and (b) depicts the same after 110 minutes of anneal (inset scalebars = 5 μm). (c) Represents the evolution of I_D/I_G versus time in humid air (15,000 ppm H_2O) 623 K, where dotted-circles 'a' and 'b' denote the instances corresponding to (a) and (b) above.

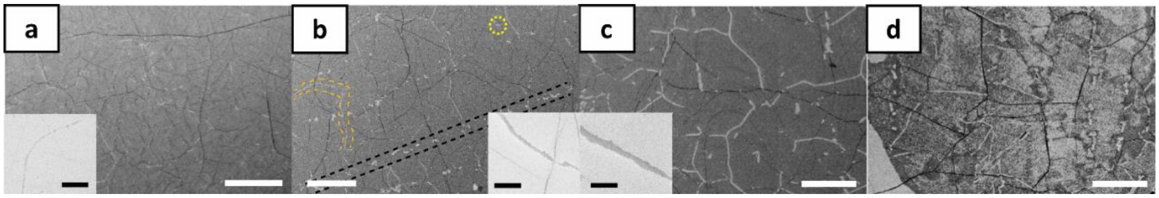

Figure 3.6: Evolution of etching of monolayer CVD-graphene on SiO_2/Si: (a), (b), (c) and (d) represent 15, 30, 45 and 60 minute etch periods in humid air (15,000 ppm H_2O) at 673 K (white scalebars = 10 µm and black scalebars =1 µm). Contrast of the etched grain boundaries is reversed in the insets due to charging and deposition of carbon on the SiO_2 substrate which is commonly observed during high magnification imaging in the scanning electron microscope. (b) also shows the first visually obvious signatures of etching at (i) grain boundaries in the graphene (orange dashed lines), (ii) linear striations in the graphene (black dashed lines), which are spatially commensurate with rough, linear striations in the Cu foil, and (iii) random spots (yellow encircled feature) in the graphene grain interiors presumably from point/other surface defects that are present in the as-grown graphene.

3.2.3. Temperature dependence of the grain boundary etch rate

We next use time-resolved scanning electron microscopy (SEM) to quantify and image the gasification process at the grain edges. A single layer of CVD-grown graphene is transferred to SiO_2/Si and split into several smaller pieces. The samples are maintained at a constant temperature (673 K) in humid air (water vapor = 15,000 ppm) in the open-lid Raman chamber and removed at intervals of 15 minutes and then imaged in the SEM as shown in Fig. 3.6. The first visually obvious signatures of etching are at (i) grain-boundaries in the graphene (orange dashed lines), (ii) linear striations in the graphene (black dashed lines), which are spatially commensurate with rough, linear striations in the Cu foil growth substrate that arise from its manufacture, and (iii) random spots (yellow encircled feature) in the graphene grain interiors presumably from point/other surface defects that are present in the as-grown graphene. With time (Fig. 3.6) these etch pits and lines grow wider. Our observations are consistent with previous experimental and theoretical studies where it has been shown that graphitic materials selectively etch or oxidize at intrinsic and induced defects.[57, 136-138] The dark lines in Fig. 3.6 are wrinkles or folds in the graphene layer which originate from a mismatch between the thermal expansion coefficient of the atomic membrane and the Cu substrate.[139] It can be noted that these folds etch relatively slowly and are more stable (Fig 3.6a-d), presumably because they are elevated off of the SiO_2 substrate.[89] It is important to note that the scale of these wrinkles and folds is much larger than the atomic-scale deformation induced by water-mediated interactions with the substrate. While the latter deformation occurs over a few lattice constants of graphene leading to an increased reactivity, the former deformation via wrinkling and folding occurs over a much longer length scale and elevates the graphene off of the substrate thereby increasing its oxidative stability.

We capture electron micrographs as a function of time and temperature and calculate the average etch-width of the grain boundaries over a cumulative-length of > 200 μm using an image analysis algorithm. From these data, we are able to calculate the etch rate at a grain boundary edge at given temperature and also the temperature dependence of this rate and the activation energy. The histograms in Figs. 3.7a-c show the frequency distribution of the grain boundary widths after 240, 105, and 45 minutes of etching at 573, 623, and 673 K, respectively. From the mode of these distributions fit to log-normal distributions, we find that the grain edges etch with a mode velocity of $3.6x10^{-3}$, $2.3x10^{-2}$, and $1.1x10^{-1}$ nm s^{-1} at 573, 623, and 673 K, respectively. The temperature dependence of the mode velocity can be represented by $v = v_{673}\exp[(-E_A/k_B)(1/T - 1/673)]$ with v_{673} = (1.08 ± 0.02) x 10^{-1} nm s^{-1} and E_A = 1.14 ± 0.10 eV. Several previous studies have investigated the analogous gasification of graphite from crystal edges, reporting large variation in the measured E_A from 0.7 to 2.0 eV.[119, 133, 140-142] However, differences in the experimental O_2 and H_2O concentrations and the temperature range between our study and these past studies of graphite make direct comparison difficult. Whereas the E_A of 0.63 ± 0.05 eV measured in Section 3.2.1 quantifies the activation energy for the oxidation (Fig. 3.1i) of the grain interiors, the E_A of 1.14 ± 0.10 eV measured in this section quantifies the activation energy for the gasification of the grain edges (Fig. 3.1iv).

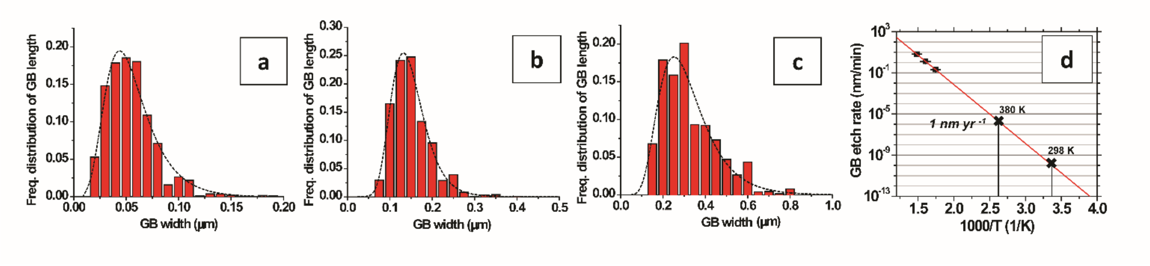

Figure 3.7: Temperature dependence of grain boundary etch rate: (a), (b), and (c) represent the frequency distribution of the grain boundary widths after 240, 105, and 45 minutes of etching at 573, 623, and 673

K, respectively, fit to a log-normal curve. The fits from (a), (b) and (c) are used to determine the etch rates at the respective temperatures and (d) depicts the Arrhenius dependence of these rates with temperature. (E_A = 1.14 ± 0.10 eV).

Sections 3.2.1-3.2.3, combined, allow us to paint a more detailed picture of the degradation of graphene monolayers, which occurs via a two-step process: oxidation followed by gasification as CO or CO_2. Our data show that the barrier for the oxidation of pristine grain interiors (Fig. 3.1i) is lowered to 0.63 ± 0.05 eV in humid air on SiO_2 substrates. Theory has also shown that pre-existing point (e.g. vacancy) and graphene edges (Fig. 3.1iii) will oxidize in air in a barrierless process.[119] Thus, pre-existing defects and the pristine grain interiors will oxidize, with either no barrier or a small 0.63 eV barrier, respectively, relatively rapidly even at modest temperature. It is thought that adsorbed oxygen molecules will dissociate to form oxygen based stationary functional groups like –C=O,-C-O, -O-C=O etc. and sometimes mobile/floating functional groups like C-O-C.[121-123, 143-145] The gasification of oxidized carbon atoms can next occur in the form of CO or CO_2 gas through several probable reaction pathways depending on the stationary functional group of the carbon atom and its proximity to mobile functional groups.[119, 121-123, 143, 146] Gasification leads to widening/etching of the grain edges and boundaries (Fig 3.1iv), as seen previously in the SEM images (Fig. 3.6), with an E_A of 1.14 ± 0.10 eV. The Raman I_D/I_G data indicate the density of oxidized carbon atoms increases with time within the grain interiors; however, our measurements do not directly tell us the activation energy for the gasification (Fig. 3.1ii) of these oxidized carbon atoms. With this said, gasification from within the grain interiors will eventually lead to the formation of small etch pits, and gasification from the edges of these etch pits will also be dictated by an E_A of 1.14 ± 0.10 eV.

It is likely that the barrier to the oxidation of pristine grain interiors is lowered in humid air on SiO_2 substrates because the roughness of the SiO_2 substrate introduces local deviations in the sp^2 structure (as observed in previous AFM studies)[115, 117] and because of charge inhomogeneity[117, 128] on the SiO_2 substrate. This hypothesis can be further verified qualitatively from bilayer experiment in Figure 3.3c, where the topmost graphene layer is isolated from the substrate, resulting in a significantly slower degradation. The lower activation energy calculated for the interior oxidation (Fig. 3.3) compared to the one calculated for grain boundary etching (Fig. 3.7) indicates that the build-up of defects is faster (Fig. 3.1i) than removal of carbon atoms via gasification (Fig. 3.1iv), which is why the graphene grains appear to disappear from the inside out in Fig. 3.6d.

3.2.4 In situ temperature-dependent field-effect transport measurements

Finally, in order to assess the effects of degradation on the electronic properties of graphene on SiO_2, we use field effect transistor measurements to quantify both the doping concentration and charge carrier mobility of single layers of CVD-grown graphene *in situ* during degradation between 473 K and 673 K in humid air (water vapor = 15,000 ppm). Prior to annealing, the CVD-grown graphene is p-type doped with a carrier concentration of $2.4 \, x \, 10^{13}$ cm^{-2} and a field-effect mobility, μ, of 500 $cm^2V^{-1}s^{-1}$, at room temperature. The carrier concentration is determined by extrapolating the linear portion of the source-drain current versus gate bias transfer curve to zero-current to determine the charge neutrality gate bias, and μ is determined from the transconductance, using a standard parallel-plate capacitor model. These fit parameters are typical of graphene grown by CVD on Cu and transferred to SiO_2/Si using similar conditions.[13, 102, 131, 147]

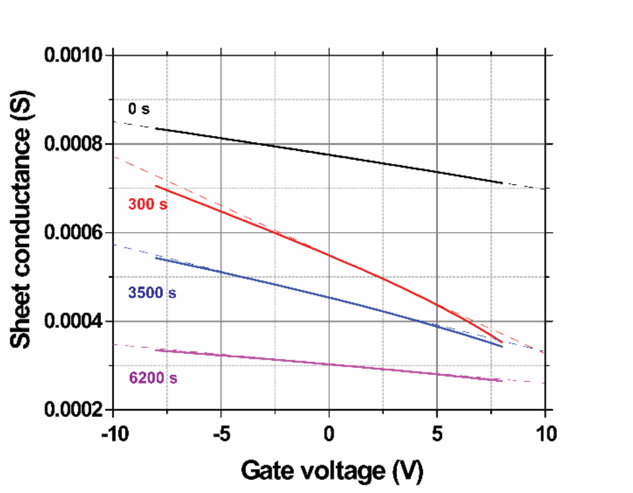

Figure 3.8: Sheet conductance vs gate voltage characteristics of monolayer graphene on SiO_2 at 523 K vs. time. Top to bottom represents the transconductance characteristics at (i) *t* = 0 s (black), (ii) 300 s (red), (iii) 3500 s (blue) and (iv) 6200 s (pink)

Figure 3.8 shows the evolution of the transconductance characteristics of monolayer graphene on SiO_2 at 523 K in ambient with time. The mobility, determined from the slope of the curve, increases rapidly to a maximum value and then starts decreasing back again with time. During the very beginning stages of annealing, the doping concentration rapidly decreases while μ increases as shown for 523 K in Fig. 3.9a and b, respectively. These changes can be attributed to the desorption of surface contaminants, which act as charge transfer dopants and charge scattering sites. Following this desorption, the graphene begins to degrade leading to a doping concentration that increases approximately linearly and μ that decreases with time. Our hypothesis is that μ decays mostly due to interior grain oxidation (Fig. 3.1i), which is based on the observation that the grains oxidize most rapidly from the interior (Section 3.2.2) and the activation energy for this degradation (Section 3.2.1) is lower than that of grain boundary gasification (Section 3.2.3). Previous experiments have shown that the mobility of exfoliated monolayer graphene decays inversely with point defect density.[66, 129] Accordingly, we fit our μ decay data to the following form $\mu^{-1} = \mu_0{}^{-1} + \lambda(t - t_o)$, where μ_0 is the mobility prior to degradation, t_o is the time at which the degradation begins, and λ is the decay constant, which will be proportional to the point defect generation rate (Fig. 3.9b). λ is computed by calculating the slope of the μ^{-1} vs. annealing time plot (Fig. 3.9b) at μ = 500 cm^{2}Vs^{-1}, which is around the center of the range where μ exhibits an almost linear behavior. The fit decay constant λ increases with temperature as shown in Fig. 3.9c, varying as $\lambda = \lambda_{673}\exp[(-E_A/k_B)(1/T - 1/673)]$ with temperature where λ_{673} = (1.1 ± 0.3) x 10^{-5} cm^{-2}V and E_A = 0.66 ± 0.08 eV (Fig. 3.9c). The mobility dependent decay time can be defined as $\tau(\mu) = 1/(\lambda\mu)$. In particular, at 523 K, the mobility dependent decay time at μ = 500 cm^{2}Vs^{-1} is τ = 3.6k s. It can be noted that the μ^{-1} does not have an exact linear dependence with time. The non-linearity can be attributed to other mechanisms, for example the opening of grain boundaries.

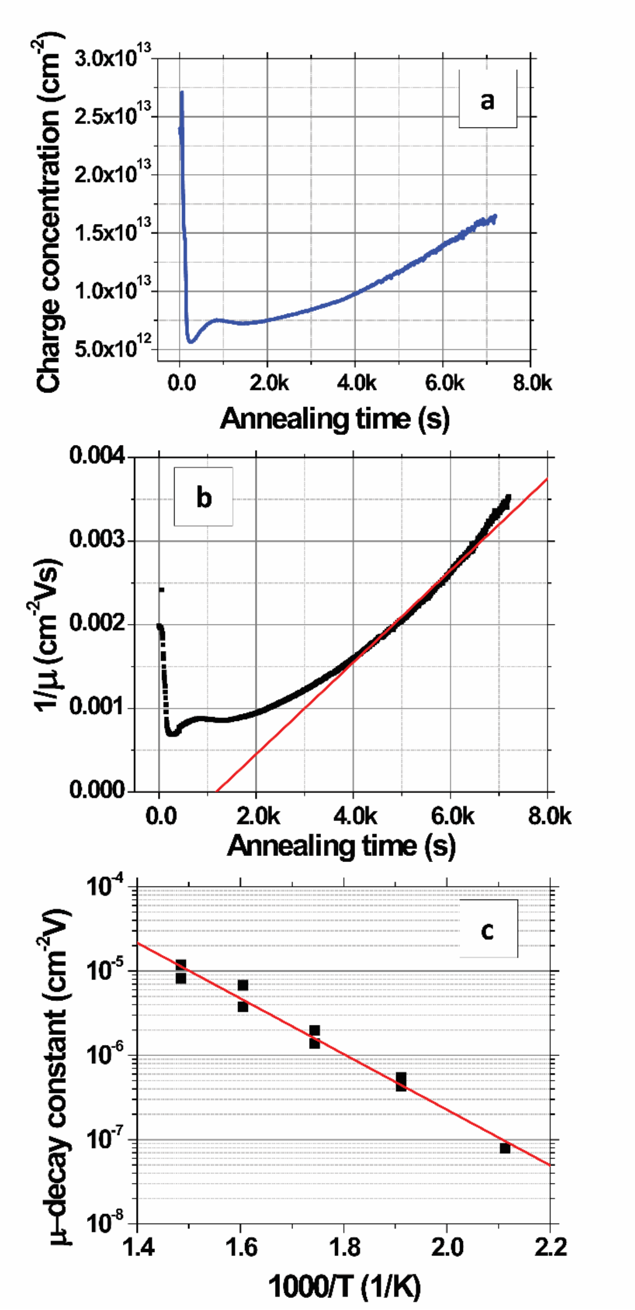

Figure 3.9: Effect of degradation on transport properties of graphene: (a) and (b) represent the evolution of charge concentration and carrier mobility, respectively, with time at 523 K for the CVD-graphene based FET devices on SiO_2/Si. Mobility vs. time plots for different temperatures are independently fit to compute the decay constants for each temperature. (c) Depicts the Arrhenius

dependence of the decay constant, λ, determined from the exponential decay with temperature, where $\lambda = \lambda_{673}\exp[(-E_A/k_B)(1/T - 1/673)]$ and where λ_{673} = (1.1 ± 0.3) x 10^{-5} $cm^{-2}V$ and E_A = 0.66 ± 0.08 eV.

3.3 Implications and conclusions

Successful integration and support of monolayer graphene on substrates, especially oxides, is an integral part of realizing electronic and optoelectronic devices with the atomic membrane. We find that the grain interiors of monolayer graphene oxidize at a rate $(\partial/\partial t)(I_D/I_G) = R_{673}\exp[(-E_A/k_B)(1/T - 1/673)]$. In humid ambient air (15,000 ppm H_2O), CVD-graphene has a R_{673} = (3.7 ± 0.7) *x* 10^{-4} s^{-1} and an E_A = 0.63 ± 0.05 eV, whereas in dry air R_{673} = (3.6 ± 0.4) *x* 10^{-5} s^{-1} and E_A = 1.85 ± 0.17 eV. Mechanically exfoliated monolayer graphene oxidizes with similar kinetics as CVD-grown monolayer graphene. The degradation is immeasurable for exfoliated multilayers in ambient and for CVD-monolayers in nitrogen. Etching at the grain boundaries for monolayers proceeds with a mode velocity $v = v_{673}\exp[(-E_A/k_B)\{(1/T) - (1/673)\}]$ with v_{673} = (1.08 ± 0.02) *x* 10^{-1} nm s^{-1} and E_A = 1.14 ± 0.10 eV. At a given temperature, the charge carrier mobility decay rate is given by $\mu^{-1} = \mu_0{}^{-1} + \lambda(t - t_o)$, and the decay constant varies as $\lambda = \lambda_{673}\exp[(-E_A/k_B)(1/T - 1/673)]$ where λ_{673} = (1.1 ± 0.3) x 10^{-5} $cm^{-2}V$ and E_A = 0.66 ± 0.08 eV.

These measurements are useful for two important reasons. Firstly, these measurements can be used to quantitatively predict the oxidative stability of monolayer graphene on SiO_2 under different conditions. For example, at 298 K in humid (15,000 ppm H_2O) ambient, $(\partial/\partial t)(I_D/I_G)$, v, and τ(500 $cm^2V^{-1}s^{-1}$)can be extrapolated to 4.5 x 10^{-10} s^{-1}, 7.3 x 10^{-5} nm yr^{-1} and 8.4 yr, respectively. Thus, the mobility of graphene exposed to humid ambient on SiO_2 is expected to be stable at room temperature for only a duration of several years. At an elevated temperature of 380 K the same parameters become 4.49 x 10^{-8} s^{-1}, 1 nm yr^{-1}, and 12.4 days, respectively. At this condition, mobility decay is much faster and the grain boundaries will etch leaving discontinuous graphene after roughly one year.

Secondly, these data are useful as they clearly show how graphene's stability on SiO_2 can be increased. Most importantly, graphene's stability on SiO_2 in ambient can be improved by limiting its exposure to water vapor. Furthermore, degradation at grain boundaries or striations can be reduced by growing graphene with larger grains and using high quality, flatter metal catalyst substrates, respectively. Ultimately, this study is expected to serve as a foundation for overcoming the limitations posed by ambient on graphene and help engineer graphene materials with superior properties for demanding applications.

3.4 Experimental details

A. CVD-graphene growth

Monolayers of graphene were grown on Cu foils (Alfa Aesar product# 13382, lot# B03Y027) as the growth catalyst. The foils were pre-cleaned with acetic acid (Fisher) for 15 minutes to remove contaminants and native oxides then rinsed in DI water (x3) before being dried with an air-gun. The cleaned Cu foils were then annealed for 30 minutes at 1030 °C in 95% argon + 5% hydrogen (340 sccm flowrate) to remove trace surface contaminants and also to reduce the surface roughness of the foil before initiating the growth process. The growth was conducted at 1030 °C with 95% argon + 5% methane (0.300 sccm) and 95% argon + 5% hydrogen (340 sccm) for 3 hours. The manufactured graphene on Cu foils were stored in a N_2 glovebox to prevent the oxidation of the graphene and the copper surfaces. All the graphene monolayers used for the experiments were manufactured from the same batch for consistency and the initial I_D/I_G varied as 0.06 ± 0.025 for the entire batch used for this study

B. Transfer of CVD-graphene on to SiO_2/Si and mechanical exfoliation of graphene

Graphene monolayers grown via CVD were transferred on to Si substrates with an 89 nm thick thermally-grown SiO_2 layer. The transfer was completed using a commonly employed sacrificial polymer (PMMA – poly methyl methacrylate) method, similar to previously reported.[53, 91] CVD-graphene on copper was over-coated with PMMA (M.W. = 950k, 2% in chlorobenzene) by spin-coating at 2000 rpm. The samples were placed in copper etchant ammonium persulfate (25% Transene company, Inc. APS-100 + 75% DI water) and then bath-ultrasonicated for 15 minutes to remove the bottom-facing graphene layer. The samples were left overnight (~10 hr) in the etchant for the copper to completely etch. Post-etch, the floating PMMA on graphene was scooped out from the APS solution and re-floated in DI water (*x*3) to rinse any residual copper etchant. The samples were then dispersed in 5% HF in DI water for 60 minutes to remove trace silica particles that might have deposited from the CVD system during the growth, following which they were rinsed in DI water (*x*3). From the final DI water bath, the samples were scooped on to SiO_2/Si and spin-dried at 8000 rpm for 2 minutes to remove water trapped between the graphene sheet and the substrate. To remove the PMMA layer, the samples were placed in room-temperature acetone baths (*x*2) for 20 minutes after which they were rinsed in isopropanol for 2 minutes to wash away any residual acetone. Finally, they were dried using an air-gun before being cut into several pieces for further analysis.

Mechanical exfoliation of monolayer graphene on SiO_2 was done from small flakes of HOPG using the scotch-tape method that has been previous used in several other studies, and they were identified on the substrate using optical microscopy and further confirmed via Raman spectroscopy.[148, 149] The thickness of the silicon dioxide, 89 nm, used in the experiments creates enough contrast between the graphene and the substrate to make the graphene visible under white light in an optical microscope. In particular, the lowest contrast features indicate the presence of a single graphene layer and addition of subsequent layers increases this contrast and makes it appear darker, progressively. In the Raman spectra for an intrinsically doped monolayer graphene on SiO_2/Si, (i) the 2D-band to G-band ratio is always >1 under a 532 nm excitation wavelength and (ii) the 2D peak can be fit to a single Lorentzian function. For a bi-layer graphene the 2D to G band ratio is <1 and the 2D peak can be fit two Lorentzian functions.[71, 74]

C. Characterization and analysis techniques

(i) In-situ Raman spectroscopy: Labram Aramis by Horiba was used for the *in situ* Raman studies. An enclosed heating stage (Linkam THMS 600) was integrated with an automated X-Y stage to control the temperature of the sample and atmosphere around it. A 532 nm laser with power = 1 mW power and exposure time = 1 second/spot were used for all the scans to avoid substrate heating effects. Maps were collected across a fixed 100 μm *x* 100 μm region (with a pixel size of 10 μm *x* 10 μm) at intervals of 150 seconds during the annealing period. A temperature controller was used to control the initial ramp-rate (100 K min^{-1}) and final hold-temperature of the stage. Gas inlets in Linkam THMS 600 were used to pump or purge the sample chamber to control the

atmosphere. The heating rate used for all the measurements was 100 °C/min and the measurements of relative humidity and Raman spectra were initiated after the stage had reached the set annealing temperature.

(ii) Imaging Raman spectroscopy: MicroRaman DXR by Thermofisher was used for all the spatially-resolved Raman imaging studies. A 532 nm laser with power = 1 mW power and exposure time = 3 second / spot were used for all the scans to avoid substrate heating effects. The laser spot size was focused to ~700 nm, and a mapping pixel size of 200 nm x 200 nm was used.

(iii) Scanning electron microscopy: SEM LEO 1530 was used to image the graphene on SiO_2/Si samples. The electron gun energy used was 3 keV.

(iv) Image analysis: The scanning electron micrographs were analyzed via an image analysis algorithm developed using MATLAB to compute the average grain boundary width.

(v) Charge carrier mobility measurements: Graphene based field-effect transistors were made with 89 nm SiO_2 as the gate dielectric on a Si gate. 75 nm of Au was thermally evaporated through a shadow mask to form the source and drain contacts. The channel width and length were 5 mm and 1 mm, respectively. The temperature was controlled using Linkam THMS 600 during the measurements. The heating rate used for all the measurements was 100 °C/min and the transconductance measurements were initiated after the stage had reached the set annealing temperature.

Acknowledgements: The majority of the experimental Raman spectroscopy and electron microscopy work was supported by the National Science Foundation (Grant number CBET-1033346). The experimental Raman spectroscopy and electron microscopy were partially supported by Wisconsin Energy Institute. The *in situ* charge transport measurements were supported by the DOE Office of Science Early Career Research Program (Grant number DE-SC0006414) through the Office of Basic Energy Sciences. The grain boundary etching analysis was supported by the University of Wisconsin-Madison, Center of Excellence for Materials Research and Innovation (National Science Foundation Grant number DMR-1121288). MSA also acknowledges partial support from a 3M Non-Tenured Faculty Grant. The authors gratefully acknowledge use of facilities and instrumentation supported by the NSF-funded University of Wisconsin Materials Research Science and Engineering Center (DMR-1121288).

4. Intrinsic pinholes in graphene grown via chemical vapor deposition

*Susmit Singha Roy, Robert M. Jacobberger, Chenghao Wan, Michael S. Arnold**

Department of Materials Science and Engineering, University of Wisconsin-Madison

SS synthesized graphene, characterized defects via scanning electron microscopy and Raman spectroscopy and analyzed the results. RMJ developed recipes for synthesis of graphene on Cu (111), helped in understanding the data and partially contributed to the surface roughness measurements. CW performed majority of the surface roughness measurements and partially contributed to understanding the data.

Abstract

Presence of defects in the form of pinholes and edges can fatally affect graphene's properties and its ability to perform in numerous applications. It is demonstrated that graphene, synthesized via chemical vapor deposition on scalable copper substrates, that appears complete in scanning electron microscopy, consists of high density of regions where the growth is still incomplete. On copper foils, typically used in scalable applications of graphene, the intrinsic pinholes or nanopores primarily coincide with the regions of high surface roughness on the growth substrate. The surface roughness of the copper foil and in-turn the nanopore density in the graphene membrane can by regulating the pre-growth annealing temperature and time. Nanopore density is reduced by a factor of 42 when pre-growth conditions are changed from 1223 K / 0.5 h to 1323 K / 16 h. On atomistically flat epitaxial Cu (111) growth substrate, the nanopore density is 200x less under the exact same conditions compared to the copper foil. The degree of completion of growth on the Cu (111) is further enhanced by increasing the duration of growth and is limited by presence of surface irregularities in the form of impurities or surface roughness. This study is expected to serve as a foundation for engineering graphene membranes of superior quality with ultra-low density of intrinsic nanopores for demanding applications.

4.1 Introduction

Despite its atomic thickness of ~ 3.4 Å, monolayer graphene is impermeable to species as small as helium.[35] Graphene also has high thermal stability, mechanical strength, optical transparency, and chemical inertness.[14, 16, 17, 20, 26, 27, 31, 34, 76, 78, 79] Consequently, graphene is a promising candidate material for diffusion barriers in applications such as corrosion prevention and device encapsulation.[70, 82, 85, 94] Moreover, fabricating nanopores with tailored size, density, and functionalization into the graphene lattice can improve the efficiency and functionality of gas separation and water desalination. For example, theoretical calculations performed by Cohen-Tanugi *et al.* and Jiang *et al.*[5, 90] revealed that graphene films with precisely engineered nanopores can outperform state-of-the-art membranes in gas-phase and liquid-phase separation, increasing the permeability and selectivity by orders of magnitude. While these studies have provided proof-of-principle demonstrations of graphene's ability to outperform existing technology, scalable graphene synthesis techniques are required to develop commercial products.

Chemical vapor deposition is among the most promising methods to produce graphene on an industrial scale because of its ability to yield continuous sheets over large areas on relatively inexpensive catalysts, such as copper.[33, 45, 47, 51, 78, 80, 93, 147, 150] However, graphene samples made using CVD contain a variety of point and line defects, such as vacancies, impurities, and grain boundaries. Presence of defects in general of any form can fatally affect graphene's mechanical, electronic and barrier properties and its ability to perform in numerous applications.[46, 70, 88, 91, 151] In particular, these types holes or edges in the atomic membrane can drastically affect its ability to perform as a barrier by providing spurious pathways for species diffusion and inhibiting graphene's use as a diffusion barrier.[70, 101]

Consequently, attempts to use graphene synthesized via CVD for diffusion barrier applications have greatly underperformed compared to the benchmarks set by the theoretical and non-scalable counterparts. For example, O'Hern *et al*. showed that graphene monolayers that look visually-complete with scanning electron microscopy can still have a high density of intrinsic nanopores of diameters ranging between 1 and 10 nm.[23] These pores are sufficiently large to allow permeation of oxygen and water through the membrane. The presence of these random holes or regions of incomplete growth in the membrane with such high density drastically hinders its performance as a corrosion barrier by providing numerous barrierless pathways for oxygen and water diffusion. In addition, these defects and incomplete growth areas also limit its performance for filtration, where it is critical to have pores of a particular diameter that are rationally incorporated and distributed in a controlled fashion over the entire membrane. Hence, in order to develop high performance barriers and filters using graphene membranes, it is crucial to understand the origin of the nanopores and develop methods to reduce or eliminate the nanopores.

In this work, we investigate the origin of these intrinsic nanopores and engineer methods to control their density and to produce high-quality graphene films with ultra-low pore density. The completeness of graphene layers grown on Cu catalysts via CVD is characterized. These monolayer graphene films cover nearly 100 % of the Cu surface, except for sub-10 nm point-like holes or pores. On commercially-available Cu foils, the degree of completion of graphene monolayer growth is limited by surface roughness. The majority of the nanopores in the monolayer graphene coincide with regions of high roughness, which are primarily periodic parallel striations introduced during production. The Cu foil surface roughness can be reduced by increasing the pre-growth annealing temperature and time, resulting in a decrease in the nanopore density of over two orders of magnitude. On smooth epitaxial Cu thin films, the degree of completeness of growth is significantly improved compared to the rough foils and is no longer limited by surface roughness. The degree of completeness on the epitaxial Cu (111) is found to be enhanced even further by increasing the growth duration which is hypothesized to reduce the trace surface irregularities originating from contaminants and surface roughness. We believe this study will serve as a foundation for (i) developing better scalable growth substrates for CVD graphene, (ii) synthesizing graphene with ultra-low nanopore density and (iii) engineering high performance samples for diffusion barriers, filters, and electronics.

4.2 Results and Discussion

We explore the effects of surface roughness, annealing temperature, and annealing time on the degree of completion in monolayer graphene films grown via CVD. The graphene films are synthesized on Cu foils and on epitaxial Cu (111) thin films at atmospheric pressure as described in the supporting information. Large regions with incomplete graphene growth can typically be identified by contrast differences in scanning electron microscopy (SEM) imaging or by an increase in the D:G ratio in Raman spectroscopy.[55] The graphene films studied here cover nearly 100 % of the Cu surface, except for sub-10 nm point-like defects. Thus, these films are referred to as visually-complete graphene monolayers (VCMG). However, sub-10 nm defects and holes are below the spatial resolution of these techniques. Such small regions with incomplete growth have been studied with scanning tunneling microscopy and transmission electron microscopy.[23] However, these techniques have low throughput and it is difficult to gain ensemble information over large areas. Therefore, in order to visualize and quantify the intrinsic nanopores in the VCMG, we adapt a procedure introduced by O’Hern *et al.* in which Cu etchant diffuses through regions of incomplete growth or defective graphene regions, referred as intrinsic nanopores, resulting in the formation of etch pits that are localized underneath the nanopores.[23] The Cu etchant cannot diffuse through regions containing pristine graphene, and the underlying Cu does not form etch pits. In our procedure, the monolayer graphene films grown on Cu are immersed into a dilute Cu etchant (0.08 mM $FeCl_3$ + 0.08 mM HCl), rinsed in deionized water, and dried with air. These etch pits grow wider and deeper with time. After etching for 10 minutes, the etch pits are easily visualized with SEM and, consequently, the density of the nanopores can be easily quantified.

4.2.1 Surface-roughness limited regime

First, the completeness of coverage is investigated on monolayer graphene films synthesized on commercially-available Cu foils, which are the most commonly used substrates for graphene growth. Fig. 4.1a shows an SEM image of a representative VCMG synthesized at 1323 K for 2 h and 0.500 sccm of CH_4. The darker lines in Fig. 4.1a are wrinkles and folds in the monolayer graphene, which originate from thermal expansion mismatch between graphene and Cu. Using SEM imaging, the graphene layer looks complete without any holes. In addition, the spatially-resolved Raman spectrum of the VCMG has a low ratio of the Raman D band to the Raman G band of 0.03 (Fig. 4.1b), indicating a low defect density. However, after exposing the sample to the etching solution, etch pits can be easily visualized with SEM, as shown in Fig. 4.1c. Unlike Fig. 4.1a, Fig. 4.1c is imaged using the secondary electron detector of the SEM, which gives a better depth perception over surface contrast. This indicates that even though the graphene layer appears to be complete with a low defect-density at the resolution of the SEM and the Raman, it actually consists of a high number of regions where the growth of the monolayer is incomplete or highly defective.

These regions of high nanopore density primarily coincide with the rough elevated parallel striations of the as-manufactured Cu foil as seen in Fig. 4.1d. This indicates that graphene is unable to grow over these rough features present on the Cu foil, resulting in the formation of holes. The nanopore density on then smoother regions of the Cu foil are significantly reduced compared to these striations. These nanopores are primarily situated in the regions of high roughness on the Cu foil and do not coincide with the grain boundaries of the graphene as discussed later in section 2.2.

The morphology of the growth substrate is modified by varying the pre-growth annealing conditions in a flow of 95% Ar and 5% H_2 to study the effect of surface roughness on growth completion. The topography of the Cu foils after growth is characterized optical interferometry, as shown in Supporting Information Fig. B.S2. Before growth, these surfaces have an as-manufactured surface roughness of ~ 500 nm. When the pre-growth annealing time is 0.5 h, the surface roughness at 1223 K, 1273 K and 1323 K is 246 ± 12 nm, 225 ± 12 nm and 204 ± 15 nm (Fig. 4.2), respectively, indicating that the surface of the foil becomes smoother as the pre-anneal temperature increases. With 0.5 h annealing time, the nanopore density is significantly reduced when the annealing temperature is varied from 1223 K to 1323 K, Fig. 4.3a-c. The nanopore density at 0.5 h anneal reduces from $1.27 \pm 0.04\ \mu m^{-2}$ to $(8.82 \pm 0.12) \times 10^{-1}\ \mu m^{-2}$ when temperature is increased from 1223 K to 1323 K (Fig. 4.4).

The decrease in roughness with temperature becomes larger when the pre-growth annealing time is increased to 16 h. The roughness for 1223 K, 1273 K and 1323 K is 231 ± 11 nm, 189 ± 12 nm and 143 ± 11 nm, respectively. Using the same pre-growth annealing temperature reduces the roughness for longer annealing times. For example, at 1323 K, the roughness is reduced to 143 ± 11 nm from 204 ± 15 nm when the pre-growth annealing time is increased from 0.5 h to 16 h. Similar to the 0.5 h anneal, with the 16 h anneal, the nanopore density is significantly reduced when the annealing temperature is varied from 1223 K to 1323 K, Fig. 4.3d-f. The nanopore density at 16 h anneal reduces from $(4.84 \pm 0.09) \times 10^{-1}$ µm^{-2} to $(3.00 \pm 0.05) \times 10^{-2}$ µm^{-2} when temperature is increased from 1223 K to 1323 K (Fig. 4.4).

The trends in the nanopore density correlate with those observed for the surface roughness (Fig. 4.2), confirming that the surface morphology of the growth substrate plays a crucial role in determining the degree of completeness of the graphene layer. Overall, a reduction of 42 times is achieved when the pre-growth annealing conditions are modified from 1223 K / 0.5 h to 1323 K / 16 h. However, even though the density of rough areas in the Cu foils are reduced significantly by altering the pre-growth annealing conditions, it is difficult to eliminate these regions completely. Hence, to explore the growth completeness of the VCMG in a regime where the growth is not limited by the surface roughness of the substrate, the surface must be atomically flat.

4.2.2 Beyond surface-roughness limited regime

In order to further reduce the surface roughness of the substrate, smooth epitaxial Cu(111) thin films are used to catalyze growth instead of the rough polycrystalline Cu foils. Cu(111) thin films 500 nm in thickness are sputtered on c-plane sapphire. The resulting Cu(111) surface roughness is ~1 nm across a 10 µm x 10 µm area, as measured by Jacobberger *et al.*[152] VCMG was synthesized simultaneously on Cu foils and Cu(111) thin films under the same growth conditions as were used in Fig. 4.3c to compare the intrinsic nanopore density. The nanopore density is reduced by a factor of ~200 on the Cu(111) thin films $(4.61 \pm 0.56) \times 10^{-3}$ µm^{-2} compared to the Cu foils $(8.82 \pm 0.12) \times 10^{-1}$ µm^{-2} (Fig. 4.5a-b).

The duration of the growth was varied while the other parameters were set similar to that in Fig. 4.5 to further investigate the degree of completeness. Previous studies have suggested that the growth rates of graphene is greatly reduced once it is nears completion.[49, 50, 54] As the growth time increases from 0.25 h to 2 h, the nanopore density in the VCMG reduces exponentially. The nanopore density saturates after 1.5 h (Fig. 4.6a-d). The density of the holes reduces from (2.93 ± 0.30) x 10^{-2} μm^{-2} for the 0.25 h growth to (4.61 ± 0.56) x 10^{-3} μm^{-2} for the 2 h growth (Fig. 4.6d). These results show that the completion of the VCMG is increased by longer growth times.

Partial graphene growths were conducted to determine if nanopores in the graphene layers originate from un-stitched grain boundaries. Partially grown graphene monolayer with > 70 % coverage was synthesized and tested for nanopores which allowed a direct correlation between the spatial distribution of the grain boundaries and the nanopores. Figure 4.7a shows an unstitched grain boundary, where two growth fronts are about to merge and form a grain boundary. The etch pits align along the intersection of the two fronts. As the grain boundary stitches together, the number of etch pits along the line of intersection is reduced (Fig. 4.7b) and eventually almost disappears (Fig. 4.7c). As the grain-boundaries approach visual-completion, the nanopores start to disappear at the grain boundary lines; however they still exist at random spots in the visually-complete grain interiors, indicating the nanopores do not predominately originate from un-stitched grain boundaries (Fig. 4.7a-c).

It is possible that the incomplete or defective spots are irregularities on the surface of the copper film. These could either be trace contaminants like SiO_2 from the furnace environment or a rough feature intrinsic to the film, both of which have a chance of getting removed during the course of the growth due to the reducing environment and high temperature anneal, respectively. As observed in figure 4.6, these irregularities on the surfaces of the epitaxial thin films are removed to some extent via annealing at increased growth temperature or growth time, suggesting that they could be some surface contaminants that are neutralized during the growth either by the effect of the precursor gases (H_2/CH_4) or by the thermal annealing.

4.3 Conclusion

In order to take advantage of graphene’s extraordinary ability to act as an impenetrable barrier in commercial applications such as corrosion prevention, device encapsulation, water desalination and gas separation, it crucial to achieve atomically-continuous graphene films using scalable synthesis techniques. However, CVD on Cu foils results in a graphene that appears visually-complete, but actually contains a high density of intrinsic holes that hinder their ability to selectively prevent diffusion. These intrinsic nanopores are due to the roughness and morphology of the underlying Cu foil used for growth, such as striations introduced during Cu foil production. Pre-growth annealing can be used to reduce the roughness of the Cu foil surface, resulting in a higher degrees of growth completion. In particular, when pre-growth annealing temperature is increased from 1223 K to 1323 K for a given annealing time of 16 h, the nanopore density in the VCMG reduces from $(4.84 \pm 0.09) \times 10^{-1}$ μm^{-2} to $(3.00 \pm 0.05) \times 10^{-2}$ μm^{-2}. Also, at an annealing temperature of 1323 K, the nanopore density is reduce by a factor of ~30 when the duration of the pre-growth anneal is increased from 0.5 h to 16 h. Therefore, on the commercially available Cu foils that are typically used for synthesis, the degree of completion of monolayer graphene is limited by the surface roughness of the Cu substrate. On smooth epitaxial Cu(111), the nanopore density is reduced by a factor of ~200 using the same conditions when compared to the Cu foil. On the epitaxial films, where the nanopore density is not limited by surface roughness of the growth substrate, the degree of completion of the VCMG can be altered by varying the growth conditions during CVD. For example, the hole density is increased by a factor of ~6 when the growth time is increased from 0.25 h to 2 h for a constant growth temperature of 1323 K. The holes do not coincide with graphene grain boundaries, but instead occur at random locations primarily in the grain interiors. This study is expected to serve as a foundation for (i) developing high quality substrates for scalable graphene synthesis, (ii) synthesizing graphene with ultra-low nanopore density and ultimately (iii) is expected to serve as a foundation for engineering graphene membranes of superior quality for demanding applications.

4.4 Experimental details

A. Graphene growth via CVD

Monolayer graphene was grown on Cu foils (Alfa Aesar product # 13382, lot # B03Y027) and epitaxial Cu(111) thin films. The foils were pre-cleaned with acetic acid (Fisher) for 15 minutes to remove contaminants and the native oxide. The substrates were then rinsed in three deionized water baths before being dried with compressed air. The Cu foils and Cu thin films were then pre-annealed at their respective growth temperature (described in Fig. B.S1) between 1223 K and 1323 K in 95% Ar and 5% H_2 (340 sccm total flowrate) to remove trace surface contaminants and oxides and also to reduce the surface roughness of the foil before growth. 95% Ar and 5% CH_4 (0.500 sccm) was added to the flow to begin the graphene growth. The graphene on Cu was stored in N_2 to prevent oxidation of the graphene and the Cu surfaces. More details of the CVD process are provided in Fig. B.S1 of the supporting information.

B. Characterization and analysis techniques

(i) Raman spectroscopy: MicroRaman DXR by Thermofisher was used to obtain spatially-averaged Raman spectra over a 100 µm x 100 µm area. A 532 nm laser with power of 1 mW and

exposure time of 3 seconds / spot was used for each scan to avoid substrate heating effects. The laser spot size was ~700 nm, and the mapping pixel size was 500 nm x 500.

(ii) Scanning electron microscopy: SEM LEO 1530 was used to image the graphene on Cu samples. The electron energy was 3 keV. The secondary electron detector was used to better visualize the variations in depth along the surface and the in-lens detector was used to better study the contrast between different features on the surface.

(iii) Image analysis: The SEM images were analyzed via ImageJ and via an image analysis algorithm developed using MATLAB to determine the nanopore density.

(iv) Surface roughness: The surface morphology of Cu foils after graphene synthesis was characterized using a Zygo NewView 6K white light interferometer over areas of 180 µm x 130 µm. More details are provided in the supporting information (Fig. B.S2).

Acknowledgements: The majority of the Raman spectroscopy and electron microscopy work was supported by the National Science Foundation (Grant number CBET-1033346). The Raman spectroscopy and electron microscopy were also partially supported by the Wisconsin Energy Institute. DOE Office of Science Early Career Research Program (Grant number DE-SC0006414) through the Office of Basic Energy Sciences. The grain boundary etching analysis was supported by the University of Wisconsin-Madison, Center of Excellence for Materials Research and Innovation (National Science Foundation Grant number DMR-1121288). MSA also acknowledges partial support from a 3M Non-Tenured Faculty Grant. The authors gratefully acknowledge use of facilities and instrumentation supported by the NSF-funded University of Wisconsin Materials Research Science and Engineering Center (DMR-1121288). R.M.J. is supported by the Department of Defense (DOD) Air Force Office of Scientific Research through the National Defense Science and Engineering Graduate Fellowship (No. 32 CFR 168a).

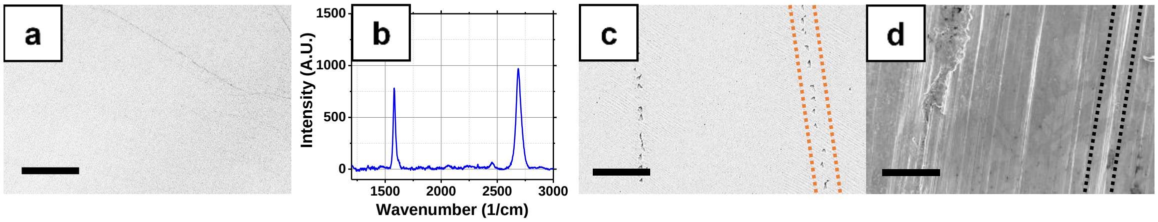

Figure 4.1. Nanopores in visually complete monolayer graphene: (a) A representative image of visually-complete graphene monolayer (VCMG) on copper in SEM synthesized at 1323 K for 2 h and 0.500 sccm of CH_4., darker lines depict wrinkles or folds in the graphene layer. (b) Spatially-averaged Raman spectra of (a) over a 100 µm x 100 µm area. (c) Depicts the SEM image of (a) after exposure to copper etchant - the darker spots indicate etch pits in the copper that coincide with regions of incomplete growth in the graphene monolayer primarily occurring in parallel lines (between orange-dashed lines). (d) SEM image of as-manufactured copper foil showing parallel striations (black-dashed lines) which end up as regions of incomplete growth after CVD. (Scalebars = 10 µm)

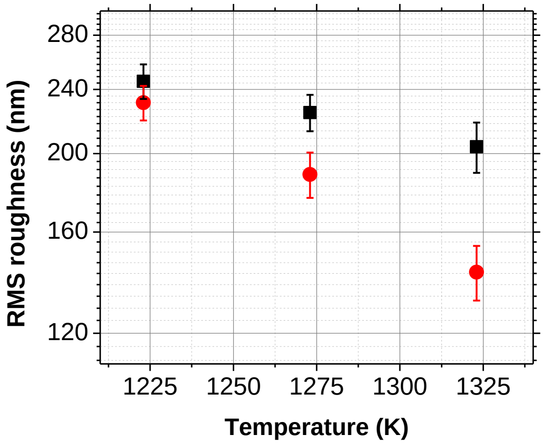

Figure 4.2. Surface roughness variation with pre-growth anneal duration and temperature - 0.5 hour pre-anneal duration (black-squares) yields a spatially averaged (180 µm x 130 µm) rms roughness of 246 ± 12 nm, 225 ± 12 nm and 204 ± 15 nm at 1223 K, 1273 K and 1323 K, respectively. The rms roughness after 16 hour annealing (red-circles) for 1223 K, 1273 K and 1323 K is 231 ± 11 nm, 189 ± 12 nm and 143 ± 11 nm, respectively

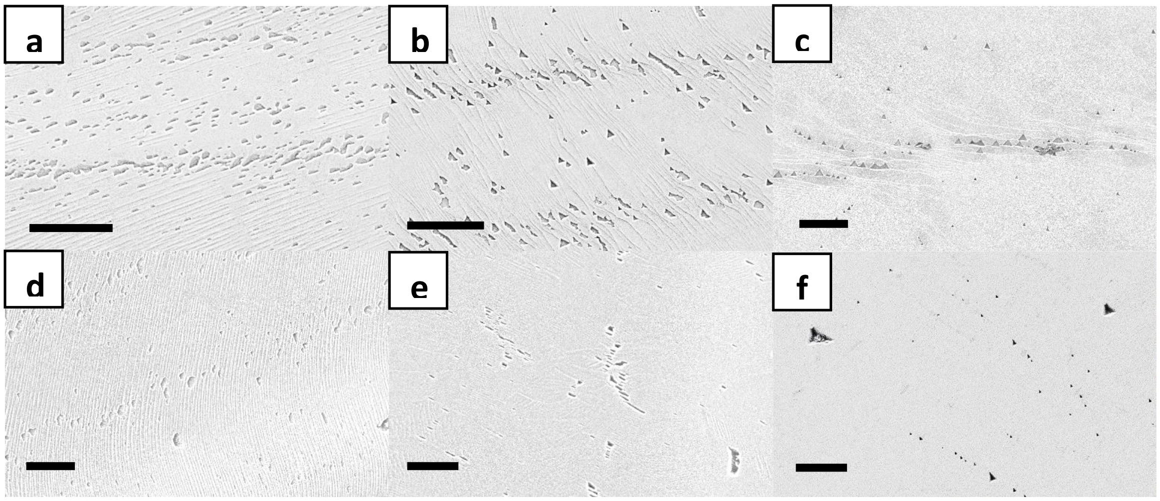

Figure 4.3. Qualitative representation of nanopore density variation in VCMG with repect of pre-growth annealing duration and temperature. Top row: SEM images depicting the nanopores

when pre-growth annealing temperature is (a) 1223 K, (b) 1273 K and (c) 1323 K, respectively at a constant annealing time of 0.5 hours. Bottom row: SEM images depicting the nanopores when pre-growth annealing temperature is (d) 1223 K, (e) 1273 K and (f) 1323 K, respectively at a constant annealing time of 16 hours. (Scalebars = 5 μm)

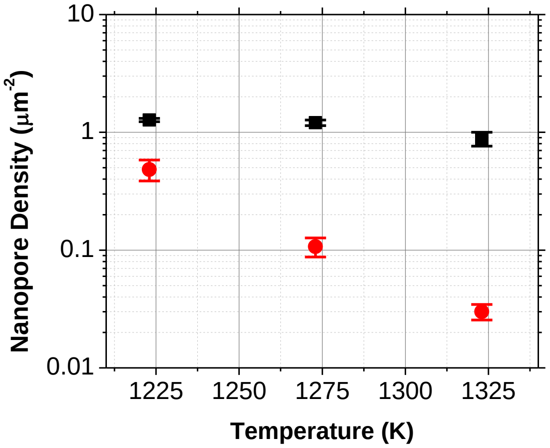

Figure 4.4. Nanopore density variation with pre-growth annealing temperature and duration. At 0.5 h annealing time (black squares) nanopore density from 1.27 ± 0.04 μm^{-2} to (8.82 ± 0.12) x 10^{-1} μm^{-2} when temperature is increased from 1223 K to 1323 K. At 16 h annealing time (red-circles) nanopore density reduces from (4.84 ± 0.09) x 10^{-1} μm^{-2} to (3.00 ± 0.05) x 10^{-2} μm^{-2} when temperature is increased from 1223 K to 1323 K

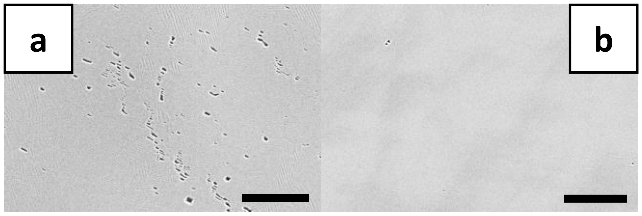

Figure 4.5. Nanopore density compared via SEM between copper foil (a) and epitaxial Cu (111) film (b) synthesized at 1323 K for 2 hours with 0.500 sccm CH_4 flowrate. The nanopore density

56) x 10^{-3} μm mpared to

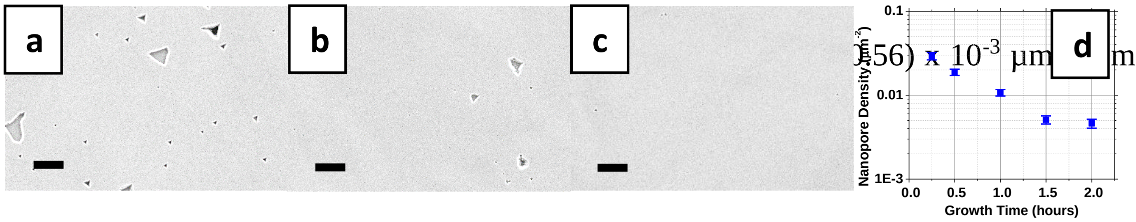

Figure 4.6. Nanopore density variation with growth duration on epitaxial Cu (111) films. (a), (b) and (c) denote SEM images of VCMG grown at 1323 K at 0.500 sccm CH_4 for 0.5 hours, 1 hour and 1.5 hours, respectively, after being exposed to copper etchant to visualize the nanopores . (d) Represents the variation of nanopore density with growth time. The density of the nanopores reduces from (2.93 ± 0.30) x 10^{-2} μm^{-2} for the 0.25 h growth to (4.61 ± 0.56) x 10^{-3} μm^{-2} for the 2 h. (Scalebars = 10 μm)

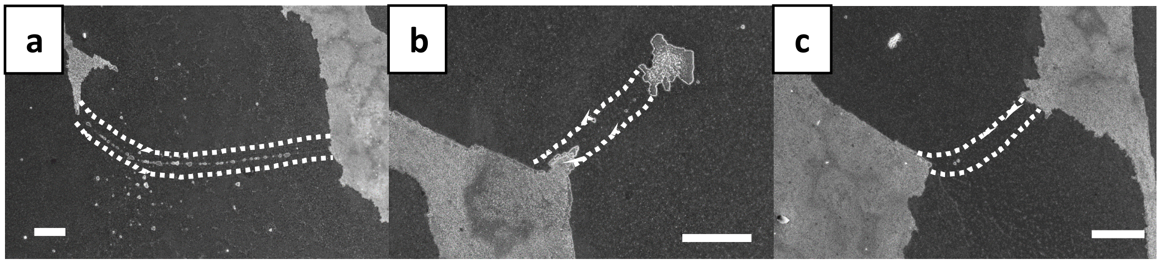

Figure 4.7. Nanopores at grain boundaries via SEM (Growth conditions: 1323 K for 0.25 hours at 0.500 sccm CH_4 flowrate). Dashed lines in (a), (b) and (c) depict the regions when two distinct graphene crystals merge to form a grain boundary. (a) Represents an unstitched grain boundary with a large density of nanopores. (b) and (c) shows the nanopore density across a partially stitched and a fully stitched grain boundary, respectively. Nanopore density in the grain boundary regions of (b) and (c) are significantly lower than (a) indicating that stitched grain boundaries in complete growth rarely contribute to nanopores. (Scalebars = 5 µm)

5. Engineering scalable graphene diffusion barriers

Susmit Singha Roy, Zhaodong Li, Xudong Wang, Michael S. Arnold*

Department of Materials Science and Engineering, University of Wisconsin Madison

SS performed the all the experiments and calculations for this study.

ZL deposited Al_2O_3 for the heterostructured barriers using atomic layer deposition for this study.

Abstract

Experimental studies have established that defect-free non-scalable graphene is an excellent barrier material, however its scalable counterparts are still well behind in terms of performance. The latter’s ability to perform as a corrosion preventing membrane is compromised by the presence of high density of defects, degradation in ambient environment and induced electrochemical corrosion of the underlying metal due the presence of graphene. It is demonstrated here that the electrochemical corrosion can be suppressed by adding an ultra-thin layer of electrical insulator Al_2O_3 between the metal and graphene. The hybrid structure performs 27 times better compared to the graphene on metal control after 24 hours of annealing in humid environment at 473 K. In addition, stacking multiple layers of graphene progressively improves the barrier performance by protecting the underlying graphene layers from deterioration. A four monolayer stack of graphene on Al_2O_3 keeps the underlying metal corrosion-free at 473 K for 55 hours and 72 hours in humid and dry air, respectively. Oxidation follows a three-regime kinetics

and the oxidation rate in the linear-regime, controlled by diffusion of Cu^+, is activated with an energy of 0.60 eV. In dry air the oxidation is slower by a factor of 2 and 3 for structures without and with Al_2O_3 inter-layer. The study is expected to serve as a foundation for engineering high-performing scalable diffusion barrier with graphene membranes.

5.1 Introduction

Theoretical and experimental studies on pristine and defect-free graphene have shown that graphene has the ability to outperform the materials that are currently being used as diffusion barriers. The densely-packed sp^2-honeycombed structure makes the monolayer of atoms impenetrable to even atomic He.[35] This when combined with graphene's superior thermal stability, chemical inertness, transparency and flexibility make it a great candidate for barrier applications.[14, 16, 31, 34, 76-79] However, graphene's success as a barrier depends on the ability to reproduce the results obtained from theoretical or pristine graphene using scalable approaches.[23, 24, 80] Initial research by Compton *et al.* has demonstrated that nanosheets of graphene when used as a filler material in polymer films can significantly enhance its barrier properties.[81] A pioneering experimental study by Chen *et al*. has shown that large-area monolayer graphene grown via chemical vapor deposition (CVD) can be used to reduce the oxidation of refined metals even at elevated temperatures up to 200 ° C.[82] Kang *et al*. have also shown similar results using reduced graphene oxide and Yu *et al.* have utilized 30–40 nm thick layers of self-assembled graphene oxide (GO)-polyethleneimine (PEI) composites on PET to reduce the oxygen transmission rate to 0.05 $cc.m^{-2}day^{-1}$.[83] In addition, Kirkland et al. have demonstrated that mixed-thickness CVD-graphene coatings on Ni and Cu can serve as barriers to electrochemical corrosion in aqueous media.[84] Prasai *et al.* have shown that multilayer graphene grown on Ni can act as a better diffusion barrier than a single layer. However, while these demonstrations of scalable graphene barriers have served as an important proof-of-principal, thus far, their performance has still been substantially below their pristine and defect-free counterparts.[85] Previous work by our group has shown that the performance of CVD-graphene based barriers can greatly enhanced via increasing the internucleation distance and stacking of multiple monolayers.[70] In addition, recent studies by Zhou *et al.* and Schriver *et al*. have shown that monolayer graphene promotes extensive electrochemical corrosion of underlying copper over a period of few months and few hours at room and elevated temperatures (~473 K), respectively, thereby severely reducing its ability to perform as a corrosion-inhibiting material.[86, 87] Finally, a recent study by our group has also shown that a graphene monolayer becomes discontinuous due to etching at intrinsic defects and grain boundaries in a matter of few hours in ambient atmosphere at slightly elevated temperatures (>473 C).[55]

In summary, these studies indicate that the problem with using scalable graphene as a barrier is three-fold – (i) high density of defects compared to pristine or theoretical graphene providing spurious diffusion pathways, (ii) degradation and etching of the monolayer graphene at the defective regions at elevated temperatures in ambient atmosphere and (iii) enhanced oxidation of underlying metal in presence of graphene due to electrochemical corrosion. Problem (i) has been and still is one of the most substantial for applications not only pertaining to barriers but also to any application of graphene that requires scalability.[45, 48, 88, 89] Though there are a few ways to minimize the intrinsic defect concentration in scalable-graphene, for example increasing the internucleation distance during the CVD process.[70] However, the graphene manufactured using these techniques is still far from its pristine or defect-free state. Studies to reduce the defect density of scalable-graphene are being constantly pursued by our group and other groups working on synthesis of graphene. In this paper, we focus on addressing the problems (ii) and (iii) which are equally limiting when it comes to ability of graphene to perform as a diffusion barrier. Problem (ii) occurs when the defective regions in monolayer graphene are exposed to air and water. This leads to oxidation of the graphene at the defects and subsequent gasification of the oxidized carbon atom in the form of CO or CO_2, leading to formation holes in the graphene layer in the form of etched pits and grain boundaries.[55] This effect is accelerated at elevated temperatures. The holes formed from the etching process can act as spurious diffusion pathways when monolayer graphene is being used as a barrier membrane. Problem (iii) arises when graphene is in electrical contact with the material that needs protection from oxidation. Due to a difference in the electrochemical potentials of graphene and the underlying material, an electrochemical cell is created that promotes the corrosion of the material, as shown for the case of graphene protecting copper in previous studies.[86, 87]

In order to limit the effect of (iii), we use an ultra-thin layers (~3 nm) of electrically insulating material (Al_2O_3) between the monolayer graphene and the underlying material requiring corrosion protection (Cu). To reduce the effect of (ii), we transfer and stack more monolayers of graphene over the first monolayer, where the subsequent layers of graphene protect the first layer from exposure to air and water. The kinetics, energetics and spatial distribution different barrier structures were studied using temporally-resolved Raman spectroscopy and scanning electron microscopy (SEM). The barriers structures were characterized both quantitatively (Raman) and qualitatively (SEM) by monitoring the degree of oxidation of the underlying bare Cu on which they were stacked or grown to create a protective barrier. In the following section the effects of electrochemical corrosion (5.2.1), number of graphene monolayers (5.2.2), annealing temperature (5.2.3) and water vapor concentration (5.2.4) are critically analyzed. First, in section 5.2.1, we show that using just a 3 nm thick electrically insulating Al_2O_3 interlayer between the graphene and the copper, the degree of oxidation can be significantly reduced by limiting the electrochemical corrosion of copper. In section 5.2.2, we show that transferring multiple layers has a multiplicative effect on the barrier performance. Furthermore, in section 5.2.3, we show that the kinetics of oxidation of the underlying copper foil with the barriers has multiple regimes with annealing time. In particular, in the samples with more than one layer of graphene the oxidation rate increases very slowly at first, which is followed by a linear regime and then a saturation. In addition, the oxidation rate of the linear regime trend has an Arrhenius dependence with temperature with activation energies equaling 0.56 ± 0.06 eV and 0.60 ± 0.06 eV for monolayer graphene barrier w/o and w/ an Al_2O_3 inter-layer, respectively. Finally, in section 5.2.4, we show that the degree of oxidation is directly affected by the presence of water vapor in the atmosphere which accelerates the degradation of the graphene.

5.2 Results and Discussion

The following structures were explored in this barrier study - (i) bare pre-annealed Cu (Cu), (ii) single layer of graphene grown on Cu (gGx1), (iii) single layer of graphene transferred onto gGx1 (tGx1+ gGx1), (iv) three single layers transferred (tGx3+gGx1), (v) single layer of graphene transferred onto Cu (tGx1), (vi) two single layers transferred onto Cu (tGx2), (vii) four single layers transferred onto Cu (tGx4), (viii) 3nm of Al_2O_3 on Cu (AO), (ix) single layer transferred onto AO (tGx1+AO), (x) two single layers transferred onto AO (tGx2+AO) and (x) four single layers transferred onto AO (tGx4+AO). The tests were performed between 298 K and 513 K in a humidity controlled environment and the relative degree of oxidation was quantified using the intensity Raman peak for Cu2O (647 cm-1) vs. annealing time for the different barrier structures, as previously used in literature. The samples were also simultaneously visualized in SEM to monitor the evolution of oxidation qualitatively.

5.2.1 Electrochemical corrosion

Previous studies by Zhou *et al.* and Schriver *et al.* have recently established that graphene has the ability to electrochemically corrode the underlying metal requiring protection due to their difference in electrochemical potentials.[86, 87] In fact the rate of oxidation of underlying metal in the areas where the graphene is defective is hypothesized to be faster compared to even bare copper surface. The reason for this being the fact that graphene provides a much faster route for electron migration to the surface of the copper oxide,[87] a crucial step in the oxide formation process, compared to the alternative on bare copper when the electron has to migrate through an already formed oxide layer to reach its surface.[153] The accelerated electron migration leads to an enhanced production of O^{2-} ions which in turn increases the overall oxidation rate of the copper metal. Figure 5.1a-c shows the SEM micrographs of this electrochemical oxidation process of gGx1 at different times, 0 hours, 5 hours and 20 hours, when the samples were being annealed at 473 K in air with 20,000 ppmv of water vapor. It is clearly seen that the oxidation of the copper surface, indicated by white grain-like features in the images increases with time and eventually by the 20 hour mark covers almost the entire surface (Fig 5.1c). In particular, as seen in previous studies, the oxidation of the copper surface originates at the grain-boundaries and defects in the graphene layer, and then spreads over the entire surface with time.[70, 82, 101] In summary, though the graphene itself is a good diffusion barrier, the accelerated oxide formation underneath it leads to its deterioration and eventual disappearance from the surface of the copper. To prevent graphene for acting as an electrochemical catalyst to the corrosion of underlying metal, in this case copper, it is essential minimize the electrical conductivity between the two to slow down the migration electrons to the surface of the copper oxide layer. To achieve this a very thin layer of aluminum oxide ~3nm is deposited via atomic layer deposition on the surface of the copper before transferring a layer of graphene on top forming the tGx1+AO hetero-barrier stack. When exposed to the same conditions as gGx1 in figure 5.1a-c the tGx1+AO structure performs significantly better as can be seen in figure 5.1d-f. It can be easily observed that isolating the graphene layer from the surface of the copper using an electrically insulating layer drastically reduces the rate of electrochemical corrosion of the copper surface. It is important to point out here that though it is well known that aluminum oxide itself can act as an excellent diffusion barrier as noted by several previous studies, however the minimum thickness of the oxide layer to perform well as a barrier is >200 nm.[154-157] In this study the thickness of the aluminum oxide layer is only 3 nm and at this thickness the oxide layer doesn't perform well as a barrier layer as seen later in figure 5.2.

To relatively quantify the temporal evolution and degree of oxidation of copper under the different types of barrier stacks, gGx1, tGx1, tGx1+AO and AO, spatially averaged Raman spectroscopy of Cu_2O (647 cm^{-1}) is used. Figure 5.2 shows the kinetics of oxidation of the different structures, bare copper Cu (black-squares) and AO (red-circles) oxidize very rapidly when exposed to air (20,000 ppmv water vapor) at 473 K and saturates at a very high value after a 5 hours and 20 hours for Cu and AO, respectively, which can be hypothesized to be limited by the penetration depth of the Raman excitation laser. The oxidation of gGx1(blue-triangles) progresses linearly and eventually also saturates after 24 hours when the surface of the copper is completely oxidized. tGx1 (pink-inverted triangle) behaves very similar to gGx1 sample but the rate of oxidation is marginally lower than gGx1. The electrochemical corrosion is promoted by contact between the graphene and the copper surface and it can be hypothesized the number of contact points between graphene monolayer and the copper surface is less on the transferred layer compared to the layer that was grown resulting in the difference in the oxidation rates. In tGx1+AO (green-diamonds) the oxidation proceeds at a significantly slower rate compared to all the other structures. In particular, the degree of oxidation of the copper surface in tGx1+AO is reduced by at least 38 times and 27 times compared to Cu and gGx1 even after 24 hours of annealing.

5.2.2 Effect of number of layers of graphene

Recent studies by Prasai *et al.* and Singha Roy *et al.* have shown that stacking multiple layer of graphene has a multiplicative effect on the overall barrier performance.[70, 85] Another study by Singha Roy *et al.* has demonstrated that the graphene deteriorates an order of magnitude faster with a 3x reduced activation energy in air when the water vapor concentration in air increased from <2000 ppmv to 15,000 ppmv.[55] Stacking layers of graphene on top of the first layer serves a dual purpose. First, it provides additional barrier layers and reduces degree of oxidation of the copper surface. Second, being hydrophobic in nature, it protects the underlying layers of graphene from exposure to water vapor, thereby minimizing their deterioration and improving their barrier performance. SEM images in figure 5.3a-f show qualitatively the degree of oxidation of the copper surface after 24 hours of annealing in air (20,000 ppmv water vapor) at 473 K. As expected and seen previously in literature, addition of layers on the copper surface progressively decreases it degree of oxidation (Fig. 5.3a-c). However, it clearly seen that the gGx1 (Fig. 5.3b) is completely oxidized to the extent of just Cu (Fig. 5.3a) due to electrochemical corrosion of the copper surface. The oxidation of the surface of copper is reduced by adding a second layer of graphene on top as shown in figure 5.3c (tGx1+gGx1). Adding an aluminum oxide buffer layer reduces this effect as is clearly observed in figures 5.3d-f. In particular, gGx1 (Fig. 5.3b) is completely oxidized after the 24 hour anneal however tGx1+AO (Fig. 5.3e) is only oxidized at the grain boundaries and intrinsic defects of the graphene layer. Figure 5.3g-h compares the degree of oxidation between the tGx3+gGx1 and tGx4+AO after 72 hours of annealing in the same condition. It is clearly observed that tGx4+AO performs better than its counterpart without the aluminum oxide layer.

Furthermore, to relatively quantify the kinetics of the oxidation process, temporally-resolved and spatially averaged Raman spectroscopy is used. It is observed that the Cu_2O Raman peak intensity decreases progressively with the addition of layers on the top of gGx1 (Fig. 5.4). In particular the oxidation of the copper surface is reduced by a factor of at least 1.5, 18 and 40 after 24 hours at 473 K in air (20,000 ppmv water vapor) with addition of one (gGx1), two (tGx1+gGx1) and four layers (tGx3+gGx1) of graphene. These effect is more pronounced with the addition of the aluminum oxide as the intermediate electrically insulating layer. The same ratio is further reduced to 38 for one (tGx1+AO). For two (tGx2+AO) layer and the four layer stacked sample (tGx4+AO), the oxidation is below the equipment's resolution and immeasurable until 30 and 55 hours of annealing, respectively. In particular, even after 72 hours the degree of oxidation in the tGx4+AO sample is reduced by a factor of at least 71 compared to bare Cu and by factor of 7 compared to the tGx3+gGx1 structure which also consists of four graphene layers. It is clearly seen the tGx4+AO combines the effect of AO buffer layer and the graphene stack and is by far the best performing barrier structure.

Furthermore it is also seen that the kinetics of the oxidation process follows consistent trend. Initially the Cu_2O proceeds very slowly, then accelerates to form a linear trend with time and finally it saturates. It can be seen that the onset of this linear regime varies with the number of layers in the graphene stack. With increase in the number of graphene layers, the onset is delayed further. The kinetics and mechanism of oxidation of copper is well understood in literature.[153] The steps involved in the process are follows: (a) Cu+ diffusion from the Cu/Cu_2O

interface to the surface of Cu_2O, (b) e^- diffusion from the Cu/Cu_2O interface to the surface of Cu_2O, (c) O_2 diffusion through the graphene layers to the Cu_2O surface, (d) Formation of O^{2-} and (e) Reaction of Cu^+ and O^{2-}. Step (b) occurs extremely fast for reasons mentioned in section 5.2.1. Also Steps (d) and (e) occur considerably faster compared to steps (a) and (c), making steps (a) and (c) the rate limiting steps. From this, it can be hypothesized that the initial slow increase in the Cu_2O intensity (Fig. 5.4) occurs when the rate limiting step in the oxidation process is step (c). This is further supported by the fact that with addition of number of layers of graphene the time period of this regime increases. The linear regime can be hypothesized to occur when the oxidation process is limited by step (a). This is further supported by the fact that the slope of this linear trend is independent of the number of layers of graphene (Fig. 5.4), suggesting that once there is enough O^{2-} available at the interface the rate of oxidation is limited by the diffusion of Cu^+ ions through the growing oxide layer. The saturation of the intensity at constant level after certain degree of oxidation can be hypothesized to be occurring due to a limitation created by the penetration depth of the Raman laser.

5.2.3 Effect of temperature

In order to study the energetics of the oxidation process, a temperature dependence study is performed in the same environment (air with 20,000 ppmv water vapor). The kinetics of oxidation was studied at three temperatures, 433 K, 473 K and 513 K. Figures 5.5a-c shows the SEM images of gGx1 samples after 24 hours of annealing at 433 K, 473 K and 513 K, respectively, whereas figures 5.5d-f depict the degree of oxidation for the tGx1+AO sample under the same conditions, respectively. As expected, less oxidation is observed in the later samples due a suppressed electrochemical corrosion effect. In order to relatively quantify the dependence on temperature of the oxidation process temporally-resolved and spatially-averaged Raman spectroscopy is used.

Figure 5.6a depicts the kinetics of the Cu_2O Raman peak intensity for gGx1 and tGx1+AO at the above mentioned temperatures. It is observed that the oxidation kinetics follow a similar trend where first there is a linear increase followed by a saturation. The dashed lines show this linear trend for the gGx1 samples are 433 K (red-circles), 473 K (black-squares) and 513 K (blue-triangles). In this regime, the rate of oxidation (R) varies with temperature and has an Arrhenius dependence with temperature, $R = R_0 \exp(-E_A/kT)$ as shown in figure 5.6b, where E_A = activation energy (eV), R_0 = pre-factor (s^{-1}), T = temperature (K) and k = Boltzmann constant (eV K^{-1}). E_A is calculated to be 0.56 ± 0.06 eV and 0.60 ± 0.06 eV for the samples without and with the aluminum oxide layer, respectively, whereas R_0 is calculated to be $(3.71 \pm 0.56) \times 10^8$ h^{-1} and $(1.30 \pm 0.25) \times 10^8$ h^{-1}, respectively. The similar values of E_A suggests that the rate limiting step in the linear oxidation regime is the same for both the types of sample and is the migration of Cu^+ ions to the Cu_2O surface. The difference in the overall oxidation rates between the samples with and without the aluminum oxide layer is caused by the difference in the prefactor (R_0). The relative oxidation rate or the rate of increase of the Cu_2O Raman peak intensity (R) at room temperature can be extrapolated to be 0.142 h^{-1} and 0.0091 h^{-1} without and with the Al_2O_3 layer, respectively. This suggests that the oxidation of the copper surface is appreciable in a matter of few months at room temperature for gGx1 similar to previous observations made in literature. However, the corrosion is negligible when an intermediate aluminum oxide layer is added between the graphene and the copper surface (tGx1+AO) after the same amount of time.

5.2.4 Effect of water vapor

It has been previously shown by Singha Roy *et al*. that the graphene itself degrades at elevated temperature (~473 K) and this degradation creates new defects that can act as new spurious diffusion pathways for oxygen to reach the underlying copper and oxidize it.[55, 70] In addition the same group has also shown that the reducing the amount the water vapor content in air reduces slows down the degradation process of graphene on SiO_2. In order to explore the effect of water vapor in the barrier performance of the heterostructures the samples were exposed to two different environments at 473 K - (i) humid air (20,000 ppmv water vapor) and (ii) dry air (<7 ppmv water vapor) and the kinetics of oxidation of the copper surface was studied using Raman spectroscopy. Figures 5.7a and 7b depict the SEM micrographs of the gGx1 structure that were annealed for 24 hours in humid and dry air environment, respectively. It is clearly seen that the degree of oxidation is less for the sample exposed to dry air compared to the one exposed to the humid air environment. Similar effect is seen for the samples with aluminum oxide layer (tGx1+AO) as shown in figures 5.7c and 7d, however, the overall degree of oxidation is reduced compared to gGx1 in both cases (humid and dry environment).

To relatively quantify and compare the kinetics of oxidation for both dry and humid air, Raman spectroscopy was used. In particular, degree of oxidation after 24 hours of annealing at 473 K, is reduced by a factor of 2 and 3 for gGx1 and tGx1+AO, respectively going from humid to dry environment (Fig. 5.8). Furthermore, the oxidation was limited to the equipment resolution for tGx4+AO sample even after 72 hours of annealing dry air. The above results suggest that water vapor plays an important role in accelerating the diffusion process through the graphene barriers by creating new defects in them with time. It is also important to mention that the water vapor has been known to accelerate the corrosion itself and it can be hypothesized that eliminating or reducing water vapor in air can serve a dual purpose, namely slowing down the corrosion of the copper itself and also improving the oxidative stability of the graphene layers.

5.3 Implications and conclusions

Experimental and theoretical studies on pristine and non-scalable graphene have shown that graphene is an excellent choice when it comes to barrier material. However, recent experimental studies with scalable forms of graphene haven't been able to match the expectations and predictions of their pristine counterparts. In summary, previous studies indicate that the problem with using scalable graphene as a barrier is three-fold – (i) high density of defects compared to pristine or theoretical graphene providing spurious diffusion pathways, (ii) degradation and etching of the monolayer graphene at the defective regions at elevated temperatures in ambient atmosphere and (iii) enhanced oxidation of underlying metal in presence of graphene due to electrochemical corrosion. This work focuses on addressing problems (ii) and (iii). In order to limit the effect of (iii), an ultra-thin layers (~3 nm) of electrically insulating material (Al_2O_3) is added between the monolayer graphene and the underlying material requiring corrosion protection (Cu). To reduce the effect of (ii), more monolayers of graphene are transferred and stacked over the first monolayer, where the subsequent layers of graphene protect the first layer from exposure to air and water.

It is found that adding an ultra-thin layer of electrically insulating material between graphene and copper the degree of oxidation is reduce by at least by a factor of 38 and 27 compared to bare Cu and gGx1, repectively, after 24 hours of oxidation by suppressing the effect of electrochemical corrosion of the copper surface. Furthermore, stacking additional layers of graphene over the first layer improves the barrier performance progressively. Additional layers of graphene are not only able to serve independently as barriers themselves but also protect the underlying graphene layers from water vapor and oxygen which enhance their degradation. When combined with the suppressed electrochemical corrosion due to the addition of aluminum oxide buffer layer superior barrier performances can be achieved. In particular, tGx4+AO sample has no detectable oxidation until 55 hours of annealing in humid air at 473 K. For the multilayer graphene stacked heterostructure barriers, the oxidation kinetics has three distinct regimes, (i) very slow gradual increase, followed by a (ii) linear regime and finally a (iii) saturation regime. It is hypothesized that during regime (i) oxidation is limited by O_2 diffusion through the graphene layers, in regime (ii) it is limited by the diffusion of Cu+ ions through the growing oxide layer and the saturation in regime (iii) is reached when the thickness of the Cu_2O is more than what the Raman laser can penetrate. The oxidation kinetics is also dependent on the ambient temperature and oxidation rate is proportional to $R = R_0 \exp(E_A/kT)$, where E_A is calculated to be 0.56 ± 0.06 eV and 0.60 ± 0.06 eV for the samples without and with the aluminum oxide layer, respectively, whereas R_0 is calculated to be $(3.71 \pm 0.56) \times 10^8\ h^{-1}$ and $(1.30 \pm 0.25) \times 10^8\ h^{-1}$, respectively. This suggests that the oxidation of the copper surface is appreciable in a matter of few months at room temperature, however, the corrosion is negligible in the same amount of time when an intermediate aluminum oxide layer is added between the graphene and the copper surface. It is finally found that removing water vapor from ambient air improves the barrier performance by 2 and 3 times for gGx1 and tGx1+AO, respectively after 24 hours of annealing at 473 K. Also, the oxidation is immeasurable for tGx4+AO sample even after 72 hours of annealing in dry air.

In summary, this study will help developing a deeper understanding of how environmental factors negatively affect the use CVD-graphene as corrosion protecting layer for refined metals. Furthermore, results from this study can be used to relatively quantify the kinetics of oxidation for similar barrier structures at any given temperature. Finally, this study is expected open new doors and lay the foundation for engineering scalable barriers with graphene that can match its pristine and non-scalable counterparts.

5.4 Experimental Methods

Sample preparation: The graphene barriers for our studies were grown one layer at a time on Cu foils using standard atmospheric pressure chemical vapor deposition (CVD) commonly used to grow monolayer graphene. Prior to CVD, the Cu foils (Alfa Aesar 99.8% Lot # 13382) were annealed in a reducing forming gas environment (17 sccm H_2, 320 sccm Ar) at 1030 °C for 8 hours. The growth of graphene was achieved by adding a 0.250 sccm CH_4 flow for 180 min at 1030 °C. Bare Cu samples without graphene were produced by annealing in forming gas at 1030°C for 11 hours but never introducing methane. Al_2O_3 layer was deposited using atomic layer deposition which was achieved by 500 ms H_2O pulsing + 60 s N_2 purging + 500 ms Trimethylaluminum (TMA) pulsing + 60 s N_2 purging at 300 °C. A growth rate is ~ 0.1 nm/cycle was achieved using this technique and 30 cycles were performed to achieve the 3 nm thickness. Stacked barrier structures were fabricated by mechanically transferring additional layers with the help of a sacrificial layer of poly(methyl methacrylate), using a transfer approach derived from that of Singha Roy *et al.*, Safron *et al.*, and others for transferring graphene to arbitrary substrates.[34, 91, 102] Oxidation was carried out in three heating zone closed furnace tube. Water vapor concentration inside the furnace was controlled via regulating the flow of the carrier gas (Dry air <7 ppmv water vapor) through a water-bubbler. The concentration of water vapor was monitored via an *in-situ* hygrometer and thermometer.

Characterization: After oxidation, the samples were imaged using Scanning Electron Microscopy (SEM LEO 1530, 3 keV) and optical microscopy. The oxidation of the Cu was quantified temporally and spatially using imaging Raman spectroscopy (DXR*xi* MicroRaman Thermo Fisher Scientific, excitation λ = 532 nm, 4 mW). The pixel size of the scans was 0.5 μm x 0.5 μm and the laser spot size was also ~1 μm. The laser power and exposure time were sufficiently low that the Raman laser did not induce oxidation of the Cu during measurement, combined with high-frequncy raster scanning technique of the equipment, the effect of the laser on the substrates temperature is negligible. The amplitude of the Cu_2O component of each Raman spectrum was determined by fitting. Each spectrum was fit from 450 – 850 cm^{-1} using the Raman spectrum of the oxidized bare Cu sample as a reference spectrum for Cu_2O and a sixth order polynomial to account for the broad background and interference effects. The full-width at half-maximum of the main Cu_2O peak at 647 cm^{-1} was only 50 cm^{-1} and could not be reproduced by the polynomial background, which was forced to fit over the entire 450 – 850 cm^{-1} range. Thus, this fitting protocol successfully was able to extract the Cu_2O component of each spectrum.

Acknowledgements: The majority of the experimental Raman spectroscopy and electron microscopy work was supported by the National Science Foundation (Grant number CBET-1033346). The experimental Raman spectroscopy and electron microscopy were partially supported by Wisconsin Energy Institute. MSA also acknowledges partial support from a 3M Non-Tenured Faculty Grant. The authors gratefully acknowledge use of facilities and instrumentation supported by the NSF-funded University of Wisconsin Materials Research Science and Engineering Center (DMR-1121288).

Figures:

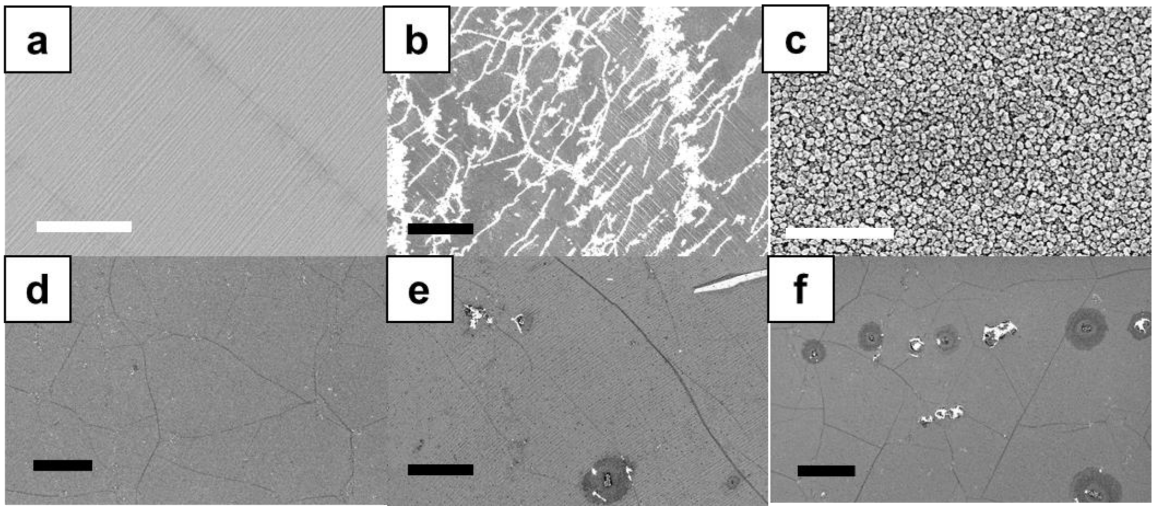

Figure 5.1. Electrochemical corrosion of copper from single layer of graphene: (a), (b) and (c) represent SEM images of gGx1 after 0 hour, 5 hour and 20 hour annealing, respectively in humid air (20,000 ppmv) at 473 K. (d), (e) and (f) show SEM images of tGx1+AO after 0 hour, 5 hour and 20 hour annealing, respectively under the same conditions. Electrochemical corrosion of copper by the graphene layer is suppressed in the later case due to the presence of Al_2O_3. (white scalebars = 2 µm and black scalebars = 5 µm)

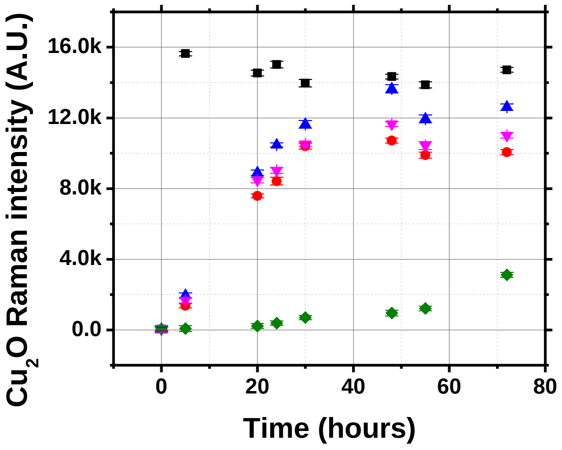

Figure 5.2. Oxidation kinetics of barrier structures with single layer of graphene in humid air (20,000 ppmv water vapor) at 473 K. Cu, AO, gGx1, tGx1 and tGx1+AO represented by black-squares, red-circles, blue-triangles, pink-inverted triangles and green-diamonds, respectively.

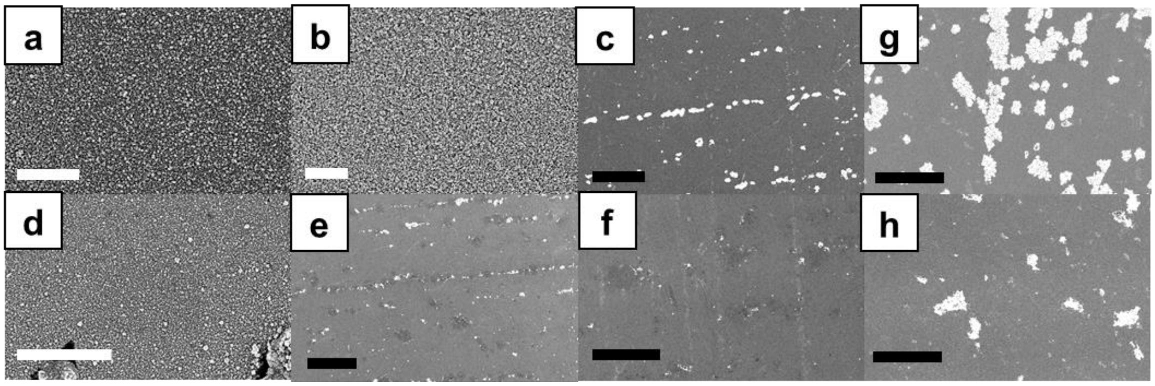

Figure 5.3. Layer dependence of oxidation without and with Al_2O_3 buffer layer: (a), (b) and (c) show SEM images of samples Cu, gGx1 and tGx1+gGx1, respectively after 24 hours of annealing in humid air (20,000 ppmv water vapor) at 473 K. (d), (e) and (f) show SEM images of samples AO, tGx1+AO and tGx2+AO, respectively after 24 hours of annealing in humid air (20,000 ppmv water vapor) at 473 K. (g) and (h) SEM image of tGx3+gGx1 and tGx4+AO, respectively after 72 hours of annealing in the same conditions as (a)-(f). (white scalebars = 2 µm, black scalebars in (c, e and f) = 20 µm, black scalebars in (g and h) = 10 µm)

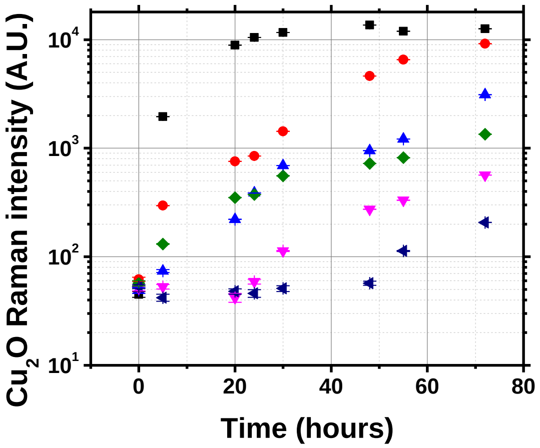

Figure 5.4. Oxidation kinetics of stacked barrier structures in humid air (20,000 ppmv water vapor) at 473 K. gGx1, tGx1+gGx1, tGx3+gGx1, tGx1+AO, tGx2+AO and tGx4+AO represented by black-squares, red-circles, green-diamonds, blue-triangles, pink-inverted triangles and navy tilted triangles, respectively.

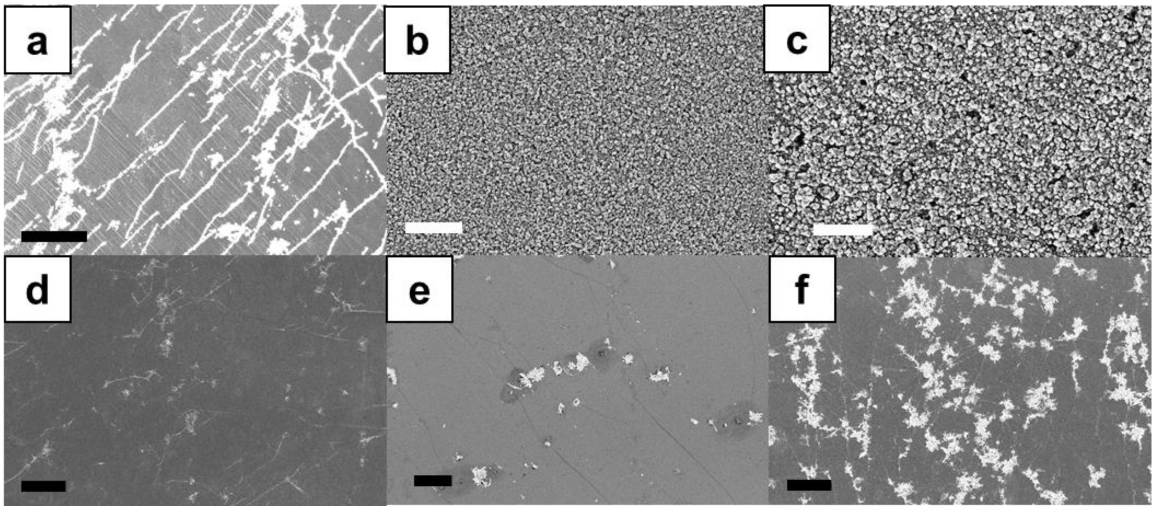

Figure 5.5. Temperature dependence of oxidation for single layer of graphene without or with Al_2O_3 buffer layer: (a), (b) and (c) represent SEM images of gGx1 after 24 hours of annealing in humid air (20,000 ppmv) at 433 K, 473 K and 513 K, respectively. (d), (e) and (f) represent SEM images of tGx1+AO after

24 hours of annealing in humid air (20,000 ppmv) at 433 K, 473 K and 513 K, respectively. (white scalebars = 2 µm and black scalebars = 5 µm)

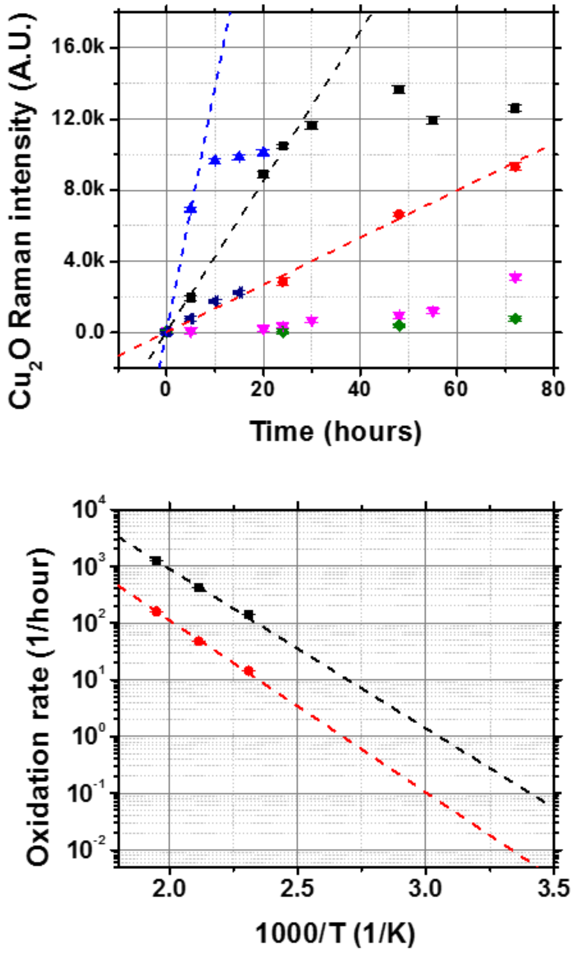

Figure 5.6 (a) Temperature dependence of oxidation kinetics in without and with Al_2O_3 buffer layer in humid air (20,000 ppmv water vapor). Red-circles, black-squares and blue-triangles represent oxidation of gGx1 at 433 K, 473 K and 513 K, respectively. Green-diamonds, pink-inverted triangles and navy tilted triangles represent oxidation of tGx1+AO at 433K, 473 K and 513 K, respectively. Dashed lines show the initial linear trend in the oxidation for the gGx1 samples and are used to compute the respective oxidation rates. (b) Energetics of oxidation in the linear regime for gGx1 and tGx1+AO in humid air (20,000 ppmv

water vapor): Black-squares and red-circles show the Arrhenius dependence of gGx1 ($E_A = 0.55 \pm 0.06$ eV) and tGx1+AO ($E_A = 0.60 \pm 0.06$ eV), respectively.

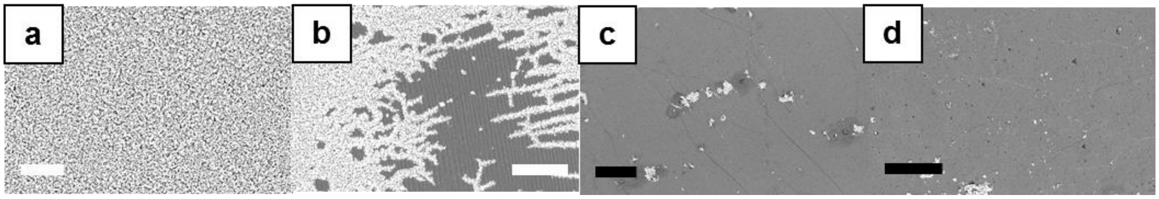

Figure 5.7. Effect of water vapor concentration on oxidation without and with the Al_2O_3 buffer layer annealed at 473 K for 24 hours: (a) and (b) depict SEM images of gGx1 in humid (20,000 ppmv water vapor) and dry air (<7 ppm water vapor). (c) and (d) represent SEM images of tGx1+AO in humid (20,000 ppmv water vapor) and dry air (<7 ppm water vapor). (white scalebars = 2 µm and black scalebars = 5 µm)

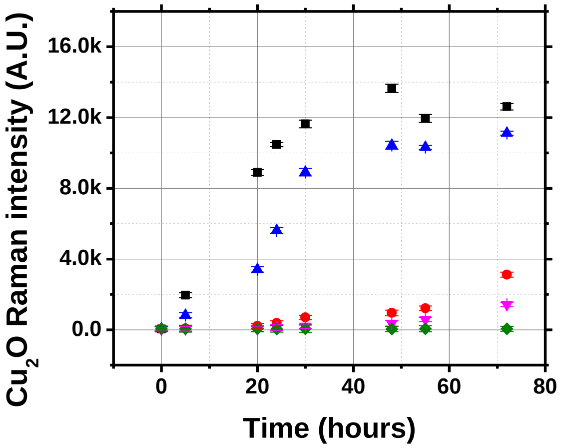

Figure 5.8. Effect of water vapor concentration in air on the oxidation kinetics of gGx1 and tGx1+AO annealed at 473 K: Black-squares and red-circles represent the kinetics of gGx1 in humid (20,000 ppmv water vapor) and dry air (< 7 ppmv water vapor), respectively. Blue-triangles and pink-inverted triangles represent the kinetics of tGx1+AO in humid (20,000 ppmv water vapor) and dry air (< 7 ppmv water

vapor), respectively. Green-diamonds, represent kinetics of tGx4+AO in dry air and is immeasurable until at least 72 hours.

6. Graphene in organic photovoltaics

This chapter is adapted from “Singha Roy. S.; Bindl, D. J.; Arnold, M. S., Templating Highly Crystalline Organic Semiconductors Using Atomic Membranes of Graphene at the Anode/Organic Interface. *Journal of Physical Chemistry Letters* **2012,** 3, (7).” SS synthesized and transferred graphene, deposited organic film, performed X-ray diffraction analysis, Raman spectroscopy scanning electron microscopy and analyzed data. DJB performed the optical characterization.

Abstract

Charge and energy transport in organic semiconductors is highly anisotropic and dependent on crystalline ordering. Here, we demonstrate a novel approach for ordering crystalline organic semiconductors, with orientations optimized for optoelectronics applications, by using a single monolayer of graphene as a molecular template. We show, in particular, that large-area graphene can be integrated on metals and oxides to modify their surface energies and used to template copper phthalocyanine (CuPc), a prototypical organic semiconductor. On unmodified substrates, thermally evaporated films of CuPc are small-grained and the molecules are in the “standing-up” (100) orientation. On graphene modified substrates, CuPc is templated in favorable “lying-down” (11-2) and (01-2) orientations with drastically larger crystal sizes. This

results in an 86% increase in the absorption coefficient at 700 nm and should furthermore result in enhanced energy and charge transport. The use of highly conductive and transparent (> 95%) graphene membranes as templates is expected to be a foundation for developing future planar and nanostructured OLEDs and OPVs with improved performance.

Small molecule organic semiconductors are attractive materials for applications in light emitting diodes (OLEDs), photovoltaic solar cells (OPVs), photodetectors, thin-film field-effect transistors (FETs), and other electronic/optoelectronic devices, because of their potential for low-temperature processability, strong and broadband optical absorptivity, efficient light emission, and tunable chemical structures and properties.[158] The charge and energy transport characteristics of organic semiconductors are typically highly anisotropic and are strongly dependent on crystalline ordering and molecular orientation.[159-161] Thus, learning how to control these parameters is an important aspect of improving their performance in applications.

While there has been substantial success in controlling the ordering of monolayers or few-layers of organic semiconductors and to optimize the transverse charge transport mobility of organic field effect transistors (FETs),[162-168] there has been relatively less progress in controlling the ordering and orientation of organic films for OLEDs and OPVs. Films in these devices must be considerably thicker (100’s of Å) and charge and energy (exciton) transport in them must be optimized normal to the growth substrate and the device stack, in the direction of charge injection or extraction. For approximately planar molecules, optimized transfer is generally in the direction of π-π stacking. Thus, for organic FETs, a “standing-up” molecular orientation is typically desired, whereas in OLEDs and OPVs, a “lying-down” orientation is more optimal.

A "lying-down" morphology can be driven in the first monolayer by a strong molecule-substrate interaction.[169, 170] However, in most cases the lattice parameters of the organic semiconductor do not match the substrate, resulting in a strain energy that builds with increasing film thickness beyond a few monolayers, ultimately resulting in disorder.[171, 172] In order to achieve a "lying-down" morphology that is sustained beyond several molecular layers, the molecule-substrate interaction must be weaker, more comparable to the inter-molecular interaction energy,[169] to accommodate the relaxation of the strain in the first monolayer, but still strong enough to orient the organic film.

Previously, several studies have identified substrates that have the proper molecule-substrate interactions to induce this "lying-down" morphology for thick, oriented films of polyacenes, perylene-derivatives, and phthalocyanines. The substrates include graphite (HOPG)[173], MoS_2 [162], copper iodide [174], alkali metal halides [175], and even other organic molecules such as perylene-3,4,9,10-tetracarboxylic-3,4,9,10-dianhydride (PTDCA) [176-178]and pentacene.[179] One problem however is that the integration of films grown on these templates into optoelectronic devices has proved to be challenging because these templates are either partially or completely opaque or poorly conducting. Furthermore, the transfer of oriented films from these templates into separate device stacks is not straightforward.

Here, we demonstrate a novel approach for overcoming these challenges by implementing a template based on a monolayer of graphene. The graphene template is only a single atomic layer < 0.5 nm in thickness, > 95% transparent and highly conductive . Aside from templating, the exceptional properties of graphene make it an excellent transparent conductor for optoelectronics, either on insulators or to modify the surface of transparent conductors such as indium tin oxide (ITO). [14, 78] At the same time, graphene's conjugated aromatic structure makes it an ideal template for growing oriented and crystalline films of organic semiconductors. Graphene can be integrated onto arbitrary substrates, thereby modifying the substrates to give them an interfacial surface energy comparable to that of HOPG. Although graphene has been previously utilized as a transparent conductor in both OLEDs and OPVs [180], it has typically been over-coated by a layer of PEDOT:PSS prior to the deposition of the active organic layers, and therefore graphene has not yet been fully exploited as a template to orient the growth of films for these optoelectronics applications. Other groups have started taking the first steps toward examining the assembly of molecules on graphene. For example, Ling et al. have studied Raman scattering from sub-monolayers assembled on graphene.[181] Furthermore, Mao et al. have recently employed NEXFAS to characterize π-π stacking (perpendicular to the substrate) of a few layers of chloroaluminum phthalocyanine on graphene on ITO and have used UPS to study its interface electronic structure.[43] Here, we demonstrate that graphene can be employed to modify the surface energy of both metals and oxides, allowing these substrates to template of highly crystalline films of substantial thickness > 320 nm of organic semiconductors of controlled orientation. The oriented and unoriented films are strikingly different, even by eye. We gain unique insight into the templating using x-ray diffraction, electron microscopy, and optical transmission spectroscopy and have specifically examined a prototypical organic semiconductor, copper phthalocyanine (CuPc), commonly used in OPVs as a light absorbing and hole transporting material and as well as in OLEDs as a hole-injection layer, as a proof-of-principal.[158, 182-185] On unmodified metal and oxide surfaces, thermally evaporated films of CuPc are small-grained and the CuPc molecules are undesirably in the "standing-up" orientation. However, by modifying these substrates with a single atomic layer of graphene < 0.5 nm in thickness, we show that the

CuPc can be driven to “lie-down” and that this orientation can be maintained through 100′s of nm in CuPc film thickness, with drastically larger lateral crystal sizes.

In order to create graphene modified metal and oxide surfaces, we first grew monolayered graphene via atmospheric pressure chemical vapor deposition on Cu foils that has been previously demonstrated by Ruoff and coworkers.[43, 53, 180] In some instances, we left the graphene directly on the Cu foils (defined as graphene modified copper, GMC), and in other instances we transferred the graphene onto glass (defined as graphene modified glass, GMG) with the help of a polymer support using processes similar to those that have been reported in literature for transferring graphene to a wide range of substrates.[93] The process-flow is depicted in Figure 6.1. Clean copper foils (6 cm x 4 cm x 0.025 mm) were used as the substrate to grow monolayered graphene by Atmospheric Pressure Chemical Vapor Deposition (AP-CVD). To start, the substrates were annealed in forming gas (95% Ar + 5% H_2) (flow-rate = 340 sccm) at 1050 °C for 30 min. Upon completion of the annealing, the temperature was reduced to 1030 °C. Following, methane was introduced at 31 ppm, for 4 hours, to grow the graphene. After the growth, the furnace was cooled rapidly at 15 °C min^{-1} to 150 °C. Copper foils with graphene, denoted here as Graphene Modified Copper (GMC), were then spin-coated with 1500 Å of poly(methyl methacrylate) (PMMA - 2 % wt.) in chlorobenzene, as a sacrificial support. The graphene on the bottom-side of copper was removed by a 4 minute sonication using a bath-sonicator. The copper was then removed using an etchant comprised of a mixture of 0.2 M $FeCl_3$ and 0.2 M HCl. Residual copper was removed in 1% HF. The graphene supported by the PMMA was then transferred to arbitrary substrates such as glass, ITO, and SiO_2 and the layer of PMMA was removed via a series of heated solvent baths comprising of acetone (x2), dichloromethane (x2) and isopropanol (x2), followed by a two hour anneal in forming gas (95% Ar + 5% H_2) at

500 °C to remove any residual PMMA. We found the forming gas anneal very critical to our process-flow, resulting in more atomically pristine graphene surfaces more analogous to freshly cleaved HOPG. Graphene transferred to a SiO_2 substrate was used for the Raman spectroscopy measurement.

The above mentioned process can be easily scaled to any substrate size with the utilization of larger growth substrates. In our process, the graphene atomic layer was intentionally made to cover only part of the substrate in-order to have a side-by-side comparison of the templated and the non-templated regions.

Different thicknesses of CuPc (sublimed grade, 99.9%, Sigma-Aldrich) were thermally evaporated at 0.3 Å s^{-1} in high vacuum ($2x10^{-6}$ torr). We characterized the crystallinity and orientation by performing a θ-2θ scan of the CuPc films using a STOE X-ray Diffractometer operating at 40.0 kV and 25.0 mA with Cu-Kα (wavelength =1.542 Å). A quartz tungsten halogen lamp coupled to a monochromator was used to measure absorption spectra.

After graphene growth and transfer, we employed Raman spectroscopy to characterize the structure, number of layers, and quality of the resulting graphene (Figure 6.2a). A typical Raman spectrum is plotted in Figure 6.2a, which shows a characteristic G and the 2D peak at ~1580 cm^{-1} and ~2640 cm^{-1}, respectively. The 2D peak can be fit by a single Lorenztian and the ratio of the amplitude of the 2D peak to the G peak was 3.3, indicating that the graphene predominantly consists of a single layer.[64] The absence of a defect D-band Raman peak at ~1350 cm^{-1} signifies that the graphene is of high-quality with minimal defects. To explore templating, CuPc was thermally evaporated at high vacuum ($2x10^{-6}$ torr) on these bare and graphene modified substrates.

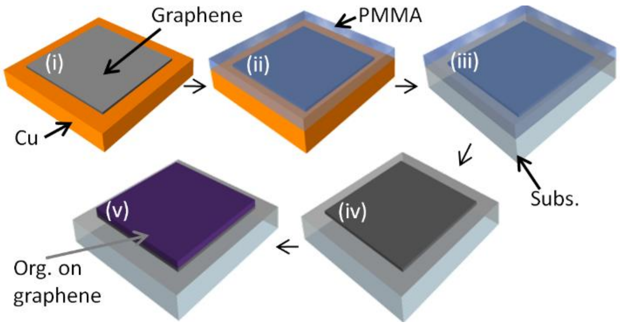

Figure 6.1. Process-flow. (i) Graphene on copper (GMC) grown by AP-CVD; (ii) PMMA-support spin-coated on graphene on copper; (iii) PMMA-supported graphene transferred to glass after removal of copper; (iv) Graphene on a glass (GMG) after removal of PMMA-support; (v) CuPc thermally evaporated on graphene template.

An optical image of graphene modified glass (GMG) is shown in Figure 6.2b-c. The graphene uniformly and continuously covers the middle of the substrate and is highly transparent. After the deposition of an 80 nm film of CuPc, there is a difference in appearance of the CuPc film on the graphene (Figure 6.2c). At normal incidence, the CuPc film on bare glass is blue whereas the film on the GMG is reddish-purple. To further characterize this difference, we spectrally resolved optical transmission. The transmission losses due to the graphene layer, alone, were < 5% across the entire spectrum and only 2.7% from 800-1500 nm, consistent with that of a single layer of graphene (Figure 6.2d). The CuPc absorption is identified by a pair of peaks at 620 nm and 700 nm. The optical absorptivity of CuPc on the GMG is stronger than its absorptivity on bare glass, across the entire spectrum, for example, with an absorption coefficient that is 50% higher at 664 nm (Figure 6.2d). Furthermore, the Q-band region (~ 700 nm) of CuPc on the GMG is particularly enhanced. It is well known that the morphology and molecular orientation of a film can affect its optical properties and has been previous reported by Sullivan et al.[178] We next utilized scanning electron microscopy (SEM) to characterize the morphology of these films in more detail.

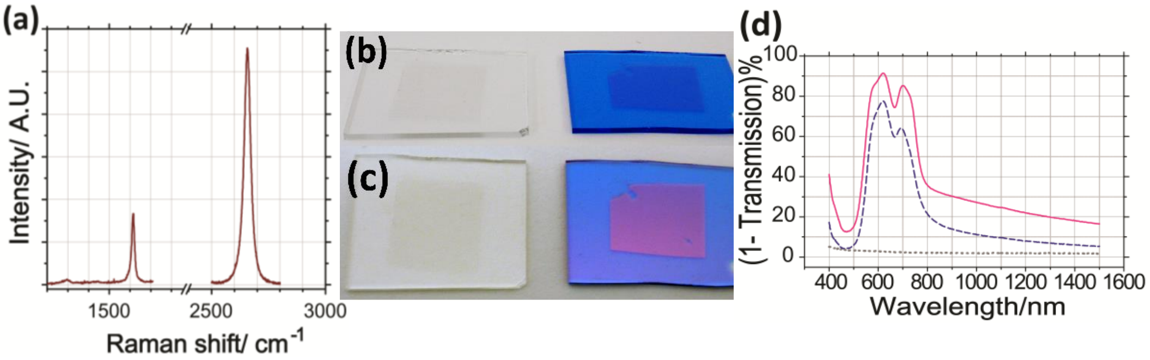

Figure 6.2. (a) Raman spectrum of a single monolayer of graphene (on SiO_2 on Si). (b-c) Optical images of GMG (left) and CuPc on GMG (right). (d) Optical transmission through GMG (dotted/grey), CuPc on GMG (solid line/pink), and CuPc on bare glass (dashed/blue), at normal incidence.

To investigate further, we looked at the above samples in the SEM. On both the bare Cu and bare glass substrates, the CuPc formed small domains of 38 nm and 34 nm respectively in lateral extent (Figure 6.3). In contrast, the film morphology drastically changed when it was deposited on a single layer of graphene that modifies these substrates. On the GMC and GMG we observed significantly larger domain sizes, but it was difficult to quantify them as we couldn’t observe distinct grains. However, the average distance between the consecutive holes on GMC and GMG were measured to be 241 nm and 125 nm respectively, providing a lower limit to the grain sizes on them. We believe the factors limiting the lateral domain size were non-uniformities in the underlying substrate. The difference in lateral domain sizes of GMC and GMG might be caused by increased surface roughness after the graphene is transferred to glass due to (i) occurrence of folds during the transfer process and/or (ii) the presence of small amount of residual PMMA left even after the forming gas anneal, which could affect the surface energy of the graphene and hence interfere with the templating (making the domain sizes slightly smaller). Near the edges of the substrate, where the graphene membrane abruptly ends and the bare substrate is exposed (Figure 6.2b-c), the transition between the different morphologies was sharp, as observed in Figure 6.3, in which the morphology changes from ordered to disordered. The morphology of the CuPc on the graphene modified substrates was invariant for the thicknesses explored, from 20 nm to 320 nm.

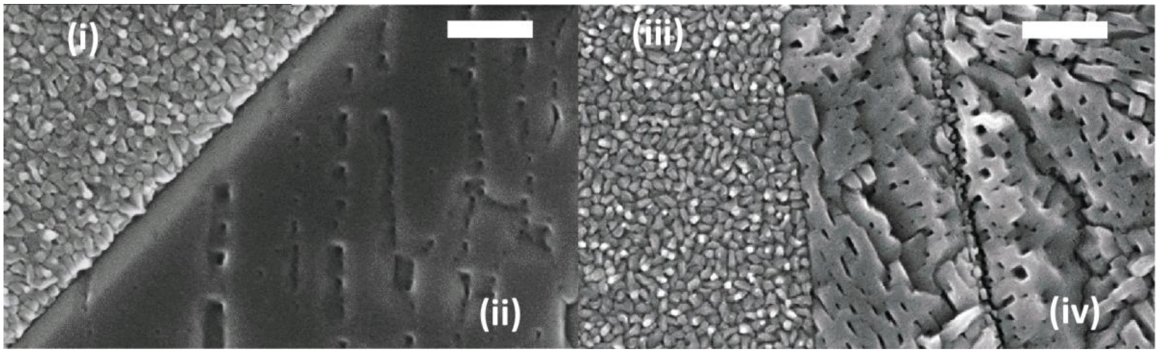

Figure 6.3. Scanning electron micrographs of 80 nm film of CuPc thermally evaporated on (i) bare copper, (ii) GMC, (iii) bare glass, and (iv) GMG. Scalebars = 300 nm.

We employed x-ray diffraction in order to further investigate differences in morphology and crystalline orientation, using the refined crystal structure of α-CuPc recently reported by Hoshino et al. [186] to interpret our data. The films of CuPc on bare glass and bare Cu were dominated by a Bragg peak at 2θ = 6.83º (Figure 6.4b and 6.4e). In contrast, on GMC and GMG, this peak nearly completely disappeared and two new Bragg peaks at 2θ = 26.6º and 2θ = 27.7º emerged (Figure 6.4c and 6.4f). The humps between 20° to 30° in Figure 6.4a and 6.4b and 5° to 10° in Figure 6.4d and 6.4e are attributed to background scattering from glass and copper, respectively. These diffraction data tell us that the (100) plane of α-CuPc satisfies the Bragg's condition on bare substrates, which corresponds to the molecules "standing-up" on the surfaces, as depicted in Figure 6.5a and 6.5c. In contrast, the 2θ = 26.6º and 2θ = 27.7º indicate stacking in the direction of the (11-2) and (01-2) Bragg planes, corresponding to a nearly "lying-down" conformation, in which the molecules form stacked columns as depicted in Figure 6.5b and 6.5d. These observations are similar to those reported by Wang et al. on HOPG [173] and by Lassiter et al. on PTDCA templates [177]. However, here, the orientation has been driven, remarkably, only by a single layer of atoms, which is conductive, highly transparent, and directly integrable onto a wide variety of substrates.

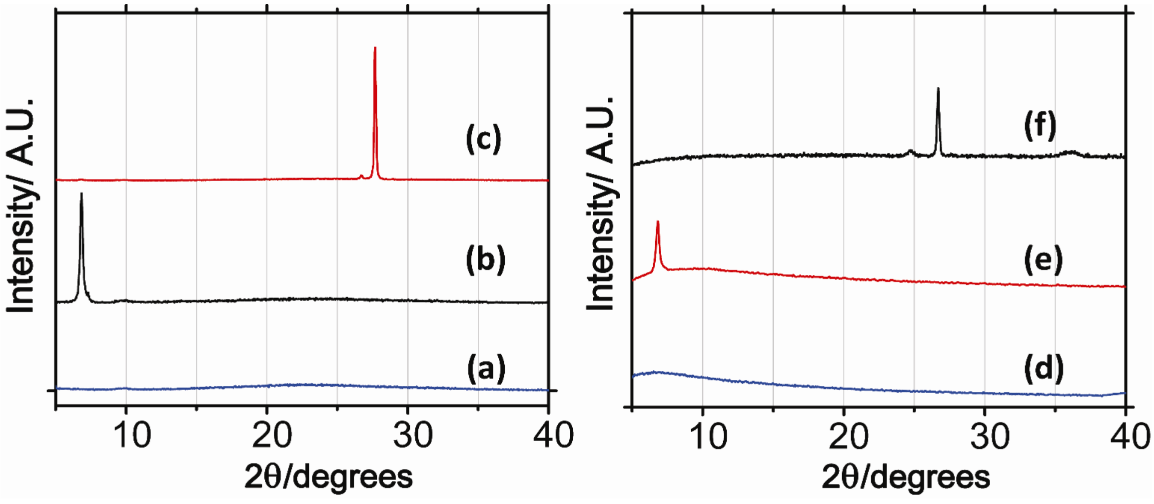

Figure 6.4. X-ray diffraction of (a) glass, (b) 80 nm of CuPc on bare glass, (c) 80 nm of CuPc on GMG, (d) bare copper, (e) 80 nm CuPc on bare copper, and (f) 80 nm of CuPc on GMC. Peaks at 2θ = 6.8° correspond to diffraction from the α-CuPc (100) Bragg plane, corresponding to the "standing-up" molecular orientation depicted in Fig. 6.4a,c. Peaks at 2θ = 26.6° and 27.7° correspond to diffraction from the α-CuPc (01-2) and (11-2) Bragg planes, respectively. The (11-2) molecular orientation is depicted in Fig. 6.4b,d.

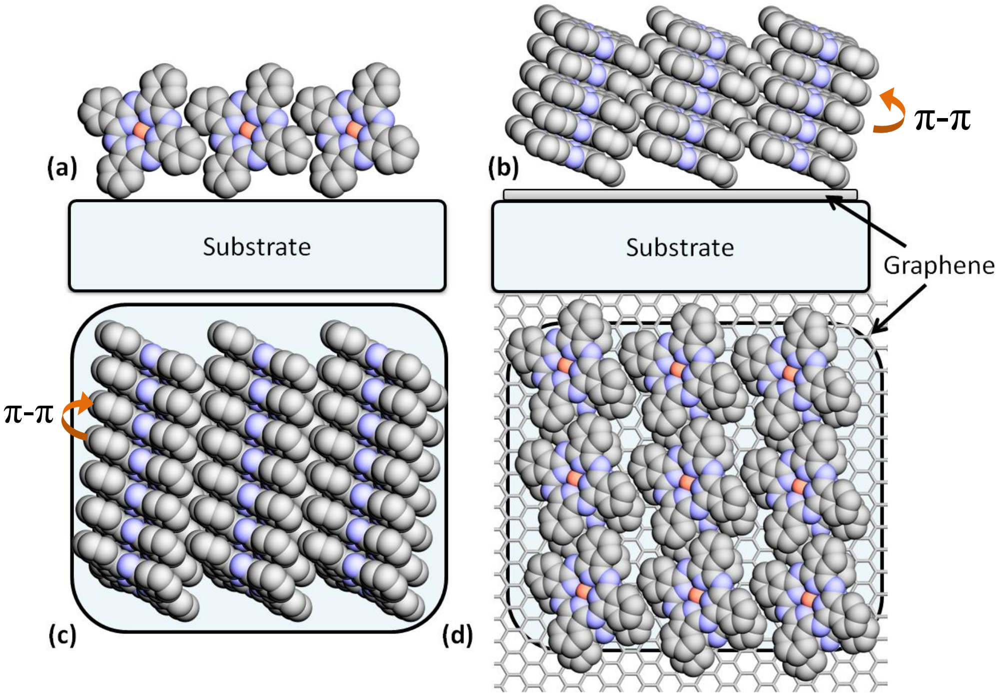

Figure 6.5. A graphical representation of the orientation of CuPc on bare glass and GMG. (a) and (c) depict the "standing-up" orientation of the CuPc molecules on glass with the α-CuPc (100) plane normal to the substrate. (b) and (d) depict "lying-down" orientation of the CuPc molecules on GMG with the α-CuPc (11-2) Bragg plane normal to the substrate. The arrows on (b) and (c)

indicate the π-π overlap and in-turn the favored direction of charge and energy transport for optoelectronics and transistor applications.

Also, the peaks positions and widths of the XRD spectra were independent of film thickness over the explored range of 20 nm to 320 nm, indicating that the orientation of the CuPc was invariant over this range (Figure C.S1 of the Supporting Information). Taken together, the contrast between the SEM images and XRD spectra on bare surfaces and graphene modified surfaces is striking and convincingly shows that a single layer of carbon atoms can drive the orientation and crystallization of an organic layer on both metallic and oxide substrates, masking the molecule-substrate interactions that would normally be expected on their native surfaces.

The preferred orientation of CuPc on HOPG has previously been predicted by comparing the energetics of inter-molecular CuPc interactions and the interactions of CuPc with HOPG. The edge-on inter-CuPc interaction energy, the inter-CuPc π-π stacking energy, and the adsorption energy of CuPc "lying-down" on HOPG have been estimated by Yin et al. as -0.087, -1.09, and -2.65 eV molecule^{-1}, respectively.[164, 187] The lateral corrugation barrier for CuPc on HOPG is as low as 8.7 meV molecule^{-1}, thereby facilitating efficient lateral diffusion of the molecules over the surface and the creation of a uniform monolayer. Thus, on HOPG, a "lying-down" orientation of CuPc is preferred over "standing-up" stacking. Although the adsorption energetics likely change for CuPc molecules on a single monolayer of graphene compared with HOPG, due to incomplete screening of the underlying substrate by graphene, we believe that the surface energies are nonetheless similar. This conclusion is supported by the fact that the CuPc film orientation and crystallinity that we report here is similar to that previously reported on HOPG.

The benefits of templating CuPc in the “lying-down” conformation in OPV devices are potentially threefold: (i) increased optical absorption and shorter absorption length (L_A), (ii) faster exciton migration and increased exciton diffusion length (L_D), and (iii) enhanced charge transport mobility (μ). These effects all stand to increase the power conversion efficiency of planar and planar-nanostructured small molecule OPVs, which are currently limited in efficiency by the poor mismatch of L_A to L_D. From Figure 6.2, it is evident that the optical absorptivity of the CuPc films, for light propagating normal to the substrate, is increased by templating. Optical absorptivity is proportional to the square of the scalar product of the transition dipole moment and optical polarization. It is known that the transition moment of porphyrins and phthalocyanines lies in the plane of the molecules [188] and coincides with the N-Cu-N axis of CuPc.[189] Considering this transition dipole moment and the observed molecular orientations, we would therefore expect a 77% increase in absorption coefficient for CuPc on GMG compared with on bare glass, which is consistent with the experimentally observed increase of 63%, 51% and 86% at 620 nm, 664 nm and 700 nm respectively. A 77% increase in optical absorptivity should result in a 45 % decrease in L_A.

At the same time, we expect the exciton diffusion length (L_D) to be improved by using graphene to template CuPc in the “lying-down” morphology. It has been both theoretically [159] and experimentally [160] shown that L_D is strongly affected by crystallinity and molecular ordering. Singlet exciton diffusion mainly occurs via Förster energy transfer by dipole-dipole coupling between neighboring molecules (namely the donor and the acceptor).[190] The coupling depends on: (a) the angle between the transition dipole moments of the donor and acceptor, (b) the fluorescence quantum yield of the donor and (c) the spectral/energy overlap between the emissivity of the donor and the absorptivity of the acceptor. Disorder is known to decrease L_D

due to inter-molecular misalignment, reduced fluorescence quantum yield, and decreased spectral overlap due to energetic disorder resulting from local heterogeneity. Athanasopoulos et al. have recently employed Monte Carlo non-equilibrium hopping models to shown that L_D can indeed decrease by more than an order of magnitude as a result of energetic and molecular disorder.[159] Furthermore, it has been experimentally demonstrated in other molecular systems such as PTCDA, that L_D can increase up to four times by increasing the spatial extent of crystalline order.[160] Future work will be needed to quantify the L_D of the ordered and oriented CuPc films realized here. However, similar gains in L_D are expected.

A single monolayer of graphene that is < 0.5 nm in thickness, > 95% transparent and highly conductive was used as a template to control and modify the orientation of CuPc films of 80-320 nm in thickness, on both oxide and metal substrates. Specifically, the lateral CuPc crystal size increased from 38nm to >125nm by functionalizing bare glass and copper surfaces with graphene. The CuPc was oriented in the (100) crystallographic direction on the bare substrates, corresponding to a “standing-up” molecular orientation, whereas the CuPc was oriented in the (11-2) and (01-2) directions on the graphene modified substrates, corresponding to a nearly “lying-down” conformation of the molecules on the substrate, in which the molecules form stacked columns. This “lying-down” conformation is expected to be ideal for planar and planar nanostructured OPV solar cells. We have shown already that the absorption coefficient of the CuPc films is increased by 86% at 700 nm by templating the films using graphene. Further enhancements in exciton diffusion length and charge transport mobility are expected.

We anticipate that the strategy presented here for templating CuPc on graphene will be extendable to many other semiconducting molecules which have aromatic bases. Furthermore, recent advances in the scalable synthesis of graphene via chemical vapor deposition beyond the

3000 cm^2 scale[77] should ultimately make it possible to integrate single monolayers of graphene over large area substrates of glass, plastic, or metal. Thus this method is expected to serve as a foundation for developing future, OLEDs and OPVs with improved performance.

Acknowledgement

This work was supported by National Science Foundation (Grant# CBET-1033346). MSA also acknowledges partial support from a 3M Non-Tenured Faculty Grant.

7. Summary and Outlook

We have demonstrate significant advances in the fundamental understanding and engineering of scalable graphene diffusion barriers. Previous experimental studies have established that defect-free non-scalable graphene is an excellent barrier material, however its scalable counterparts are still well behind in terms of performance. Studies by our group and others have shown that the latter's ability to perform as a barrier membrane is compromised primarily by the presence of three major problems - (i) high density of defects, (ii) self-degradation in ambient environment and (iii) induced electrochemical oxidation of the underlying material. We have developed an in-depth understanding of how diffusion occurs through monolayer graphene grown via chemical vapor deposition. It is observed that the atomic membrane is impenetrable in the pristine regions, however it is easily penetrated by oxygen and water at grain boundaries and other intrinsic defects like nanopores. To understand and address problem (ii), we studied in detail the self-deterioration of graphene in ambient and quantify the evolution, kinetics, and energetics of the degradation process both in the pristine and intrinsically defective regions of graphene. We also found that the degradation process is accelerated in the presence of water vapor. The overall defect density of a graphene membrane is primarily determined by the density of its intrinsic nanopores and grain boundaries. In order to tackle problem (i), we demonstrated that the density on intrinsic nanopores can be significantly reduced by reducing the surface roughness of the growth substrate which is achieved by regulating the pre-growth annealing time and temperature. Also, the density of the grain boundaries can be altered by varying the internucleation distance during the growth of the membrane. For using graphene is used as a corrosion barrier for metals and preventing problem (iii), we established that the electrochemical corrosion of the metal is drastically reduced by adding an ultra-thin electrically insulating layer between the graphene and the metal. In addition, the barrier performance is enhanced greatly by stacking more layers of graphene top of the first layer. Finally, we combined all we learnt and developed from these previous studies and design high performance scalable graphene barriers and the best until date. We expect this study to serve as a foundation for engineering next-generation graphene barriers with performance comparable to its pristine and theoretical counterparts. There are several opportunities to extend this work and realize near-theoretical graphene barriers. A few research directions to address each of three major problems are listed, below:

7.1 Reducing defects

Defects are a major cause of concern in all forms of graphene manufactured through scalable methods and has been the primary focus of a lot of research groups around the world, including ours. Presence of defects in the form of holes, pores, grain boundaries, contaminants and tears from transfer etc. can fatally affect the properties of graphene as observed in this study. However, there are several approaches through which the defect density can be minimized. In particular, for graphene grown via CVD, an atomistically flat substrate, free from irregularities can eliminate the presence of nanopores or holes in the graphene layer. More research need to be done on developing such substrates that are scalable. Similarly, work needs to be done to develop better techniques to transfer large area graphene with introducing additional tears, holes, wrinkles or contaminants. Methods to obtain high internucleation distance to reduce the grain boundary density are also critical for manufacturing high quality graphene layers.

7.2 Reducing degradation in ambient

Degradation of graphene is also a problem for applications of graphene involving ambient atmosphere, especially at slightly elevated temperatures. We have demonstrated that the presence of water vapor in the atmosphere can be particularly devastating for the graphene's oxidative stability. One way to minimize this damage is by adding a hydrophobic layer to protect the atomic membrane. We saw the proof-of-principle demonstration of this approach in the stacked graphene layer approach in chapters 2 and 5, where the underlying layer of graphene was protected by the graphene layer(s) on the top of the stack resulting in a superior barrier performance. Substrate induced defects are also a major cause of concern for a lot of applications of graphene involving polar or rough substrates. It is essential that the graphene is de-coupled from the surface roughness and charge-inhomogeneity of the underlying substrate to improve its oxidative stability in ambient. More research needs pursued to identify substrates that can be used to reduce these effects.

7.3 Reducing electrochemical corrosion

For using graphene as a corrosion protecting layer for refined metals like copper. It is essential to completely eliminate electrical contact between the two. In this study, we have demonstrated as a proof-of-principle that ultra-thin Al_2O_3 layers can be used for the above purpose. It can be hypothesized that polymers that are electrically insulating and thermally stable can be used to insulate the graphene layer from the underlying metal. The use of polymers can also expand the reach of graphene based barriers to flexible and stretchable applications which are currently unattainable due to the presence of a brittle Al_2O_3 layer.

Designing barriers with superior performance closer to its theoretical limits has its utility in several demanding application which currently possess either no technology or very expensive ones, for example encapsulation of organic semiconductor based devices, membranes for water desalination and gas separation, controlled drug delivery etc. Overcoming the above listed problems can establish graphene as a material for next generation diffusion barrier.

Bibliography:

1. Cooper, D. R.; D'Anjou, B.; Ghattamaneni, N.; Harack, B.; Hilke, M.; Horth, A.; Majlis, N.; Massicotte, M.; Vandsburger, L.; Whiteway, E.; Yu, V., Experimental Review of Graphene. *ISRN Condensed Matter Physics* **2012**, 501686 (56 pp.)-501686 (56 pp.).

2. Geim, A. K., Graphene: Status and Prospects. *Science* **2009,** 324, (5934), 1530-1534.

3. Geim, A. K.; Novoselov, K. S., The rise of graphene. *Nature Materials* **2007,** 6, (3), 183-191.

4. Castro Neto, A. H.; Guinea, F.; Peres, N. M. R.; Novoselov, K. S.; Geim, A. K., The electronic properties of graphene. *Reviews of Modern Physics* **2009,** 81, (1), 109-162.

5. Novoselov, K. S.; Geim, A. K.; Morozov, S. V.; Jiang, D.; Zhang, Y.; Dubonos, S. V.; Grigorieva, I. V.; Firsov, A. A., Electric field effect in atomically thin carbon films. *Science* **2004,** 306, (5696), 666-669.

6. Butler, S. Z.; Hollen, S. M.; Cao, L.; Cui, Y.; Gupta, J. A.; Gutierrez, H. R.; Heinz, T. F.; Hong, S. S.; Huang, J.; Ismach, A. F.; Johnston-Halperin, E.; Kuno, M.; Plashnitsa, V. V.; Robinson, R. D.; Ruoff, R. S.; Salahuddin, S.; Shan, J.; Shi, L.; Spencer, M. G.; Terrones, M.; Windl, W.; Goldberger, J. E., Progress, Challenges, and Opportunities in Two-Dimensional Materials Beyond Graphene. *Acs Nano* **2013,** 7, (4), 2898-2926.

7. Geim, A. K.; Grigorieva, I. V., Van der Waals heterostructures. *Nature* **2013,** 499, (7459), 419-425.

8. Akturk, A.; Goldsman, N., Electron transport and full-band electron-phonon interactions in graphene. *Journal of Applied Physics* **2008,** 103, (5).

9. Chen, J.-H.; Jang, C.; Xiao, S.; Ishigami, M.; Fuhrer, M. S., Intrinsic and extrinsic performance limits of graphene devices on SiO2. *Nature Nanotechnology* **2008,** 3, (4), 206-209.

10. Han, M. Y.; Oezyilmaz, B.; Zhang, Y.; Kim, P., Energy band-gap engineering of graphene nanoribbons. *Physical Review Letters* **2007,** 98, (20).

11. Son, Y.-W.; Cohen, M. L.; Louie, S. G., Energy gaps in graphene nanoribbons. *Physical Review Letters* **2006,** 97, (21).

12. Baringhaus, J.; Ruan, M.; Edler, F.; Tejeda, A.; Sicot, M.; Taleb-Ibrahimi, A.; Li, A.-P.; Jiang, Z.; Conrad, E. H.; Berger, C.; Tegenkamp, C.; de Heer, W. A., Exceptional ballistic transport in epitaxial graphene nanoribbons. *Nature* **2014,** 506, (7488), 349-354.

13. Kim, M.; Safron, N. S.; Han, E.; Arnold, M. S.; Gopalan, P., Electronic Transport and Raman Scattering in Size-Controlled Nanoperforated Graphene. *Acs Nano* **2012,** 6, (11), 9846-9854.

14. De Arco, L. G.; Zhang, Y.; Schlenker, C. W.; Ryu, K.; Thompson, M. E.; Zhou, C., Continuous, Highly Flexible, and Transparent Graphene Films by Chemical Vapor Deposition for Organic Photovoltaics. *Acs Nano* **2010,** 4, (5), 2865-2873.

15. Park, H.; Brown, P. R.; Buloyic, V.; Kong, J., Graphene As Transparent Conducting Electrodes in Organic Photovoltaics: Studies in Graphene Morphology, Hole Transporting Layers, and Counter Electrodes. *Nano Letters* **2012,** 12, (1), 133-140.

16. Pang, S. P.; Hernandez, Y.; Feng, X. L.; Mullen, K., Graphene as Transparent Electrode Material for Organic Electronics. *Advanced Materials* **2011,** 23, (25), 2779-2795.

17. Matyba, P.; Yamaguchi, H.; Chhowalla, M.; Robinson, N. D.; Edman, L., Flexible and Metal-Free Light-Emitting Electrochemical Cells Based on Graphene and PEDOT-PSS as the Electrode Materials. *Acs Nano* **2011,** 5, (1), 574-580.

18. Wu, J.; Agrawal, M.; Becerril, H. A.; Bao, Z.; Liu, Z.; Chen, Y.; Peumans, P., Organic Light-Emitting Diodes on Solution-Processed Graphene Transparent Electrodes. *Acs Nano* **2010,** 4, (1), 43-48.

19. Han, T.-H.; Lee, Y.; Choi, M.-R.; Woo, S.-H.; Bae, S.-H.; Hong, B. H.; Ahn, J.-H.; Lee, T.-W., Extremely efficient flexible organic light-emitting diodes with modified graphene anode. *Nature Photonics* **2012,** 6, (2), 105-110.

20. Lee, C.; Wei, X.; Kysar, J. W.; Hone, J., Measurement of the elastic properties and intrinsic strength of monolayer graphene. *Science* **2008,** 321, (5887), 385-388.

21. O'Hern, S. C.; Boutilier, M. S. H.; Idrobo, J.-C.; Song, Y.; Kong, J.; Laoui, T.; Atieh, M.; Karnik, R., Selective Ionic Transport through Tunable Subnanometer Pores in Single-Layer Graphene Membranes. *Nano Letters* **2014,** 14, (3), 1234-1241.

22. Koenig, S. P.; Wang, L.; Pellegrino, J.; Bunch, J. S., Selective molecular sieving through porous graphene. *Nature Nanotechnology* **2012,** 7, (11), 728-732.

23. O'Hern, S. C.; Stewart, C. A.; Boutilier, M. S. H.; Idrobo, J.-C.; Bhaviripudi, S.; Das, S. K.; Kong, J.; Laoui, T.; Atieh, M.; Karnik, R., Selective Molecular Transport through Intrinsic Defects in a Single Layer of CVD Graphene. *Acs Nano* **2012,** 6, (11), 10130-10138.

24. Boutilier, M. S. H.; Sun, C.; O'Hern, S. C.; Au, H.; Hadjiconstantinou, N. G.; Karnik, R., Implications of Permeation through Intrinsic Defects in Graphene on the Design of Defect-Tolerant Membranes for Gas Separation. *Acs Nano* **2014,** 8, (1), 841-849.

25. Jiang, D.-e.; Cooper, V. R.; Dai, S., Porous Graphene as the Ultimate Membrane for Gas Separation. *Nano Letters* **2009,** 9, (12), 4019-4024.

26. Kim, K. S.; Zhao, Y.; Jang, H.; Lee, S. Y.; Kim, J. M.; Kim, K. S.; Ahn, J.-H.; Kim, P.; Choi, J.-Y.; Hong, B. H., Large-scale pattern growth of graphene films for stretchable transparent electrodes. *Nature* **2009,** 457, (7230), 706-710.

27. Bae, S.; Kim, H.; Lee, Y.; Xu, X. F.; Park, J. S.; Zheng, Y.; Balakrishnan, J.; Lei, T.; Kim, H. R.; Song, Y. I.; Kim, Y. J.; Kim, K. S.; Ozyilmaz, B.; Ahn, J. H.; Hong, B. H.; Iijima, S., Roll-to-roll production of 30-inch graphene films for transparent electrodes. *Nature Nanotechnology* **2010,** 5, (8), 574-578.

28. Balandin, A. A.; Ghosh, S.; Bao, W.; Calizo, I.; Teweldebrhan, D.; Miao, F.; Lau, C. N., Superior thermal conductivity of single-layer graphene. *Nano Letters* **2008,** 8, (3), 902-907.

29. Zacharia, R.; Ulbricht, H.; Hertel, T., Interlayer cohesive energy of graphite from thermal desorption of polyaromatic hydrocarbons. *Physical Review B* **2004,** 69, (15).

30. Chupka, W. A.; Inghram, M. G., Direct determination of the heat of sublimation of carbon with the mass spectrometer. *Journal of Physical Chemistry* **1955,** 59, (2), 100-104.

31. Kim, K.; Regan, W.; Geng, B.; Aleman, B.; Kessler, B. M.; Wang, F.; Crommie, M. F.; Zettl, A., High-temperature stability of suspended single-layer graphene. *Physica Status Solidi-Rapid Research Letters* **2010,** 4, (11).

32. Lin, Y.-C.; Jin, C.; Lee, J.-C.; Jen, S.-F.; Suenaga, K.; Chiu, P.-W., Clean Transfer of Graphene for Isolation and Suspension. *Acs Nano* **2011,** 5, (3), 2362-2368.

33. Suk, J. W.; Kitt, A.; Magnuson, C. W.; Hao, Y.; Ahmed, S.; An, J.; Swan, A. K.; Goldberg, B. B.; Ruoff, R. S., Transfer of CVD-Grown Monolayer Graphene onto Arbitrary Substrates. *Acs Nano* **2011,** 5, (9).

34. Li, X.; Zhu, Y.; Cai, W.; Borysiak, M.; Han, B.; Chen, D.; Piner, R. D.; Colombo, L.; Ruoff, R. S., Transfer of Large-Area Graphene Films for High-Performance Transparent Conductive Electrodes. *Nano Letters* **2009,** 9, (12).

35. Bunch, J. S.; Verbridge, S. S.; Alden, J. S.; van der Zande, A. M.; Parpia, J. M.; Craighead, H. G.; McEuen, P. L., Impermeable atomic membranes from graphene sheets. *Nano Letters* **2008,** 8, (8), 2458-2462.

36. Nguyen, B.-S.; Lin, J.-F.; Perng, D.-C., 1-nm-thick graphene tri-layer as the ultimate copper diffusion barrier. *Applied Physics Letters* **2014,** 104, (8).

37. Hong, J.; Lee, S.; Lee, S.; Han, H.; Mahata, C.; Yeon, H.-W.; Koo, B.; Kim, S.-I.; Nam, T.; Byun, K.; Min, B.-W.; Kim, Y.-W.; Kim, H.; Joo, Y.-C.; Lee, T., Graphene as an atomically thin barrier to Cu diffusion into Si. *Nanoscale* **2014,** 6, (13), 7503-7511.

38. Stoeberl, U.; Wurstbauer, U.; Wegscheider, W.; Weiss, D.; Eroms, J., Morphology and flexibility of graphene and few-layer graphene on various substrates. *Applied Physics Letters* **2008,** 93, (5).

39. Vosgueritchian, M.; Lipomi, D. J.; Bao, Z., Highly Conductive and Transparent PEDOT:PSS Films with a Fluorosurfactant for Stretchable and Flexible Transparent Electrodes. *Advanced Functional Materials* **2012,** 22, (2), 421-428.

40. Kang, J.; Shin, D.; Bae, S.; Hong, B. H., Graphene transfer: key for applications. *Nanoscale* **2012,** 4, (18), 5527-5537.

41. Zhu, Y.; Murali, S.; Cai, W.; Li, X.; Suk, J. W.; Potts, J. R.; Ruoff, R. S., Graphene and Graphene Oxide: Synthesis, Properties, and Applications. *Advanced Materials* **2010,** 22, (35), 3906-3924.

42. de Heer, W. A.; Berger, C.; Wu, X. S.; First, P. N.; Conrad, E. H.; Li, X. B.; Li, T. B.; Sprinkle, M.; Hass, J.; Sadowski, M. L.; Potemski, M.; Martinez, G., Epitaxial graphene. *Solid State Communications* **2007,** 143, (1-2), 92-100.

43. Mao, H. Y.; Wang, R.; Wang, Y.; Niu, T. C.; Zhong, J. Q.; Huang, M. Y.; Qi, D. C.; Loh, K. P.; Wee, A. T. S.; Chen, W., Chemical vapor deposition graphene as structural template to control interfacial molecular orientation of chloroaluminium phthalocyanine. *Applied Physics Letters* **2011,** 99, (9).

44. Dhingra, S.; Hsu, J. F.; Vlassiouk, I.; D'Urso, B., Chemical vapor deposition of graphene on large-domain ultra-flat copper. *Carbon* **2014,** 69, 188-193.

45. Wood, J. D.; Schmucker, S. W.; Lyons, A. S.; Pop, E.; Lyding, J. W., Effects of Polycrystalline Cu Substrate on Graphene Growth by Chemical Vapor Deposition. *Nano Letters* **2011,** 11, (11), 4547-4554.

46. Jauregui, L. A.; Cao, H.; Wu, W.; Yu, Q.; Chen, Y. P., Electronic properties of grains and grain boundaries in graphene grown by chemical vapor deposition. *Solid State Communications* **2011,** 151, (16).

47. Suk, J. W.; Lee, W. H.; Lee, J.; Chou, H.; Piner, R. D.; Hao, Y.; Akinwande, D.; Ruoff, R. S., Enhancement of the Electrical Properties of Graphene Grown by Chemical Vapor Deposition via Controlling the Effects of Polymer Residue. *Nano Letters* **2013,** 13, (4), 1462-1467.

48. Kim, K.; Lee, Z.; Regan, W.; Kisielowski, C.; Crommie, M. F.; Zettl, A., Grain Boundary Mapping in Polycrystalline Graphene. *Acs Nano* **2011,** 5, (3), 2142-2146.

49. Li, X. S.; Magnuson, C. W.; Venugopal, A.; An, J. H.; Suk, J. W.; Han, B. Y.; Borysiak, M.; Cai, W. W.; Velamakanni, A.; Zhu, Y. W.; Fu, L. F.; Vogel, E. M.; Voelkl, E.; Colombo, L.; Ruoff, R.

S., Graphene Films with Large Domain Size by a Two-Step Chemical Vapor Deposition Process. *Nano Letters* **2010,** 10, (11), 4328-4334.

50. Xing, S. R.; Wu, W.; Wang, Y. A.; Bao, J. M.; Pei, S. S., Kinetic study of graphene growth: Temperature perspective on growth rate and film thickness by chemical vapor deposition. *Chemical Physics Letters* **2013,** 580, 62-66.

51. Surwade, S. P.; Li, Z.; Liu, H., Thermal Oxidation and Unwrinkling of Chemical Vapor Deposition-Grown Graphene. In The Journal of Physical Chemistry C: 2012.

52. Tao, L.; Lee, J.; Holt, M.; Chou, H.; McDonnell, S. J.; Ferrer, D. A.; Babenco, M. G.; Wallace, R. M.; Banerjee, S. K.; Ruoff, R. S.; Akinwande, D., Uniform Wafer-Scale Chemical Vapor Deposition of Graphene on Evaporated Cu (111) Film with Quality Comparable to Exfoliated Monolayer. *Journal of Physical Chemistry C* **2012,** 116, (45).

53. Li, X. S.; Cai, W. W.; An, J. H.; Kim, S.; Nah, J.; Yang, D. X.; Piner, R.; Velamakanni, A.; Jung, I.; Tutuc, E.; Banerjee, S. K.; Colombo, L.; Ruoff, R. S., Large-Area Synthesis of High-Quality and Uniform Graphene Films on Copper Foils. *Science* **2009,** 324, (5932), 1312-1314.

54. Loginova, E.; Bartelt, N. C.; Feibelman, P. J.; McCarty, K. F., Factors influencing graphene growth on metal surfaces. *New Journal of Physics* **2009,** 11.

55. Roy, S. S.; Safron, N. S.; Wu, M. Y.; Arnold, M. S., Evolution, kinetics, energetics, and environmental factors of graphene degradation on silicon dioxide. *Nanoscale* **2015,** 7, (14), 6093-6103.

56. Childres, I.; Jauregui, L. A.; Tian, J.; Chen, Y. P., Effect of oxygen plasma etching on graphene studied using Raman spectroscopy and electronic transport measurements. *New Journal of Physics* **2011,** 13.

57. Jones, J. D.; Morris, C. F.; Verbeck, G. F.; Perez, J. M., Oxidative pit formation in pristine, hydrogenated and dehydrogenated graphene. *Applied Surface Science* **2013,** 264, 853-863.

58. Kim, D. C.; Jeon, D.-Y.; Chung, H.-J.; Woo, Y.; Shin, J. K.; Seo, S., The structural and electrical evolution of graphene by oxygen plasma-induced disorder. *Nanotechnology* **2009,** 20, (37).

59. Koizumi, K.; Boero, M.; Shigeta, Y.; Oshiyama, A., Atom-Scale Reaction Pathways and Free-Energy Landscapes in Oxygen Plasma Etching of Graphene. *Journal of Physical Chemistry Letters* **2013,** 4, (10), 1592-1596.

60. Liu, L.; Xie, D.; Wu, M.; Yang, X.; Xu, Z.; Wang, W.; Bai, X.; Wang, E., Controlled oxidative functionalization of monolayer graphene by water-vapor plasma etching. *Carbon* **2012,** 50, (8), 3039-3044.

61. Brady, G.; Jacobberger, R.; Roy, S. S.; Wall, M.; Arnold, M., Raman Imaging as a Tool for Characterizing Carbon Nanomaterials. *American Laboratory* **2014,** 46, (3), 12-15.

62. Dresselhaus, M. S.; Dresselhaus, G.; Saito, R.; Jorio, A., Raman spectroscopy of carbon nanotubes. *Physics Reports-Review Section of Physics Letters* **2005,** 409, (2), 47-99.

63. Cancado, L. G.; Jorio, A.; Martins Ferreira, E. H.; Stavale, F.; Achete, C. A.; Capaz, R. B.; Moutinho, M. V. O.; Lombardo, A.; Kulmala, T. S.; Ferrari, A. C., Quantifying Defects in Graphene via Raman Spectroscopy at Different Excitation Energies. *Nano Letters* **2011,** 11, (8), 3190-3196.

64. Ferrari, A. C., Raman spectroscopy of graphene and graphite: Disorder, electron-phonon coupling, doping and nonadiabatic effects. *Solid State Communications* **2007,** 143, (1-2), 47-57.

65. Havener, R. W.; Zhuang, H.; Brown, L.; Hennig, R. G.; Park, J., Angle-Resolved Raman Imaging of Inter layer Rotations and Interactions in Twisted Bilayer Graphene. *Nano Letters* **2012,** 12, (6).

66. Ni, Z. H.; Ponomarenko, L. A.; Nair, R. R.; Yang, R.; Anissimova, S.; Grigorieva, I. V.; Schedin, F.; Blake, P.; Shen, Z. X.; Hill, E. H.; Novoselov, K. S.; Geim, A. K., On Resonant Scatterers As a Factor Limiting Carrier Mobility in Graphene. *Nano Letters* **2010,** 10, (10), 3868-3872.

67. Shivaraman, S.; Chandrashekhar, M. V. S.; Boeckl, J. J.; Spencer, M. G., Thickness Estimation of Epitaxial Graphene on SiC Using Attenuation of Substrate Raman Intensity. *Journal of Electronic Materials* **2009,** 38, (6), 725-730.

68. Xu, Y. N.; Zhan, D.; Liu, L.; Suo, H.; Ni, Z. H.; Thuong, T. N.; Zhao, C.; Shen, Z. X., Thermal Dynamics of Graphene Edges Investigated by Polarized Raman Spectroscopy. *Acs Nano* **2011,** 5, (1), 147-152.

69. Zhou, H.; Qiu, C.; Yu, F.; Yang, H.; Chen, M.; Hu, L.; Guo, Y.; Sun, L., Raman scattering of monolayer graphene: the temperature and oxygen doping effects. *Journal of Physics D-Applied Physics* **2011,** 44, (18).

70. Singha Roy, S.; Arnold, M., Improving Graphene Diffusion Barriers via Stacking Multiple Layers and Grain Size Engineering. *Advanced Functional Materials* **2013,** 23, (29), 3638-3644.

71. Malard, L. M.; Pimenta, M. A.; Dresselhaus, G.; Dresselhaus, M. S., Raman spectroscopy in graphene. *Physics Reports-Review Section of Physics Letters* **2009,** 473, (5-6), 51-87.

72. Das, A.; Chakraborty, B.; Sood, A. K., Raman spectroscopy of graphene on different substrates and influence of defects. *Bulletin of Materials Science* **2008,** 31, (3), 579-584.

73. Eckmann, A.; Felten, A.; Verzhbitskiy, I.; Davey, R.; Casiraghi, C., Raman study on defective graphene: Effect of the excitation energy, type, and amount of defects. *Physical Review B* **2013,** 88, (3).

74. Ferrari, A. C.; Meyer, J. C.; Scardaci, V.; Casiraghi, C.; Lazzeri, M.; Mauri, F.; Piscanec, S.; Jiang, D.; Novoselov, K. S.; Roth, S.; Geim, A. K., Raman spectrum of graphene and graphene layers. *Physical Review Letters* **2006,** 97, (18).

75. Graf, D.; Molitor, F.; Ensslin, K.; Stampfer, C.; Jungen, A.; Hierold, C.; Wirtz, L., Raman mapping of a single-layer to double-layer graphene transition. *European Physical Journal-Special Topics* **2007,** 148.

76. Blake, P.; Brimicombe, P. D.; Nair, R. R.; Booth, T. J.; Jiang, D.; Schedin, F.; Ponomarenko, L. A.; Morozov, S. V.; Gleeson, H. F.; Hill, E. W.; Geim, A. K.; Novoselov, K. S., Graphene-based liquid crystal device. *Nano Letters* **2008,** 8, (6), 1704-1708.

77. Bae, S.; Kim, H.; Lee, Y.; Xu, X.; Park, J.-S.; Zheng, Y.; Balakrishnan, J.; Lei, T.; Ri Kim, H.; Song, Y. I.; Kim, Y.-J.; Kim, K. S.; Ozyilmaz, B.; Ahn, J.-H.; Hong, B. H.; Iijima, S., Roll-to-roll production of 30-inch graphene films for transparent electrodes. *Nat Nano* 5, (8), 574-578.

78. Bi, H.; Huang, F.; Liang, J.; Xie, X.; Jiang, M., Transparent Conductive Graphene Films Synthesized by Ambient Pressure Chemical Vapor Deposition Used as the Front Electrode of CdTe Solar Cells. *Advanced materials (Deerfield Beach, Fla.)* **2011,** 23, (28), 3202-6.

79. Wang, X.; Zhi, L. J.; Mullen, K., Transparent, conductive graphene electrodes for dye-sensitized solar cells. *Nano Letters* **2008,** 8, (1), 323-327.

80. Regmi, M.; Chisholm, M. F.; Eres, G., The effect of growth parameters on the intrinsic properties of large-area single layer graphene grown by chemical vapor deposition on Cu. *Carbon* **2012,** 50, (1).

81. Compton, O. C.; Kim, S.; Pierre, C.; Torkelson, J. M.; Nguyen, S. T., Crumpled Graphene Nanosheets as Highly Effective Barrier Property Enhancers. *Advanced Materials* **2010,** 22, (42), 4759-+.

82. Chen, S.; Brown, L.; Levendorf, M.; Cai, W.; Ju, S.-Y.; Edgeworth, J.; Li, X.; Magnuson, C. W.; Velamakanni, A.; Piner, R. D.; Kang, J.; Park, J.; Ruoff, R. S., Oxidation Resistance of Graphene-Coated Cu and Cu/Ni Alloy. *Acs Nano* **2011,** 5, (2).

83. Yu, L.; Lim, Y.-S.; Han, J. H.; Kim, K.; Kim, J. Y.; Choi, S.-Y.; Shin, K., A graphene oxide oxygen barrier film deposited via a self-assembly coating method. *Synthetic Metals* **2012,** 162, (7-8).

84. Kirkland, N. T.; Schiller, T.; Medhekar, N.; Birbilis, N., Exploring graphene as a corrosion protection barrier. *Corrosion Science* **2012,** 56, 1-4.

85. Prasai, D.; Tuberquia, J. C.; Harl, R. R.; Jennings, G. K.; Bolotin, K. I., Graphene: Corrosion-Inhibiting Coating. *Acs Nano* **2012,** 6, (2).

86. Zhou, F.; Li, Z.; Shenoy, G. J.; Li, L.; Liu, H., Enhanced Room-Temperature Corrosion of Copper in the Presence of Graphene. *Acs Nano* **2013,** 7, (8), 6939-6947.

87. Schriver, M.; Regan, W.; Gannett, W. J.; Zaniewski, A. M.; Crommie, M. F.; Zettl, A., Graphene as a Long-Term Metal Oxidation Barrier: Worse Than Nothing. *Acs Nano* **2013,** 7, (7), 5763-5768.

88. Wei, Y. J.; Wu, J. T.; Yin, H. Q.; Shi, X. H.; Yang, R. G.; Dresselhaus, M., The nature of strength enhancement and weakening by pentagon-heptagon defects in graphene. *Nature Materials* **2012,** 11, (9), 759-763.

89. Surwade, S. P.; Li, Z. T.; Liu, H. T., Thermal Oxidation and Unwrinkling of Chemical Vapor Deposition-Grown Graphene. *Journal of Physical Chemistry C* **2012,** 116, (38), 20600-20606.

90. Cohen-Tanugi, D.; Grossman, J. C., Water Desalination across Nanoporous Graphene. *Nano Letters* **2012,** 12, (7), 3602-3608.

91. Roy, S. S.; Bindl, D. J.; Arnold, M. S., Templating Highly Crystalline Organic Semiconductors Using Atomic Membranes of Graphene at the Anode/Organic Interface. *Journal of Physical Chemistry Letters* **2012,** 3, (7).

92. Berger, C.; Song, Z. M.; Li, T. B.; Li, X. B.; Ogbazghi, A. Y.; Feng, R.; Dai, Z. T.; Marchenkov, A. N.; Conrad, E. H.; First, P. N.; de Heer, W. A., Ultrathin epitaxial graphite: 2D electron gas properties and a route toward graphene-based nanoelectronics. *Journal of Physical Chemistry B* **2004,** 108, (52), 19912-19916.

93. Reina, A.; Jia, X. T.; Ho, J.; Nezich, D.; Son, H. B.; Bulovic, V.; Dresselhaus, M. S.; Kong, J., Large Area, Few-Layer Graphene Films on Arbitrary Substrates by Chemical Vapor Deposition. *Nano Letters* **2009,** 9, (1), 30-35.

94. Topsakal, M.; Sahin, H.; Ciraci, S., Graphene coatings: An efficient protection from oxidation. *Physical Review B* **2012,** 85, (15).

95. Kang, D.; Kwon, J. Y.; Cho, H.; Sim, J.-H.; Hwang, H. S.; Kim, C. S.; Kim, Y. J.; Ruoff, R. S.; Shin, H. S., Oxidation Resistance of Iron and Copper Foils Coated with Reduced Graphene Oxide Multilayers. In ACS Nano, 2012.

96. Lange, P.; Dorn, M.; Severin, N.; Vanden Bout, D. A.; Rabe, J. P., Single- and Double-Layer Graphenes as Ultrabarriers for Fluorescent Polymer Films. *Journal of Physical Chemistry C* **2011,** 115, (46), 23057-23061.

97. Murray, I. P.; Lou, S. J.; Cote, L. J.; Loser, S.; Kadleck, C. J.; Xu, T.; Szarko, J. M.; Rolczynski, B. S.; Johns, J. E.; Huang, J. X.; Yu, L. P.; Chen, L. X.; Marks, T. J.; Hersam, M. C., Graphene Oxide Inter layers for Robust, High-Efficiency Organic Photovoltaics. *Journal of Physical Chemistry Letters* **2011,** 2, (24), 3006-3012.

98. Lee, B.-J.; Jeong, G.-H., Thermal Oxidation of Synthesized Graphenes and Their Optical Property Characterization. *Journal of Nanoscience and Nanotechnology* **2011,** 11, (7).

99. Surwade, S. P.; Li, Z.; Liu, H., Thermal Oxidation and Unwrinkling of Chemical Vapor Deposition-Grown Graphene. *The Journal of Physical Chemistry C* **2012,** 116, (38), 20600-20606.

100. Xu, S. C.; Irle, S.; Musaev, D. G.; Lin, M. C., Quantum chemical study of the dissociative adsorption of OH and H2O on pristine and defective graphite (0001) surfaces: Reaction mechanisms and kinetics. *Journal of Physical Chemistry C* **2007,** 111, (3).

101. Duong, D. L. H., Gang Hee Lee, Seung Mi Gunes, Fethullah Kim, Eun Sung Kim, Sung Tae Kim, Heetae Ta, Quang Huy So, Kang Pyo Yoon, Seok Jun Chae, Seung Jin Jo, Young Woo Park, Min Ho Chae, Sang Hoon Lim, Seong Chu Choi, Jae Young Lee, Young Hee, Probing graphene grain boundaries with optical microscopy. In Nature: 2012/10/03/online; Vol. advance online publication.

102. Safron, N. S.; Kim, M.; Gopalan, P.; Arnold, M. S., Barrier-Guided Growth of Micro- and Nano-Structured Graphene. *Advanced Materials* **2012,** 24, (8).

103. Niaura, G., Surface-enhanced Raman spectroscopic observation of two kinds of adsorbed OH- ions at copper electrode. *Electrochimica Acta* **2000,** 45, (21).

104. Graf, D.; Molitor, F.; Ensslin, K.; Stampfer, C.; Jungen, A.; Hierold, C.; Wirtz, L., Spatially resolved raman spectroscopy of single- and few-layer graphene. *Nano Letters* **2007,** 7, (2), 238-242.

105. Mayer, S. T.; Muller, R. H., AN INSITU RAMAN-SPECTROSCOPY STUDY OF THE ANODIC-OXIDATION OF COPPER IN ALKALINE MEDIA. *Journal of the Electrochemical Society* **1992,** 139, (2), 426-434.

106. Kim, K.; Coh, S.; Tan, L. Z.; Regan, W.; Yuk, J. M.; Chatterjee, E.; Crommie, M. F.; Cohen, M. L.; Louie, S. G.; Zettl, A., Raman Spectroscopy Study of Rotated Double-Layer Graphene: Misorientation-Angle Dependence of Electronic Structure. *Physical Review Letters* **2012,** 108, (24).

107. Robinson, J.; Schmucker, S.; Diaconescu, B.; Long, J.; Culbertson, J.; Ohta, T.; Friedman, A.; Beechem, T., Electronic Hybridization of Large-Area Stacked Graphene Films. In ACS Nano, 2012; Vol. advanced online publication.

108. Liu, L.; Ryu, S.; Tomasik, M. R.; Stolyarova, E.; Jung, N.; Hybertsen, M. S.; Steigerwald, M. L.; Brus, L. E.; Flynn, G. W., Graphene oxidation: Thickness-dependent etching and strong chemical doping. *Nano Letters* **2008,** 8, (7).

109. Ryu, S.; Liu, L.; Berciaud, S.; Yu, Y. J.; Liu, H. T.; Kim, P.; Flynn, G. W.; Brus, L. E., Atmospheric Oxygen Binding and Hole Doping in Deformed Graphene on a SiO2 Substrate. *Nano Letters* **2010,** 10, (12), 4944-4951.

110. Romero, H. E.; Shen, N.; Joshi, P.; Gutierrez, H. R.; Tadigadapa, S. A.; Sofo, J. O.; Eklund, P. C., n-Type Behavior of Graphene Supported on Si/SiO2 Substrates. *Acs Nano* **2008,** 2, (10), 2037-2044.

111. Di, C. A.; Wei, D. C.; Yu, G.; Liu, Y. Q.; Guo, Y. L.; Zhu, D. B., Patterned graphene as source/drain electrodes for bottom-contact organic field-effect transistors. *Advanced Materials* **2008,** 20, (17), 3289-+.

112. Cheng, Z. G.; Zhou, Q. Y.; Wang, C. X.; Li, Q. A.; Wang, C.; Fang, Y., Toward Intrinsic Graphene Surfaces: A Systematic Study on Thermal Annealing and Wet-Chemical Treatment of SiO2-Supported Graphene Devices. *Nano Letters* **2011,** 11, (2), 767-771.

113. Xia, F. N.; Mueller, T.; Lin, Y. M.; Valdes-Garcia, A.; Avouris, P., Ultrafast graphene photodetector. *Nature Nanotechnology* **2009,** 4, (12), 839-843.

114. Nan, H. Y.; Ni, Z. H.; Wang, J.; Zafar, Z.; Shi, Z. X.; Wang, Y. Y., The thermal stability of graphene in air investigated by Raman spectroscopy. *Journal of Raman Spectroscopy* **2013,** 44, (7), 1018-1021.

115. Ishigami, M.; Chen, J. H.; Cullen, W. G.; Fuhrer, M. S.; Williams, E. D., Atomic structure of graphene on SiO2. *Nano Letters* **2007,** 7, (6), 1643-1648.

116. Sharma, R.; Baik, J. H.; Perera, C. J.; Strano, M. S., Anomalously Large Reactivity of Single Graphene Layers and Edges toward Electron Transfer Chemistries. *Nano Letters* **2010,** 10, (2), 398-405.

117. Yamamoto, M.; Einstein, T. L.; Fuhrer, M. S.; Cullen, W. G., Charge Inhomogeneity Determines Oxidative Reactivity of Graphene on Substrates. *Acs Nano* **2012,** 6, (9), 8335-8341.

118. Solis-Fernandez, P.; Paredes, J. I.; Villar-Rodil, S.; Guardia, L.; Fernandez-Merino, M. J.; Dobrik, G.; Biro, L. P.; Martinez-Alonso, A.; Tascon, J. M. D., Global and Local Oxidation Behavior of Reduced Graphene Oxide. *Journal of Physical Chemistry C* **2011,** 115, (16), 7956-7966.

119. Hahn, J. R.; Kang, H.; Lee, S. M.; Lee, Y. H., Mechanistic study of defect-induced oxidation of graphite. *Journal of Physical Chemistry B* **1999,** 103, (45), 9944-9951.

120. Zhang, J.; Zou, H. L.; Qing, Q.; Yang, Y. L.; Li, Q. W.; Liu, Z. F.; Guo, X. Y.; Du, Z. L., Effect of chemical oxidation on the structure of single-walled carbon nanotubes. *Journal of Physical Chemistry B* **2003,** 107, (16), 3712-3718.

121. Sendt, K.; Haynes, B. S., Density functional study of the chemisorption Of O-2 on the armchair surface of graphite. *Proceedings of the Combustion Institute* **2005,** 30, 2141-2149.

122. Sendt, K.; Haynes, B. S., Density functional study of the chemisorption Of O-2 on the zig-zag surface of graphite. *Combustion and Flame* **2005,** 143, (4), 629-643.

123. Sendt, K.; Haynes, B. S., Density functional study of the chemisorption of O-2 across two rings of the armchair surface of graphite. *Journal of Physical Chemistry C* **2007,** 111, (14), 5465-5473.

124. Lee, M. J.; Choi, J. S.; Kim, J.-S.; Byun, I.-S.; Lee, D. H.; Ryu, S.; Lee, C.; Park, B. H., Characteristics and effects of diffused water between graphene and a SiO2 substrate. *Nano Research* **2012,** 5, (10), 710-717.

125. Patra, N.; Wang, B.; Kral, P., Nanodroplet Activated and Guided Folding of Graphene Nanostructures. *Nano Letters* **2009,** 9, (11), 3766-3771.

126. Lee, D.; Ahn, G.; Ryu, S., Two-Dimensional Water Diffusion at a Graphene–Silica Interface. In American Chemical Society: Journal of American Chemical Society, 2014; Vol. online.

127. Jorio, A.; Martins Ferreira, E. H.; Moutinho, M. V. O.; Stavale, F.; Achete, C. A.; Capaz, R. B., Measuring disorder in graphene with the G and D bands. *Physica Status Solidi B-Basic Solid State Physics* **2010,** 247, (11-12), 2980-2982.

128. Decker, R.; Wang, Y.; Brar, V. W.; Regan, W.; Tsai, H.-Z.; Wu, Q.; Gannett, W.; Zettl, A.; Crommie, M. F., Local Electronic Properties of Graphene on a BN Substrate via Scanning Tunneling Microscopy. *Nano Letters* **2011,** 11, (6), 2291-2295.

129. Chen, J.-H.; Cullen, W. G.; Jang, C.; Fuhrer, M. S.; Williams, E. D., Defect Scattering in Graphene. *Physical Review Letters* **2009,** 102, (23).

130. Bolotin, K. I.; Sikes, K. J.; Jiang, Z.; Klima, M.; Fudenberg, G.; Hone, J.; Kim, P.; Stormer, H. L., Ultrahigh electron mobility in suspended graphene. *Solid State Communications* **2008,** 146, (9-10), 351-355.

131. Venugopal, A.; Chan, J.; Li, X.; Magnuson, C. W.; Kirk, W. P.; Colombo, L.; Ruoff, R. S.; Vogel, E. M., Effective mobility of single-layer graphene transistors as a function of channel dimensions. *Journal of Applied Physics* **2011,** 109, (10).

132. Niyogi, S.; Hamon, M. A.; Hu, H.; Zhao, B.; Bhowmik, P.; Sen, R.; Itkis, M. E.; Haddon, R. C., Chemistry of single-walled carbon nanotubes. *Accounts of Chemical Research* **2002,** 35, (12), 1105-1113.

133. Chu, X.; Schmidt, L. D., REACTIONS OF NO, O2, H2O, AND CO2 WITH THE BASAL-PLANE OF GRAPHITE. *Surface Science* **1992,** 268, (1-3), 325-332.

134. Blackberg, L.; Ringbom, A.; Sjostrand, H.; Klintenberg, M., Assisted self-healing in ripped graphene. *Physical Review B* **2010,** 82, (19), 4.

135. Chen, J.; Shi, T.; Cai, T.; Xu, T.; Sun, L.; Wu, X.; Yu, D., Self healing of defected graphene. *Applied Physics Letters* **2013,** 102, (10).

136. Lin, Y.; Watson, K. A.; Kim, J.-W.; Baggett, D. W.; Working, D. C.; Connell, J. W., Bulk preparation of holey graphene via controlled catalytic oxidation. *Nanoscale* **2013,** 5, (17), 7814-7824.

137. Radich, J. G.; Kamat, P. V., Making Graphene Holey. Gold-Nanoparticle-Mediated Hydroxyl Radical Attack on Reduced Graphene Oxide. *Acs Nano* **2013,** 7, (6), 5546-5557.

138. Wang, B.; Puzyrev, Y. S.; Pantelides, S. T., Enhanced chemical reactions of oxygen at grain boundaries in polycrystalline graphene. *Polyhedron* **2013,** 64, 158-162.

139. Zhu, W. J.; Low, T.; Perebeinos, V.; Bol, A. A.; Zhu, Y.; Yan, H. G.; Tersoff, J.; Avouris, P., Structure and Electronic Transport in Graphene Wrinkles. *Nano Letters* **2012,** 12, (7), 3431-3436.

140. Loren Fuller, E.; Okoh, J. M., Kinetics and mechanisms of the reaction of air with nuclear grade graphites: IG-110. *Journal of Nuclear Materials* **1997,** 240, (3), 241-50.

141. .

142. Hahn, J. R., Kinetic study of graphite oxidation along two lattice directions. *Carbon* **2005,** 43, (7), 1506-1511.

143. Yafei, D.; Shuang, N.; Zhenyu, L.; Jinlong, Y., Diffusion and desorption of oxygen atoms on graphene. *Journal of Physics: Condensed Matter* **2013,** 25, (40), 405301 (6 pp.)-405301 (6 pp.).

144. Radovic, L. R.; Silva-Tapia, A. B.; Vallejos-Burgos, F., Oxygen migration on the graphene surface. 1. Origin of epoxide groups. *Carbon* **2011,** 49, (13), 4218-4225.

145. Radovic, L. R.; Suarez, A.; Vallejos-Burgos, F.; Sofo, J. O., Oxygen migration on the graphene surface. 2. Thermochemistry of basal-plane diffusion (hopping). *Carbon* **2011,** 49, (13), 4226-4238.

146. Qi, X.; Guo, X.; Zheng, C., Density functional study the interaction of oxygen molecule with defect sites of graphene. *Applied Surface Science* **2012,** 259, 195-200.

147. Heo, J.; Chung, H. J.; Lee, S.-H.; Yang, H.; Seo, D. H.; Shin, J. K.; Chung, U. I.; Seo, S.; Hwang, E. H.; Das Sarma, S., Nonmonotonic temperature dependent transport in graphene grown by chemical vapor deposition. *Physical Review B* **2011,** 84, (3).

148. Ciric, L.; Sienkiewicz, A.; Nafradi, B.; Mionic, M.; Magrez, A.; Forro, L., Towards electron spin resonance of mechanically exfoliated graphene. *Physica Status Solidi B-Basic Solid State Physics* **2009,** 246, (11-12), 2558-2561.

149. Bunch, J. S.; van der Zande, A. M.; Verbridge, S. S.; Frank, I. W.; Tanenbaum, D. M.; Parpia, J. M.; Craighead, H. G.; McEuen, P. L., Electromechanical resonators from graphene sheets. *Science* **2007,** 315, (5811), 490-493.

150. Gautam, M.; Jayatissa, A. H., Gas sensing properties of graphene synthesized by chemical vapor deposition. *Materials Science & Engineering C-Materials for Biological Applications* **2011,** 31, (7), 1405-1411.

151. Huang, P. Y.; Ruiz-Vargas, C. S.; van der Zande, A. M.; Whitney, W. S.; Levendorf, M. P.; Kevek, J. W.; Garg, S.; Alden, J. S.; Hustedt, C. J.; Zhu, Y.; Park, J.; McEuen, P. L.; Muller, D. A.,

Grains and grain boundaries in single-layer graphene atomic patchwork quilts. *Nature* **2011,** 469, (7330), 389-+.

152. Jacobberger, R. M.; Arnold, M. S., Graphene Growth Dynamics on Epitaxial Copper Thin Films. *Chemistry of Materials* **2013,** 25, (6), 871-877.

153. Ebisuzaki, Y.; Sanborn, W. B., OXIDATION-KINETICS OF COPPER - AN EXPERIMENT IN SOLID-STATE CHEMISTRY. *Journal of Chemical Education* **1985,** 62, (4), 341-343.

154. Pombo Rodriguez, R. M. H.; Paredes, R. S. C.; Wido, S. H.; Calixto, A., Comparison of aluminum coatings deposited by flame spray and by electric arc spray. *Surface & Coatings Technology* **2007,** 202, (1), 172-9.

155. Fryauf, D. M.; Phillips, A. C.; Kobayashi, N. P. In *Moisture barrier and chemical corrosion protection of silver-based telescope mirrors using aluminum oxide films by plasma-enhanced atomic layer deposition*, Conference on Nanoepitaxy - Materials and Devices V, San Diego, CA, 2013

Aug 25-27, 2013; San Diego, CA, 2013.

156. Karpushenkov, S. A.; Shchukin, G. L.; Belanovich, A. L.; Savenko, V. P.; Kulak, A. I., Plasma electrolytic ceramic-like aluminum oxide coatings on iron. *Journal of Applied Electrochemistry* **2010,** 40, (2), 365-374.

157. Clasen, R.; Deller, K.; Deng, Y.; Fehringer, G.; Oswald, M. Plasma-injected coatings of aluminum oxide on substrate used for corrosion protection of ship or aircraft components. EP1700927-A1; JP2006249581-A; US2006216430-A1; CN101033534-A; JP4518410-B2; US7887923-B2; EP1700927-B1; DE502005011328-G.

158. Rand, B. P.; Genoe, J.; Heremans, P.; Poortmans, J., Solar cells utilizing small molecular weight organic semiconductors. *Progress in Photovoltaics* **2007,** 15, (8), 659-676.

159. Athanasopoulos, S.; Emelianova, E. V.; Walker, A. B.; Beljonne, D., Exciton diffusion in energetically disordered organic materials. *Physical Review B* **2009,** 80, (19).

160. Lunt, R. R.; Benziger, J. B.; Forrest, S. R., Relationship between Crystalline Order and Exciton Diffusion Length in Molecular Organic Semiconductors. *Advanced Materials* **2010,** 22, (11), 1233-+.

161. Karl, N., Charge carrier transport in organic semiconductors. *Synthetic Metals* **2003,** 133, 649-657.

162. Ludwig, C.; Strohmaier, R.; Petersen, J.; Gompf, B.; Eisenmenger, W., EPITAXY AND SCANNING-TUNNELING-MICROSCOPY IMAGE-CONTRAST OF COPPER PHTHALOCYANINE ON GRAPHITE AND MOS2. *Journal of Vacuum Science & Technology B* **1994,** 12, (3), 1963-1966.

163. Dou, W.; Huang, S.; Zhang, R. Q.; Lee, C. S., Molecule-substrate interaction channels of metal-phthalocyanines on graphene on Ni(111) surface. *Journal of Chemical Physics* **2011,** 134, (9).

164. Ren, J.; Meng, S.; Wang, Y.-L.; Ma, X.-C.; Xue, Q.-K.; Kaxiras, E., Properties of copper (fluoro-)phthalocyanine layers deposited on epitaxial graphene. *Journal of Chemical Physics* **2011,** 134, (19).

165. Shi, C.; Wei, C.; Han, H.; Gao, X.; Qi, D.; Wang, Y.; Wee, A. T. S., Template-Directed Molecular Assembly on Silicon Carbide Nanomesh: Comparison Between CuPc and Pentacene. *Acs Nano* **2010,** 4, (2), 849-854.

166. Lei, S. B.; Yin, S. X.; Wang, C.; Wan, L. J.; Bai, C. L., Selective adsorption of copper phthalocyanine atop functionalized organic monolayers. *Journal of Physical Chemistry B* **2004,** 108, (1), 224-227.

167. Lu, J.; Lei, S. B.; Zeng, Q. D.; Kang, S. Z.; Wang, C.; Wan, L. J.; Bai, C. L., Template-induced inclusion structures with copper(II) phthalocyanine and coronene as guests in two-dimensional hydrogen-bonded host networks. *Journal of Physical Chemistry B* **2004,** 108, (17), 5161-5165.

168. Wang, Q. H.; Hersam, M. C., Room-temperature molecular-resolution characterization of self-assembled organic monolayers on epitaxial graphene. *Nature Chemistry* **2009,** 1, (3), 206-211.

169. Forrest, S. R., Ultrathin organic films grown by organic molecular beam deposition and related techniques. *Chemical Reviews* **1997,** 97, (6), 1793-1896.

170. Hooks, D. E.; Fritz, T.; Ward, M. D., Epitaxy and molecular organization on solid substrates. *Advanced Materials* **2001,** 13, (4), 227-+.

171. Witte, G.; Woll, C., Growth of aromatic molecules on solid substrates for applications in organic electronics. *Journal of Materials Research* **2004,** 19, (7), 1889-1916.

172. Hoshi, H.; Dann, A. J.; Maruyama, Y., THE STRUCTURE AND PROPERTIES OF PHTHALOCYANINE FILMS GROWN BY THE MOLECULAR-BEAM EPITAXY TECHNIQUE .3. PREPARATION AND CHARACTERIZATION OF LUTETIUM DIPHTHALOCYANINE FILMS. *Journal of Applied Physics* **1990,** 67, (11), 6871-6875.

173. Wang, S. D.; Dong, X.; Lee, C. S.; Lee, S. T., Orderly growth of copper phthalocyanine on highly oriented pyrolytic graphite (HOPG) at high substrate temperatures. *Journal of Physical Chemistry B* **2004,** 108, (5), 1529-1532.

174. Cheng, C. H.; Wang, J.; Du, G. T.; Shi, S. H.; Du, Z. J.; Fan, Z. Q.; Bian, J. M.; Wang, M. S., Organic solar cells with remarkable enhanced efficiency by using a CuI buffer to control the molecular orientation and modify the anode. *Applied Physics Letters* **2010,** 97, (8).

175. Lunt, R. R.; Benziger, J. B.; Forrest, S. R., Growth of an ordered crystalline organic heterojunction. *Advanced Materials* **2007,** 19, (23), 4229-+.

176. Hong, D.; Do, Y. R.; Kwak, H. T.; Yim, S., Structural templating and growth behavior of copper phthalocyanine thin films deposited on a polycrystalline perylenetetracarboxylic dianhydride layer. *Journal of Applied Physics* **2011,** 109, (6).

177. Lassiter, B. E.; Lunt, R. R.; Renshaw, C. K.; Forrest, S. R., Structural templating of multiple polycrystalline layers in organic photovoltaic cells. *Optics Express* **2010,** 18, (19), A444-A450.

178. Sullivan, P.; Jones, T. S.; Ferguson, A. J.; Heutz, S., Structural templating as a route to improved photovoltaic performance in copper phthalocyanine/fullerene (C(60)) heterojunctions. *Applied Physics Letters* **2007,** 91, (23).

179. Naito, R.; Toyoshinia, S.; Ohashi, T.; Sakurai, T.; Akimoto, K., Molecular orientation control of phthalocyanine thin film by inserting pentacene buffer layer. *Japanese Journal of Applied Physics* **2008,** 47, (2), 1416-1418.

180. Wang, Y.; Tong, S. W.; Xu, X. F.; Ozyilmaz, B.; Loh, K. P., Interface Engineering of Layer-by-Layer Stacked Graphene Anodes for High-Performance Organic Solar Cells. *Advanced Materials* **2011,** 23, (13), 1514-1518.

181. Ling, X.; Xie, L.; Fang, Y.; Xu, H.; Zhang, H.; Kong, J.; Dresselhaus, M. S.; Zhang, J.; Liu, Z., Can Graphene be used as a Substrate for Raman Enhancement? *Nano Letters* **2010,** 10, (2), 553-561.

182. Peumans, P.; Forrest, S. R., Very-high-efficiency double-heterostructure copper phthalocyanine/C-60 photovoltaic cells. *Applied Physics Letters* **2001,** 79, (1), 126-128.

183. Xue, J. G.; Uchida, S.; Rand, B. P.; Forrest, S. R., 4.2% efficient organic photovoltaic cells with low series resistances. *Applied Physics Letters* **2004,** 84, (16), 3013-3015.

184. Forsythe, E. W.; Abkowitz, M. A.; Gao, Y., Tuning the Carrier Injection Efficiency for Organic Light-Emitting Diodesâ€. *The Journal of Physical Chemistry B* **2000,** 104, (16), 3948-3952.

185. Masenelli, B.; Berner, D.; Bussac, M. N.; Nuesch, F.; Zuppiroli, L., Simulation of charge injection enhancements in organic light-emitting diodes. *Applied Physics Letters* **2001,** 79, (26), 4438-4440.

186. Hoshino, A.; Takenaka, Y.; Miyaji, H., Redetermination of the crystal structure of alpha-copper phthalocyanine grown on KCl. *Acta Crystallographica Section B-Structural Science* **2003,** 59, 393-403.

187. Yin, S. X.; Wang, C.; Xu, B.; Bai, C. L., Studies of CuPc adsorption on graphite surface and alkane adlayer. *Journal of Physical Chemistry B* **2002,** 106, (35), 9044-9047.

188. Gouterman, M., Study of the Effects of Substitution on the Absorption Spectra of Porphin. *The Journal of Chemical Physics* **1959,** 30, (5), 1139-+.

189. Foweraker, A. R.; Jennings, B. R., Orientation of the electronic transitions in crystalline copper phthalocyanine by means of electric dichroism. *Spectrochimica Acta Part A: Molecular Spectroscopy* **1975,** 31, (8), 1075-1083.

190. Powell, R. C.; Soos, Z. G., SINGLET EXCITON ENERGY-TRANSFER IN ORGANIC SOLIDS. *Journal of Luminescence* **1975,** 11, (1-2), 1-45.

191. Poulston, S.; Parlett, P. M.; Stone, P.; Bowker, M., Surface oxidation and reduction of CuO and Cu2O studied using XPS and XAES. *Surface and Interface Analysis* **1996,** 24, (12).

192. Tobin, J. P.; Hirschwald, W.; Cunningham, J., XPS AND XAES STUDIES OF TRANSIENT ENHANCEMENT OF CU-1 AT CUO SURFACES DURING VACUUM OUTGASSING. *Applied Surface Science* **1983,** 16, (3-4).

193. Yu, Q.; Jauregui, L. A.; Wu, W.; Colby, R.; Tian, J.; Su, Z.; Cao, H.; Liu, Z.; Pandey, D.; Wei, D.; Chung, T. F.; Peng, P.; Guisinger, N. P.; Stach, E. A.; Bao, J.; Pei, S.-S.; Chen, Y. P., Control and characterization of individual grains and grain boundaries in graphene grown by chemical vapour deposition. *Nature Materials* **2011,** 10, (6).

194. Ogawa, Y.; Hu, B.; Orofeo, C. M.; Tsuji, M.; Ikeda, K.-i.; Mizuno, S.; Hibino, H.; Ago, H., Domain Structure and Boundary in Single-Layer Graphene Grown on Cu(111) and Cu(100) Films. *Journal of Physical Chemistry Letters* **2012,** 3, (2).

195. Ishihara, M.; Koga, Y.; Kim, J.; Tsugawa, K.; Hasegawa, M., Direct evidence of advantage of Cu(111) for graphene synthesis by using Raman mapping and electron backscatter diffraction. *Materials Letters* **2011,** 65, (19-20).

196. Buron, J. D.; Petersen, D. H.; Boggild, P.; Cooke, D. G.; Hilke, M.; Sun, J.; Whiteway, E.; Nielsen, P. F.; Hansen, O.; Yurgens, A.; Jepsen, P. U., Graphene Conductance Uniformity Mapping. *Nano Letters* **2012,** 12, (10).

197. Jin, Z.; McNicholas, T. P.; Shih, C.-J.; Wang, Q. H.; Paulus, G. L. C.; Hilmer, A.; Shimizu, S.; Strano, M. S., Click Chemistry on Solution-Dispersed Graphene and Monolayer CVD Graphene. *Chemistry of Materials* **2011,** 23, (14).

198. Hofrichter, J.; Szafranek, B. N.; Otto, M.; Echtermeyer, T. J.; Baus, M.; Majerus, A.; Geringer, V.; Ramsteiner, M.; Kurz, H., Synthesis of Graphene on Silicon Dioxide by a Solid Carbon Source. *Nano Letters* **2010,** 10, (1).

199. Wu, W.; Liu, Z.; Jauregui, L. A.; Yu, Q.; Pillai, R.; Cao, H.; Bao, J.; Chen, Y. P.; Pei, S.-S., Wafer-scale synthesis of graphene by chemical vapor deposition and its application in hydrogen sensing. *Sensors and Actuators B-Chemical* **2010,** 150, (1).

200. Li, X.; Cai, W.; Colombo, L.; Ruoff, R. S., Evolution of Graphene Growth on Ni and Cu by Carbon Isotope Labeling. *Nano Letters* **2009,** 9, (12).

201. Weatherup, R. S.; Dlubak, B.; Hofmann, S., Kinetic Control of Catalytic CVD for High-Quality Graphene at Low Temperatures. *ACS nano* **2012,** 6, (11).

Appendix A: Supporting information for chapter 2

This appendix was adopted from the supporting information of "Singha Roy, S.; Arnold, M., Improving Graphene Diffusion Barriers via Stacking Multiple Layers and Grain Size Engineering. *Advanced Functional Materials* **2013,** 23, (29), 3638-3644." *SS performed all the experiments and analysis for the study*.

XPS Analysis:

X-ray Photoelectron Spectroscopy (XPS) and X-ray excited Auger Electron Spectroscopy (XAES) were performed on a subset of samples to confirm the trend of increasing diffusion barrier performance with increasing layer number, identified in Figures 2.1 and 2.2. XPS and XAES were specifically used to estimate the relative abundance of unoxidized and oxidized Cu on bare Cu, SLG*x*1_Cu, SLG*x*2_Cu and SLG*x*4_Cu substrates annealed at 200 °C for 240 minutes in air.

The XPS and XAES data were taken with a ~3.5 x 1 mm^2 spot size and, therefore, do not have sufficient resolution to map the Cu oxidation. Unlike Raman mapping, as a result of the large spot size, XPS and XAES quantify oxygen permeation through features both (i) extrinsic (macroscopic defects and tears due to non-optimized processing) and (ii) intrinsic to CVD graphene (grain-boundaries and point-defects). In contrast, using Raman mapping, we can exclusively study the latter. It should be noted that determining the relative abundance of unoxidized and oxidized Cu using XPS and XAES is furthermore complicated by spectral congestion but can be estimated by examining features in both spectra. Furthermore, the sensitivity of the XPS is optimal only to depths of a few nanometers thereby making it harder analyze the copper in the stacked multilayer samples, whereas the Raman laser has a higher penetration depth and can get through the transparent graphene and copper oxide layers.

First, we characterized an unannealed, bare Cu substrate (Fig. A.S1a-c). The native oxide was mostly removed from the sample via *in situ* Ar sputtering in order to obtain a baseline spectrum. In the XPS spectrum, unoxidized Cu is identified by Cu $2p_{3/2}$ and Cu $2p_{1/2}$ peaks at 932.6 eV and 952.6 eV, respectively, (Fig. A.S1a).[191, 192] The O 1s and C 1s peaks are substantially weaker (Figs. A.S1b and A.S1c, respectively). The shape of Auger L3VV spectrum (denoting Auger electron emission from the valence band) can be used to determine the oxidation state of the Cu and indicates (Fig. A.S2a) that the Cu is in the ground state – Cu(0).

Next, we characterized a SLG*x*1_Cu sample, prior to annealing in air. The XPS (Fig. A.S1d-f) and XAES (Fig. A.S2b) spectra are similar to that of the unannealed, bare Cu substrate, indicating that the underlying Cu in the SLG*x*1_Cu sample prior to annealing is unoxidized, as expected. Similar measurements for unannealed SLG*x*2_Cu and SLG*x*4_Cu were not performed as we would expect to get similar results without annealing.

The Cu, SLG*x*1_Cu, SLG*x*2_Cu, and SLG*x*4_Cu samples were then annealed at 200 °C for 240 min. in air and their spectra were (re-)measured. The XPS and XAES spectra of the oxidized bare Cu sample (Figs. A.S1g-i and Fig. 2.2c) are different following oxidation. In the Cu 2p spectrum, (a) the Cu $2p_{3/2}$ and Cu $2p_{1/2}$ shift to 933.6 eV and 952.8 eV, respectively, and two new satellite peaks at 942.6 eV and 962.3 eV arise, (b) a highly intense O 1s twin-peak at 529.3 eV (CuO) and 530.3 eV (Cu_2O) evolve, (c) there is a drastic increase in the oxygen atomic concentration (as quantified in Table A.1), (d) there a significant change in the Auger L3VV spectra (Fig. A.S2c). All of these features are consistent with that expected for oxidized Cu[191, 192], confirming that, as expected, after 240 min. of annealing at 200 °C, the surface of the bare Cu substrate is nearly fully oxidized.

These spectroscopic signatures of oxidation diminish, even after annealing at 200 °C for 240 min. in air, as the Cu surface is passivated with increasing layers of graphene. The XPS and XAES data for the annealed SLG*x*1_Cu sample are shown in Fig. A.S1j-l and Fig. A.S2d, respectively. The XPS and XAES data for the annealed SLG*x*2_Cu sample are shown in Fig. A.S1m-o and Fig. A.S2e, respectively. The XPS and XAES data for the annealed SLG*x*4_Cu sample are shown in Fig. A.S1p-r and Fig. A.S2f, respectively.

The Cu signatures in the spectra of the annealed SLG*x*4_Cu sample are nearly identical to that of the unoxidized, bare Cu sample, indicating that the 4 layers of graphene nearly perfectly passivates the underlying Cu from oxidation within the 240 minutes, consistent with the findings from SEM in Figure 2.1 and via Raman spectroscopy in Figure 2.2. It should be noted that there is an O 1s signature in the annealed SLG*x*4_Cu sample (Fig. A.S1q), however, the peak shifts to 532.2 eV and is attributable to an oxidized form of C (rather than Cu oxide). The oxidized C may arise from the residual PMMA (used during layer transfer) or possibly from the oxidation of the graphene, itself.

In order to quantify the degree of Cu and C oxidation, we fit the O 1s spectra at 529.3 eV (CuO), 530.3 (Cu_2O) and 532.2 (oxygen bonded with carbon) as shown in Figure A.S3. The atomic concentrations (%) were calculated by comparing the areas under the peaks and using appropriate relative scaling factors. The fraction of oxidized copper decreases from 0.74 to 0.29

to 0.053 to < 0.045 for the bare Cu, SLG*x*1_Cu, SLG*x*2_Cu, and SLG*x*4_Cu samples, respectively. Quantification of the ratio for the SLG*x*4_Cu sample is limited by noise.

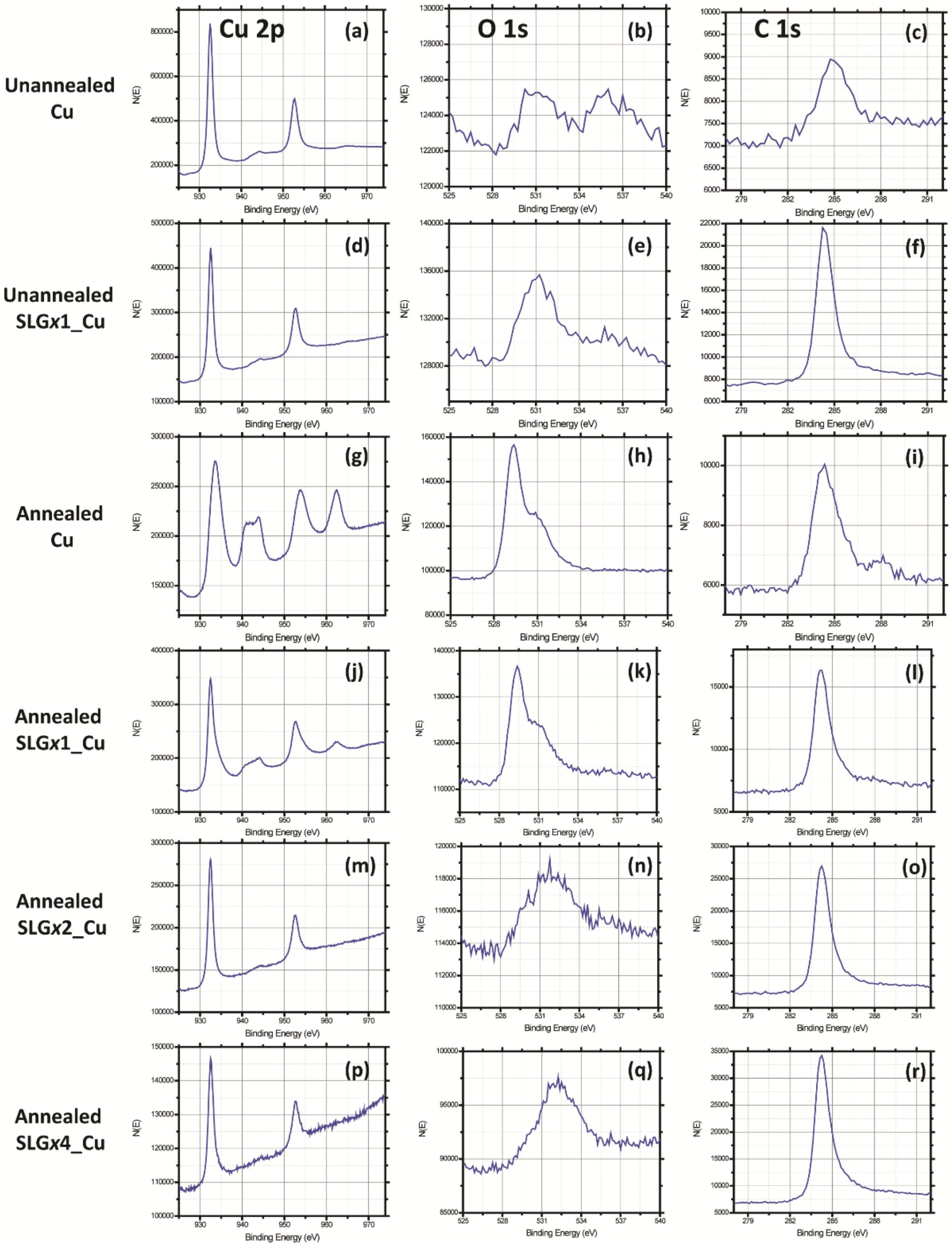

Figure A.S1: XPS spectra of Cu 2p, O 1s and C 1s.

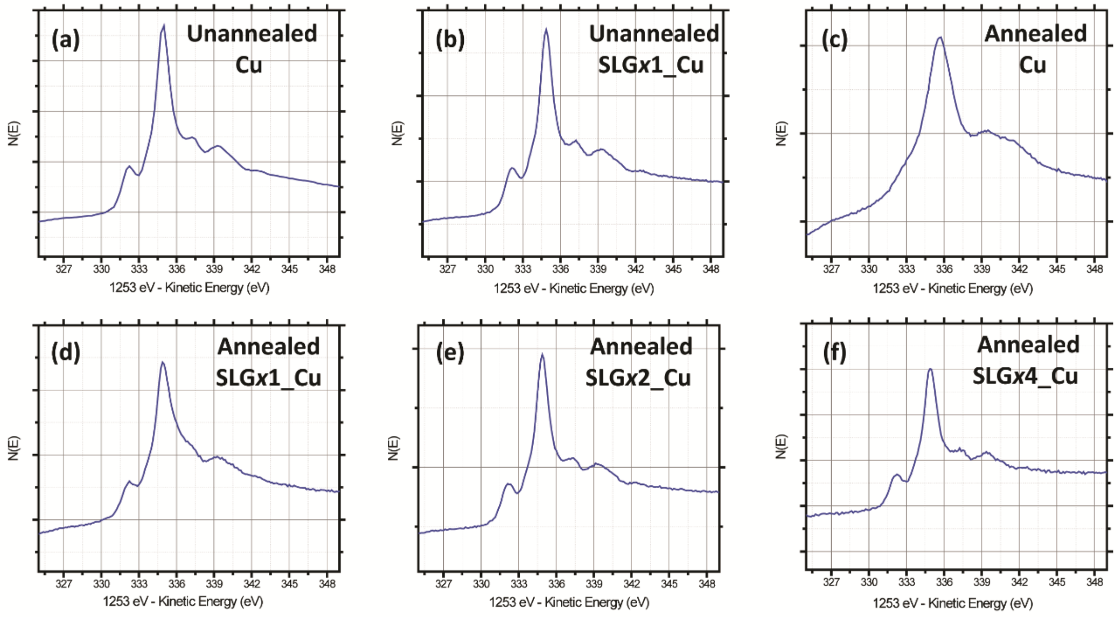

Figure A.S2: XAES spectra of Cu Auger L3VV: (a) Unannealed Cu, (b) Unannealed SLG*x*1_Cu, (c) Annealed Cu, (d) Annealed SLG*x*1_Cu, (e) Annealed SLG*x*2_Cu, and (f) Annealed SLG*x*4_Cu.

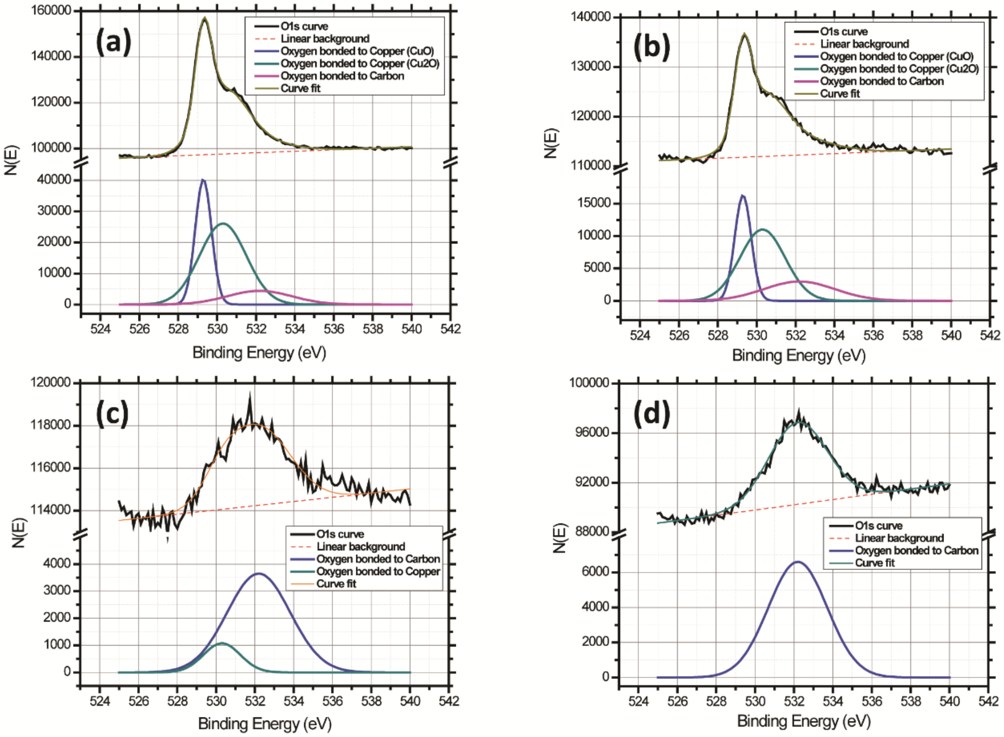

Figure A.S3: O1s XPS spectra with curve fits for samples annealed for 4 hours at 200 °C in air. (a) Annealed bare Cu, (b) Annealed SLG*x*1_Cu, (c) Annealed SLG*x*2_Cu, and (d) Annealed SLG*x*4_Cu.

Table A.1: O1s peak analysis for unannealed and annealed samples quantifying the fraction of Cu oxidized.

Sample Identity /XPS	Atomic concentration of Copper (%)	Oxygen bonded to Copper (%)	Oxygen bonded to Carbon (%)	Atomic concentration of Carbon (%)	Fraction of oxidized Copper
Bare Cu (unannealed)	90.2	3.6	-	6.2	0.04
SLGx1_Cu (unannealed)	57	2.4	2.9	37.7	0.042
Bare Cu (annealed)	48.5	35.8	5.4	10.3	0.74
SLGx1_Cu (annealed)	53.4	15.5	4.3	26.8	0.29
SLGx2_Cu (annealed)	22.7	1.2	6.2	69.9	0.053
SLGx4_Cu (annealed)	6.7	< 0.3	7	86.3	< 0.045

Pre-anneal Raman analysis:

In an attempt to map grain boundaries in graphene on Cu, prior to oxidation, we performed Imaging Raman Spectroscopy on ~ 20 μm x 20 μm area of a SLG*x*1_Cu sample with 14 μm graphene grain size. The results are shown in Figure A.S4. We were not able to image the grain boundaries by analyzing the D/G ratio due to insufficient signal to noise, even after imaging after 24 hours, due to degradation of the signal to noise on the Cu substrates. The spatial variation of the D-band and G-band are depicted in the parts (c) and (d), respectively, and it can be noted that there is not much change in the intensities of both the bands except in a few spots (encircled in red). The averaged spectrum of the whole scanned area is shown at the bottom (in blue in Figure A.S4d) along with a normal spot (top and black) and a defective spot (middle and red). The respective locations of the spots on the map have been highlighted with hollow circles in Figure A.S4b.

It should be pointed out that there have been several studies that have included Raman maps of as-manufactured CVD-graphene,[45, 46, 52, 75, 80, 193-201] however only a very few of them have been able to successfully image grain boundaries without external treatment. These successful studies have been done using a partially or fully grown graphene layer transferred onto a SiO_2/Si substrate, which drastically improves the signal to noise ratio of the Raman spectra (enabling resolution of D/G ratios down to 0.01 or even less).[46, 80, 193, 200] Typical the D/G ratios are ~ 0.04 in the grain interiors, ~ 0.08 – 0.14 at the grain boundaries, and ~ 0.25 at point defects and/or nucleation sites. However, in case of as-manufactured CVD-graphene on a Cu substrate we are severely limited by the signal to noise of the Raman spectra (even after 24-hour long scans) thereby restricting our ability to measure the weakest peak (D-band) to a great extent. Hence, in our spatial maps of D and G band intensities, we are unable to see the grain boundary patterns prior to annealing as our noise level even after a 24 hour scan is still about ± 3 a.u. With this error, the minimum D/G ratio that can be measured is ~ 0.16 (where I_G ~ 37 a.u.) thereby limiting the sensitivity of the scan to detection of point defects and/or nucleation sites. One such feature has been encircled in red in Figure A.S4b and the corresponding Raman spectra has been shown in Figure A.S4d (middle-red)

However, the fact that the oxidation of Cu takes place at the grain boundaries of graphene can be further verified with the help of the inter-nucleation distance observed during the partial growth of SLG*x*1_Cu. The inter-nucleation distance is the parameter that determines the average grain size, hence if the growth from the nucleation sites (as shown in Figure A.S5a) are extrapolated, one can predict the average grain-size of the graphene. When this extrapolation is compared with the oxidized SLG*x*1_Cu (in this case a fully grown monolayer) in Figure A.S5b it can be seen that the web-like pattern of oxidation of the Cu matches the grain boundary network of the graphene, additionally confirming that transport through SLG*x*1_Cu occurs through the grain boundaries.

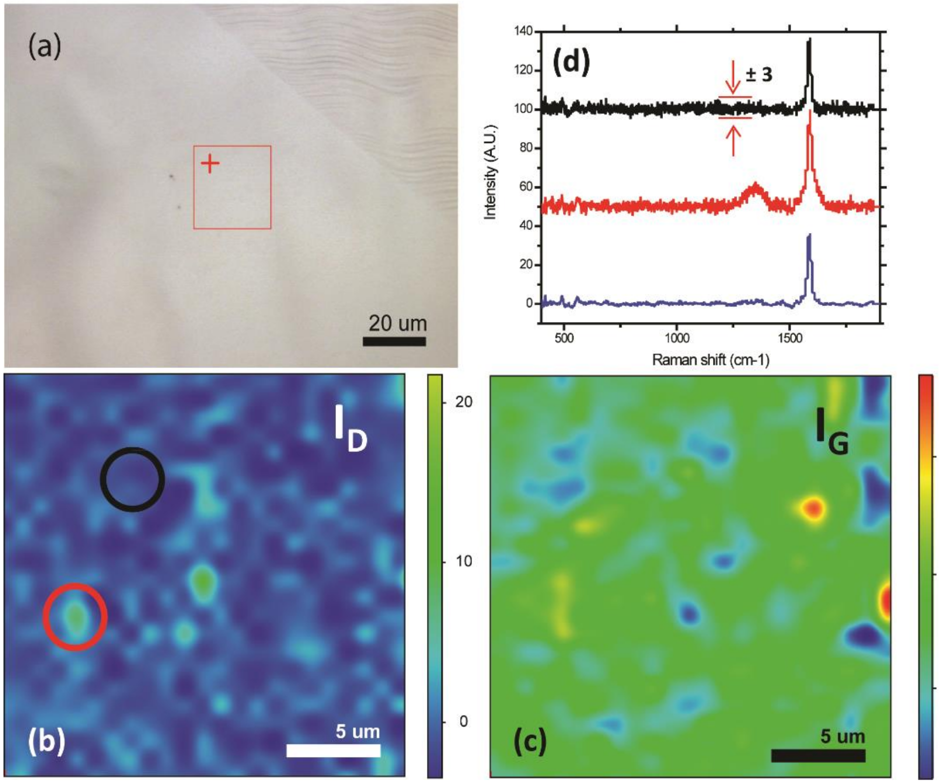

Figure A.S4: Pre-anneal Imaging Raman Spectra of as-manufactured CVD-graphene on Cu with 14 µm graphene grain size: (a) Optical image of the scanned area highlighted with a red square outline, (b) Spatial variation of the intensity of the D-band at 1345 cm^{-1}, (c) Spatial variation of the intensity of the G-band at 1585 cm^{-1}, and (d) Bottom (blue): Spatially averaged spectrum of the scanned area, Top (black): spectrum of the black encircled spot from (b) – depicting a normal spot, Middle (red): spectrum of the red encircled spot from (b) – depicting defective spot.

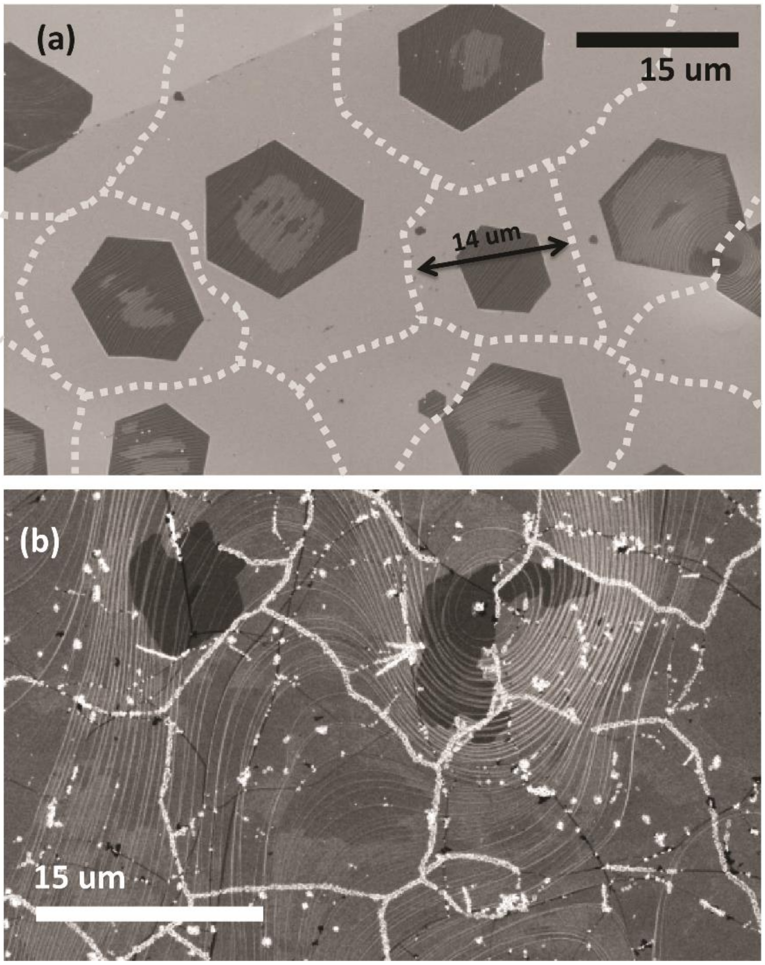

Figure A.S5: Schematic predicting the oxidation of Cu at the grain boundaries of graphene: (a) Partially grown SLGx1_Cu with average inter-nucleation distance equaling 14 μm, extrapolation and merging of growth-fronts from the nucleation site are depicted by dotted white lines. (b) An oxidized fully grown SLGx1_Cu with 14 μm grain-size.

Appendix B: Supporting information for chapter 4

This appendix is adapted from “Singha Roy. S.; Bindl, D. J.; Arnold, M. S., Templating Highly Crystalline Organic Semiconductors Using Atomic Membranes of Graphene at the Anode/Organic Interface. *Journal of Physical Chemistry Letters* **2012,** 3, (7).” SS synthesized and transferred graphene, deposited organic film, performed X-ray diffraction analysis, Raman spectroscopy scanning electron microscopy and analyzed data. DJB performed the optical characterization.

The peaks positions and widths of the XRD spectra were independent of film thickness over the explored range of 20 nm to 320 nm (as shown in Figure S1), indicating that the orientation of the CuPc was invariant over this range.

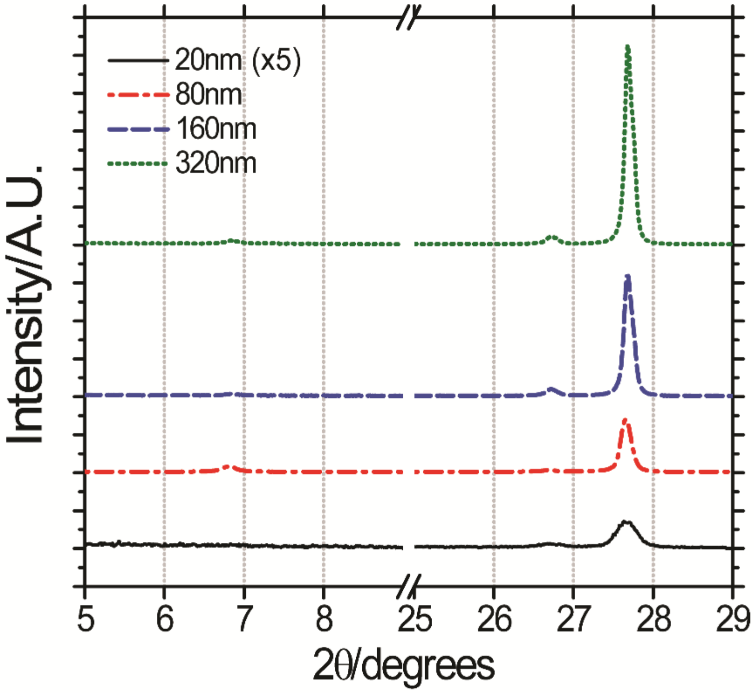

Figure B.S1. X-ray diffraction of CuPc on GMG for CuPc film thicknesses of 20 nm (solid/black) 5x magnification, 80 nm (dot-dashed/red), 160 nm (dashed/blue) and 320 nm (dotted/green)

Appendix C: Supporting information for chapter 6

Graphene synthesis via atmospheric pressure CVD

The copper foils and the epitaxial copper thin-films are introduced into the furnace in a 95% Argon + 5% Hydrogen environment at the annealing temperature T_A (Fig. C.S1). The furnace is maintained at this state for a period of t_A, defined as the pre-growth annealing period. This period plays a crucial part in determining the surface morphology of the growth substrate when copper foil is used as the substrate for growth. After the annealing period, if necessary, the temperature is quickly modified to the growth temperature T_G. However, in all the growths performed during this study $T_A = T_G$, unless specified in the text. Once the furnace attains the temperature T_G, 95% Argon + 5% Methane is introduced at 0.500 sccm to initiate the growth process. The furnace is then maintained at this state for a time period of T_G, the growth duration t_G. All the growths performed on the copper foils had a $t_G = 2$ hours, unless specified. Following this the samples are rapidly cooled by introducing them to room temperature in the same environment. The samples are cooled until they attain the room temperature following which they are removed and stored in a N_2 environment in a glovebox.

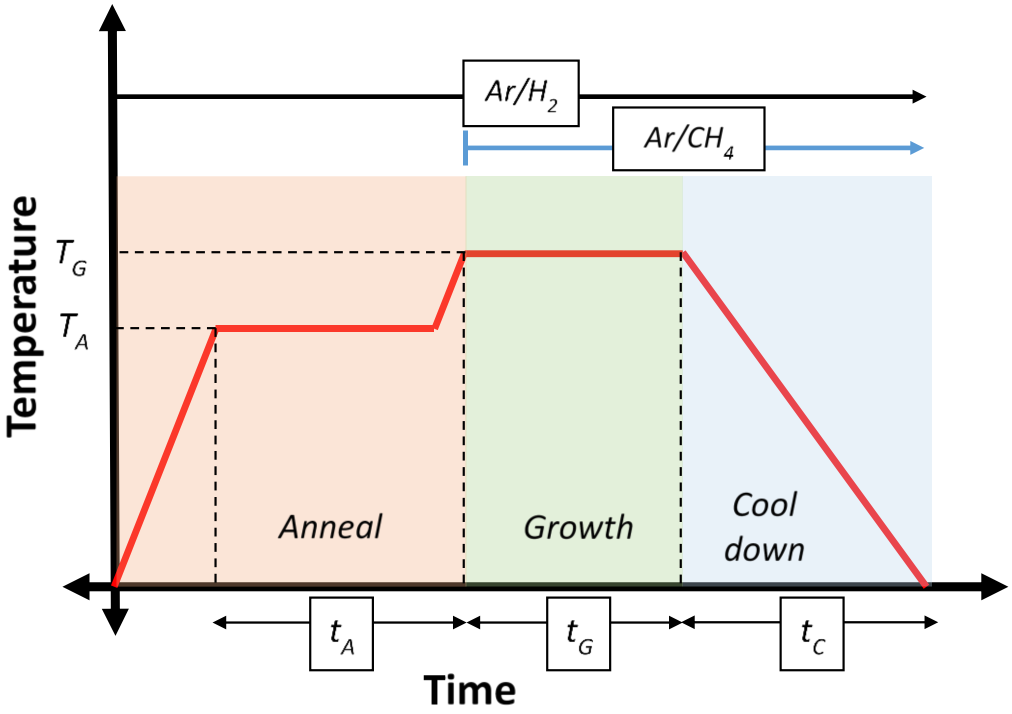

Figure C.S1: Schematic representing a typical process-flow involved in the manufacture of graphene via chemical vapor deposition.

Characterizing surface roughness of copper foils:

Post-synthesis of VCMG, the surface roughness was characterized using a white light interferometry. A typical measurement is shown in figure C.S2. Figure C.S2 shows the surface morphology of the copper foils after graphene synthesis.

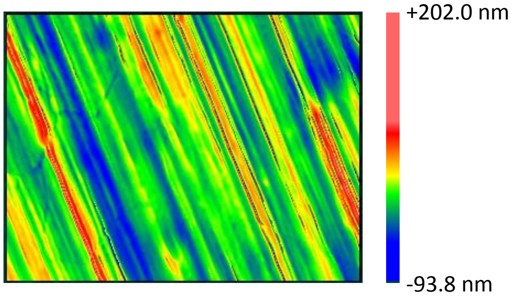

Ra = 200.8 nm	X = 180 µm
rms = 257.9 nm	Y = 130 µm

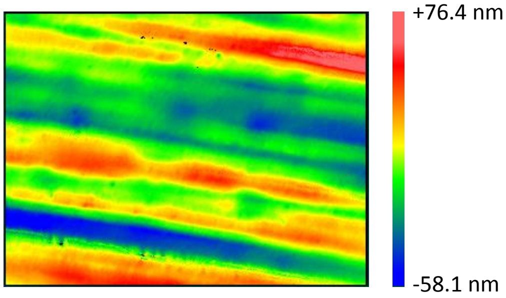

Ra = 187.5 nm	X = 180 µm
rms = 228.3 nm	Y = 130 µm

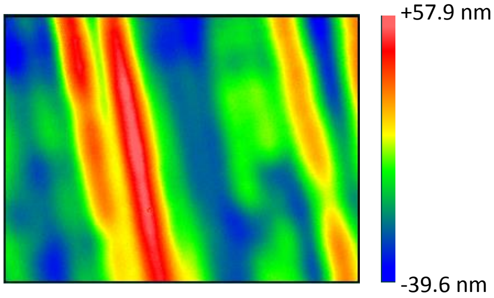

Ra = 168.9 nm	X = 180 µm
rms = 205.0 nm	Y = 130 µm

Figure C.S2: Surface morphology of copper foils after graphene synthesis using white light interferometry. Top to bottom: represent surface morphology at 1223 K, 1273 K and 1323 K, respectively with an pre-growth annealing period of 0.5 hours and growth duration of 2 hours. The tables in the bottom of the figures show the calculated rms roughness and the scan dimensions of the respective figures.